Simultaneous Coding of Microscopic and Macroscopic Features of Touch in Mouse Somatosensory Cortex

By

Brian R Isett

A thesis submitted in partial satisfaction of the

requirements for the degree of

Doctor of Philosophy

in

Neuroscience

in the

Graduate Division

of the

University of California, Berkeley

Committee in charge:

Professor Daniel E. Feldman, Chair
Professor Hillel Adesnik
Professor Yang Dan
Professor Damian Elias

Spring 2017

Abstract

Simultaneous Coding of Microscopic and Macroscopic Features of Touch in Mouse Somatosensory Cortex

by Brian R Isett

Doctor of Philosophy in Neuroscience

University of California, Berkeley

Professor Daniel E. Feldman, Chair

The cerebral cortex is thought to generate sensory experience and facilitate broadly integrative processing used in attention, decision making, and learning. A major goal in neuroscience is to understand how neurons in cortex interact to represent sensory change in the world. Rodents use whiskers to actively palpate their surroundings and gather tactile information. While it is known that rodents can discriminate different textures using whisker input, how the whisker system encodes local spatial features, like shape, is not well understood.

For many perceptual tasks rodents must pay attention to whisker input in order to extract relevant sensory information. Neural oscillations (gamma) may indicate attentive brain states, and Chapter 2 explores how sensory experience may shape the brain's ability to generate these rhythms. Superficial layers of primary somatosensory cortex (S1) showed a profound reduction in recurrent inhibition after sensory deprivation, as well as a sharp reduction in spontaneous and evoked gamma oscillations. These findings suggest cortical rhythms change with sensory experience in a recurrent inhibition-dependent manner.

How the whisker system encodes spatial features, like shape is unknown. In Chapter 3 we describe an experiment designed to study basic elements of shape encoding, using a set of tactile gratings. We trained mice to discriminate smooth surfaces from rough surfaces composed of raised gratings or sandpaper. High-speed whisker imaging revealed that stick-slip micromotions clustered on discrete grating ridges, evoking spatially and temporally precise spikes in S1. At the same time, slip-responsive neurons also responded to whisker contact and texture, forming an overlapping population of tactile feature responses. Mean firing rate was higher on rough surfaces due to stick-slip-evoked spikes, and by weighting individual units we could accurately predict rough vs. smooth trials from neural activity alone. Surprisingly, 20% of neurons showed selectivity among rough textures, including tuning for specific gratings. Thus, S1 neurons simultaneously coded microscopic and macroscopic features of touch during active palpation of tactile gratings.

Table of Contents

Acknowledgements

This thesis would not have been possible without the support of my peers, friends and family. Countless conversations carried me through difficult times, even when the details of the hardships were abstract. Without that support, I would have given up a long time ago.

I would also like to thank my advisor, Dan Feldman, for teaching me how to think like a scientist, ask better questions, and make sense of messy biological data. Dan was an excellent mentor and I will always be thankful for his support and patience. While in his lab I had the pleasure of working with Ray Shao on work appearing in this manuscript, and relied on the assistance of Janice Chua, Karan Patel, Sierra Feasel, and Monet Lane in various behavioral training and analysis procedures. I could not have completed this work without their help. I would like to thank Kelly Clancy for showing me there are no limits to multi-tasking, and for starting a creative writing group that was a great source of inspiration. I would like to thank Amy LeMessurier and Keven Laboy for always taking time to discuss analytic techniques, and to Keven for explaining complex mathematical concepts in ways that made them practical and approachable. I would like to thank Sam Harding-Forrester for moral support and his friendship inside and outside of lab. I would also like to thank Melanie Gainey for her guidance and unceasing friendship. Last but not least, I would like to thank Katie Smith for help in surgical, behavioral, and lab technique training. To everyone in the Feldman lab, thank you for your friendship, helpful suggestions, feedback, and support. I cannot imagine a better group of people for both discussing science and hitting the dance floor.

No acknowledgement would be complete without thanking the Helen Wills Neuroscience community. Kati Markowitz ruled the graduate program with a practical and fun-loving outlook, and she gave me much good advice. I also want to thank the HWNI faculty, including Dan Feldman, who worked to improve the graduate program during my time here. Many of the requirements and courses that were missing when I started are implemented now, to positive effect. Whether at the student organized Neuro Data Mining Group or playing croquet with freshly broken mallets at the departmental beer hour, I have met amazing people who achieve greatness inside and outside of science. To everyone mentioned and countless others, thank you.

Chapter 1

Introduction

One of the most striking features of the human brain is the large cerebral cortex, which has upwards of 20 billion neurons. This outer sheath of the brain generates some our most interesting human qualities, including language, abstract thinking, and conscious sensory experience. How the cortex generates phenomena like sensory experience is still not well understood. Studying the cortex in other mammals has led to many important insights that generalize well across species, with one famous example being the hierarchy of visual feature extraction first studied in cat visual cortex (Hubel and Wiesel, 1959). Here we examine a sensory modality that initially appears quite different from any possessed by humans: the whisker system in rodents. Surprisingly, the whisker system has many direct similarities with the sense of touch in our fingertips, including its use in active tactile exploration and the level of tactile sensitivity that it allows (Diamond, 2010). Unlike primate sensation, the sensory input to a single cortical column in the whisker primary somatosensory cortex (S1) can be studied in exquisite detail during naturalistic active tactile exploration. In particular, we use these benefits to study how the whisker system encodes surface texture and local shapes in cortical neural activity.

The whisker system

Rodents possess 25-30 specialized hairs (called macrovibrissa or “whiskers”) on each side of the snout. These hairs are tapered at the tip which allows them to “slip” past features on textured surfaces (Hires et al., 2013). Many nocturnal rodents actively sweep their whiskers in rostrocaudal space by rhythmically contracting the intrinsic and

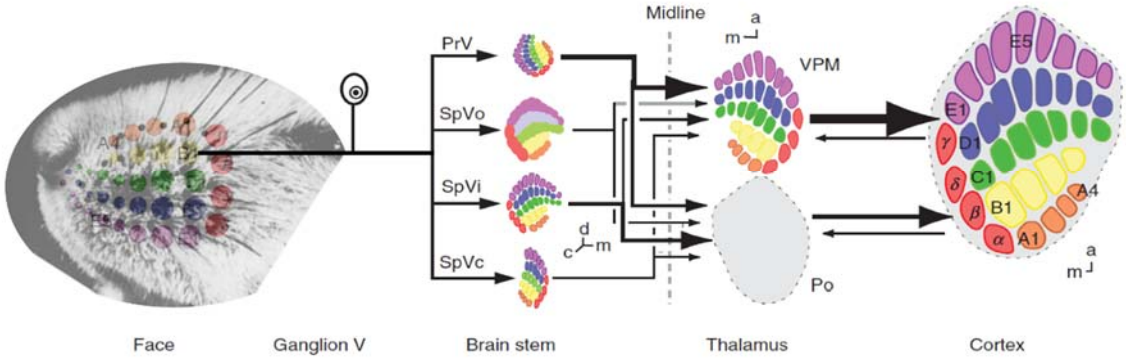

Figure 1.1. Whisker ascending pathway. (Adapted from Woolsey, 2010, 1970). Trigeminal ganglion (V). Brain stem: principal trigeminal nucleus (PrV), Spinal trigeminal nucleus (SpV) with subnucleus interpolaris (SpVi), subnucleus oralis (SpVo), subnucleus caudalis (SpVc). Thalamus: ventroposterior medial nucleus (VPM) and posterior nucleus (Po). Cortex: whisker primary somatosensory cortex with whisker columns corresponding to face. Medial (m), dorsal (d), caudal (c), anterior (a).

extrinsic muscles in the mystacial pad (Haidarliu et al., 2015). Each whisker grows from a follicle highly innervated by lanceolate endings, reticular endings, and Merkel cells (Ebara et al., 2002) which transduce self-movements and external stimuli into action potentials (Leiser and Moxon, 2007). Merkel cells in particular may be vital for transducing the epicritic touch required for texture discrimination (Maricich et al., 2012). These touch signals are sent along afferents of the trigeminal nerve and stay largely segregated by whisker follicle throughout each ascending synapse of the lemniscal pathway (Figure 1.1). This is evidenced by a somatotopic map of the mystacial pad in the principal nucleus of the brainstem (PrV “barrelettes,” Pokay, 1991), and again in the ventroposterior medial (VPM) nucleus of the thalamus (“barreloids,” Van Der Loos, 1976). Thalamocortical projection neurons also maintain follicle organization, segregating the thalamorecipient layer of cortex, layer 4 (“L4”), into a clear somatotopic map of “barrels” (Woolsey, 1970). Thus, each hemisphere of the cerebral cortex contains a primary somatosensory region with a stereotyped somatotopic map of the contralateral whisker pad. It is currently thought that many aspects of the ascending sensory pathway work to filter out self-generated whisker movement signals (Yu et al., 2016) for possible use as reafferent proprioceptive information (Moore et al., 2015), or simply to reduce signal noise in whisker touch towards a theoretical minimum (Hires et al., 2015).

In cortex, each whisker is represented in one cortical column consisting of 6 layers, defined by inputs, cellular architecture, and outputs (Figure 1.2; Lübke and Feldmeyer, 2007). Neurons in L4 receive single-whisker thalamic input and respond with low latency to whisker touch, sending excitatory input to inhibitory and excitatory cells in layer 2/3 (L2/3). Pyramidal cells in L2/3 show salt-and-pepper whisker selectivity, which means they are more scattered than the single-whisker somatotopy of L4 (Clancy et al., 2015). Many studies have shown that L2/3 neurons are remarkable

sites for plasticity (Stern et al., 2001) and may be sharply modulated by attentional circuits (Zhang et al., 2014) in order to make rapid functional changes under volitional control (Clancy et al., 2014). In Chapter 2, we present a study examining the plasticity of recurrent inhibition in L2/3 neurons after experience-dependent plasticity. These changes profoundly reduced spontaneous and evoked gamma rhythms in L2/3, which have been traditionally associated with perceptual binding and attention (Fries, 2009).

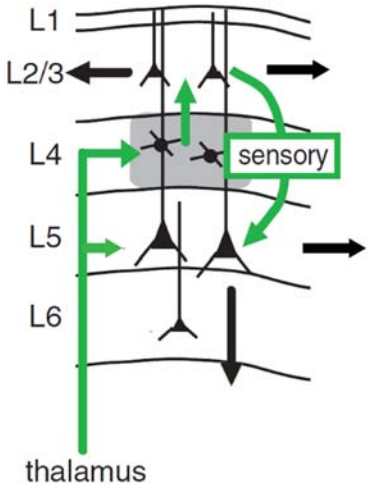

Figure 1.2. S1 column excitatory flow. (Adapted from Constantinople and Bruno, 2013). Layer 1-6 with canonical sensory information flow with green arrows. Horizontal and output projections shown with black arrows. Majority excitatory cell types: spiny stellate cells indicated in L4, and pyramidal cells indicated in L2/3, L5 and L6.

In the canonical cortical circuit, L2/3 neurons synapse with pyramidal cells in L5, and these two layers connect widely with neighboring cortical columns and areas (Aronoff et al., 2010; Feldmeyer et al., 2006; Ghazanfar and Nicolelis, 1999; Hattox and Nelson, 2007; Manns et al., 2004; Oberlaender et al., 2011; Sarid et al., 2015). In addition, L5 neurons receive direct thalamic input (Constantinople and Bruno, 2013) and translaminar inhibition from L4 (Pluta et al., 2015). How cortical layers of S1 columns process diverse, naturalistic input is still not well understood. In Chapter 3, we look at texture and spatial feature coding across cortical layers, finding that spatiotemporally precise response properties were prevalent in L4, but that responses to macroscopic properties like roughness and spatial frequency tuning emerged in extragranular layers (L2/3, L5).

Whisker behavior

In order to best understand how the whisker system functions, it is critical to understand how animals naturally use whisker inputs. As early as 1912 it was understood that trimming the macrovibrissa of a blind rat could drastically interfere with the rat's ability to navigate a maze (Vincent, 1912). Thus, whiskers supply important information during locomotion in the absence of vision or in low light conditions. While navigating in the dark, rodents actively sweep their whiskers in rostro-caudal space at up to 30Hz, using whisker contact events to extract useful information. Mice instinctively use their whiskers to run along object contours, using whisker input to maintain a constant distance via thigmotaxis (Sofroniew et al., 2014). As running speed increases, the

position of the whisker follicle and whisking set point move rostrally (Kleinfeld and Deschênes, 2011; Sofroniew et al., 2014). Thus, the whisker system is optimized to actively explore the environment as rodents run forward.

The total extent of tactile information gathered by the whisker system is not fully known, but three broad categories have been studied in depth: whisker touch, object localization, and texture discrimination. Foremost, the whisker system is exquisitely sensitive to touch. This involves passive touch, when stationary whiskers are deflected due to applied force (Ferezou et al., 2007; Hutson and Masterton, 1986; McGuire et al., 2016; Ollerenshaw et al., 2012, 2014; Sachidhanandam et al., 2013; Stüttgen and Schwarz, 2008; Stüttgen et al., 2006; Waiblinger et al., 2015a) and active touch, when whiskers contact an object during whisking (Crochet and Petersen, 2006; Ferezou et al., 2006; Hires et al., 2015; O'Connor et al., 2010a, 2010b; Szwed et al., 2003). In both cases, forces due to the mechanical properties of the touch event are rapidly transduced at the whisker follicle and conveyed to L4. When combined with whisker position signals, rodents can interpret whisker touch in head-centered coordinates to decode object location. Localization coding has been studied in the context of bilateral distance comparisons (Knutsen et al., 2006; Krupa et al., 2004; Shuler et al., 2002), radial distance (Sofroniew et al., 2014, 2015; Szwed et al., 2006), and rostrocaudal distance (Kleinfeld and Deschênes, 2011; Mehta et al., 2007; Szwed et al., 2003). Of these, the best understood is rostrocaudal spatial coding, which can be reconstructed from whisker phase signals in S1, and set point and whisk amplitude envelope signals from primary motor cortex (Kleinfeld and Deschênes, 2011). The last category, texture discrimination, is particularly relevant to the current work and we discuss it in more detail below.

Texture encoding and the slip hypothesis

In 1989 researchers showed that rats could discriminate rough and smooth textures using their vibrissa (Guić-Robles et al., 1989), which was quickly followed by studies showing that this discrimination can be as fine as discriminations performed by human fingertips (Carvell and Simons, 1990). Studies using high-speed whisker imaging revealed that rodent whiskers moved in discontinuous jumps and starts while traversing rough surfaces in artificial (muscle stimulated) whisking (Arabzadeh et al., 2005) and later, in awake animal whisking (Ritt et al., 2008; Wolfe et al., 2008). These transient, high-acceleration kinematic events, called stick-slips, also drive sparse, temporally precise spikes in S1 (Jadhav et al., 2009). This led to the slip hypothesis of texture encoding (Jadhav and Feldman, 2010; Schwarz, 2016; Waiblinger et al., 2015b), which proposes that increased whisker slips drive an increase in S1 spikes, allowing perceptual discrimination between rough and smooth surfaces. By contrast, other studies have suggested that it is the integrated vibrotactile intensity, parameterized as vibration amplitude and frequency, that enables texture discrimination (Arabzadeh et al., 2005; Gerdjikov et al., 2010; McGuire et al., 2016). Therefore, the exact importance of discrete kinematic events in texture discrimination is still unknown. One weakness of the slip hypothesis has been that no studies have tested whether rough and smooth stimuli can be decoded based on slips imaged in actively discriminating rodents. Further, no studies have shown that the spikes from these kinematics actually

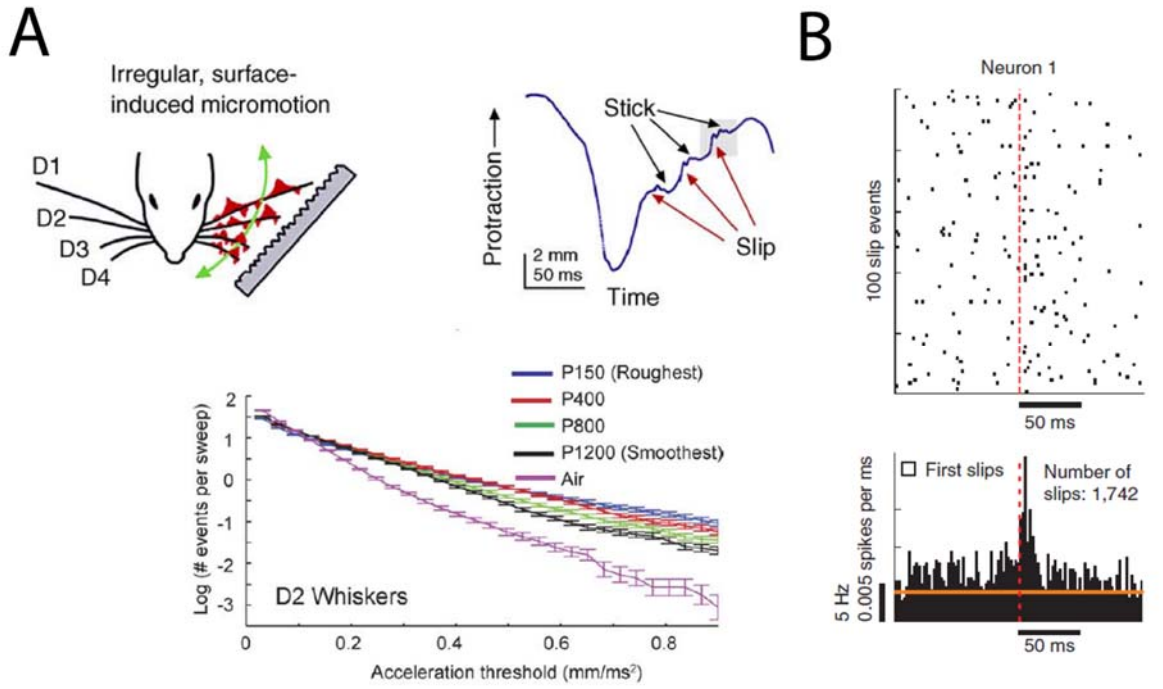

Figure 1.3. Slips encode surface roughness. (A) (Adapted from: Jadhav and Feldman, 2010; Wolfe et al., 2008). Top: Schematic of irregular micromotions on rough surface (Left), and a whisker trace illustrating sticks and slips (Right). Bottom: Quantification of the number of slips per sweep of the D2 whisker vs. slip amplitude. Lines represent slips on a range of tactile roughness from P150 sandpaper to whisking in Air. Note: the number of slips increases at every amplitude with increases in surface roughness. (B) (Adapted from: Jadhav et al., 2009). Top: Raster of spikes in one neuron aligned to peak slip (n=100 slips). Bottom: PSTH of spikes relative to slip peak.

contribute to the neural decodability of smooth and rough stimuli on a single trial basis. In Chapter 3, we measure both of these properties to show that slips do predict surface roughness and make a large contribution to the neural code for roughness in actively discriminating mice.

Tactile shape encoding

Just as whisker touch and whisker position allow the whisker system to perform object localization, a combination of whisker slips and whisker position could allow the whisker system to encode surface shapes. More broadly, whether slips occur frequently enough, and with sufficient spatial precision to represent local spatial features of objects is unknown (Schwarz, 2016). When stimuli with periodic spatial features have been used as textures in previous experiments (Carvell and Simons, 1995; Jenks et al., 2010; Zuo et al., 2011), the absolute spatial location of whisker kinematics on the stimuli has not been quantified. Spatiotemporally precise slips could contribute to a temporal coding of space (Ahissar and Arieli, 2001; Gamzu and Ahissar, 2001), similar to when primates actively palpate a ridged surface (Sinclair and Burton, 1991). This is in contrast to

spatial codes as conceived in passive primate skin indentation (Katz, 1989/1925), where shape is instantaneously transduced by parallel mechanoreceptors and conveyed via "labeled lines." Labeled line spatial coding appears to play a role in non-rodent whisker systems like the Etruscan shrew, where macroscopic shapes are encoded instantaneously via simultaneous deflections of several whiskers (Anjum et al., 2006; Munz et al., 2010), but has not been observed in the macrovibrissa of rodents (but see putative microvibrissa mechanism: Brecht et al., 1997). In Chapter 3, we explore the feasibility of representing spatial features in time using slips and slip-evoked spikes, and test for spatial frequency tuning using a set of differently spaced raised tactile gratings.

References

Ahissar, E., and Arieli, A. (2001). Figuring Space by Time. Neuron *32*, 185–201.

Anjum, F., Turni, H., Mulder, P.G.H., van der Burg, J., and Brecht, M. (2006). Tactile guidance of prey capture in Etruscan shrews. Proc. Natl. Acad. Sci. U. S. A. *103*, 16544–16549.

Arabzadeh, E., Zorzin, E., and Diamond, M.E. (2005). Neuronal encoding of texture in the whisker sensory pathway. PLoS Biol. *3*, e17.

Aronoff, R., Matyas, F., Mateo, C., Ciron, C., Schneider, B., and Petersen, C.C.H. (2010). Long-range connectivity of mouse primary somatosensory barrel cortex. Eur. J. Neurosci. *31*, 2221–2233.

Brecht, M., Preilowski, B., and Merzenich, M.M. (1997). Functional architecture of the mystacial vibrissae. Behav. Brain Res. *84*, 81–97.

Carvell, G., and Simons, D.J. (1995). Task-and subject-related differences in sensorimotor behavior during active touch. Somatosens. Mot. Res. *12*, 1–9.

Carvell, G.E., and Simons, D.J. (1990). Biometric analyses of vibrissal tactile discrimination in the rat. J. Neurosci. *10*, 2638–2648.

Clancy, K.B., Koralek, A.C., Costa, R.M., Feldman, D.E., and Carmena, J.M. (2014). Volitional modulation of optically recorded calcium signals during neuroprosthetic learning. Nat Neurosci *advance on*.

Clancy, K.B., Schnepel, P., Rao, A.T., and Feldman, D.E. (2015). Structure of a single whisker representation in layer 2 of mouse somatosensory cortex. J. Neurosci. *35*, 3946–3958.

Constantinople, C.M., and Bruno, R.M. (2013). Deep cortical layers are activated directly by thalamus. Science (80-.). *1591*, 1591–1594.

Crochet, S., and Petersen, C.C.H. (2006). Correlating whisker behavior with membrane potential in barrel cortex of awake mice. Nat. Neurosci. *9*, 608–610.

Diamond, M.E. (2010). Texture sensation through the fingertips and the whiskers. Curr. Opin. Neurobiol. *20*, 319–327.

Ebara, S., Kumamoto, K., Matsuura, T., Mazurkiewicz, J.E., and Rice, F.L. (2002). Similarities and differences in the innervation of mystacial vibrissal follicle-sinus complexes in the rat and cat: a confocal microscopic study. J. Comp. Neurol. *449*, 103–119.

Feldmeyer, D., Lübke, J., and Sakmann, B. (2006). Efficacy and connectivity of intracolumnar pairs of layer 2/3 pyramidal cells in the barrel cortex of juvenile rats. J. Physiol. *575*, 583–602.

Ferezou, I., Bolea, S., and Petersen, C.C.H. (2006). Visualizing the cortical representation of whisker touch: voltage-sensitive dye imaging in freely moving mice. Neuron *50*, 617–629.

Ferezou, I., Haiss, F., Gentet, L.J., Aronoff, R., Weber, B., and Petersen, C.C.H. (2007). Spatiotemporal dynamics of cortical sensorimotor integration in behaving mice. Neuron *56*, 907–923.

Fries, P. (2009). Neuronal gamma-band synchronization as a fundamental process in cortical computation. Annu. Rev. Neurosci. *32*, 209–224.

Gamzu, E., and Ahissar, E. (2001). Importance of temporal cues for tactile spatial-frequency discrimination. J. Neurosci. *21*, 7416–7427.

Gerdjikov, T. V., Bergner, C.G., Stüttgen, M.C., Waiblinger, C., and Schwarz, C. (2010). Discrimination of vibrotactile stimuli in the rat whisker system: behavior and neurometrics. Neuron *65*, 530–540.

Ghazanfar, A.A., and Nicolelis, M. a (1999). Spatiotemporal properties of layer V neurons of the rat primary somatosensory cortex. Cereb. Cortex *9*, 348–361.

Guić-Robles, E., Valdivieso, C., and Guajardo, G. (1989). Rats can learn a roughness discrimination using only their vibrissal system. Behav. Brain Res. *31*, 285–289.

Haidarliu, S., Kleinfeld, D., Deschênes, M., and Ahissar, E. (2015). The Musculature That Drives Active Touch by Vibrissae and Nose in Mice. Anat. Rec. *298*, 1347–1358.

Hattox, A.M., and Nelson, S.B. (2007). Layer V neurons in mouse cortex projecting to different targets have distinct physiological properties. J. Neurophysiol. *98*, 3330–3340.

Hires, S.A., Gutnisky, D.A., Yu, J., O'Connor, D.H., and Svoboda, K. (2015). Low-noise encoding of active touch by layer 4 in the somatosensory cortex. Elife *4*, 1–18.

Hires, S.A. ndrew, Pammer, L., Svoboda, K., and Golomb, D. (2013). Tapered whiskers are required for active tactile sensation. Elife *2*, e01350.

Hubel, D.H., and Wiesel, T.N. (1959). Receptive fields of single neurones in the cat's striate cortex. J. Physiol. *148*, 574–591.

Hutson, K.A., and Masterton, R.B. (1986). The sensory contribution of a single vibrissa's cortical barrel. J. Neurophysiol. *56*, 1196–1223.

Jadhav, S.P., and Feldman, D.E. (2010). Texture coding in the whisker system. Curr. Opin. Neurobiol. *20*, 313–318.

Jadhav, S.P., Wolfe, J., and Feldman, D.E. (2009). Sparse temporal coding of elementary tactile features during active whisker sensation. Nat. Neurosci. *12*, 792–800.

Jenks, R.A., Vaziri, A., Boloori, A.-R., and Stanley, G.B. (2010). Self-motion and the shaping of sensory signals. J Neurophysiol *103*, 2195–2207.

Katz, D. (1989). The World of Touch (Hillsdale, NJ: Erlbaum).

Kleinfeld, D., and Deschênes, M. (2011). Neuronal basis for object location in the vibrissa scanning sensorimotor system. Neuron *72*, 455–468.

Knutsen, P.M., Pietr, M., and Ahissar, E. (2006). Haptic object localization in the vibrissal system: behavior and performance. J. Neurosci. *26*, 8451–8464.

Krupa, D.J., Wiest, M.C., Shuler, M.G., Laubach, M., and Nicolelis, M. a L. (2004). Layer-specific somatosensory cortical activation during active tactile discrimination. Science *304*, 1989–1992.

Leiser, S.C., and Moxon, K.A. (2007). Responses of Trigeminal Ganglion Neurons during Natural Whisking Behaviors in the Awake Rat. Neuron *53*, 117–133.

Van Der Loos, H. (1976). Barreloids in mouse somatosensory thalamus. Neurosci. Lett. *2*, 1–6.

Lübke, J., and Feldmeyer, D. (2007). Excitatory signal flow and connectivity in a cortical column: focus on barrel cortex. Brain Struct. Funct. *212*, 3–17.

Manns, I.D., Sakmann, B., and Brecht, M. (2004). Sub- and suprathreshold receptive field properties of pyramidal neurones in layers 5A and 5B of rat somatosensory barrel cortex. J. Physiol. *556*, 601–622.

Maricich, S.M., Morrison, K.M., Mathes, E.L., and Brewer, B.M. (2012). Rodents rely on Merkel cells for texture discrimination tasks. J Neurosci *32*, 3296–3300.

McGuire, L.M., Telian, G., Laboy-Juárez, K.J., Miyashita, T., Lee, D.J., Smith, K.A., and Feldman, D.E. (2016). Short Time-Scale Sensory Coding in S1 during Discrimination of Whisker Vibrotactile Sequences. PLOS Biol. *14*, e1002549.

Mehta, S.B., Whitmer, D., Figueroa, R., Williams, B. a, and Kleinfeld, D. (2007). Active spatial perception in the vibrissa scanning sensorimotor system. PLoS Biol. *5*, e15.

Moore, J.D., Mercer Lindsay, N., Deschênes, M., and Kleinfeld, D. (2015). Vibrissa Self-Motion and Touch Are Reliably Encoded along the Same Somatosensory Pathway from Brainstem through Thalamus. PLoS Biol. *13*, 1–28.

Munz, M., Brecht, M., and Wolfe, J. (2010). Active touch during shrew prey capture. Front. Behav. Neurosci. *4*, 191.

O'Connor, D.H., Peron, S.P., Huber, D., Svoboda, K., Connor, D.H.O., Peron, S.P., Huber, D., Svoboda, K., O'Connor, D.H., Peron, S.P., et al. (2010a). Neural activity in barrel cortex underlying vibrissa-based object localization in mice. Neuron *67*, 1048–1061.

O'Connor, D.H., Clack, N.G., Huber, D., Komiyama, T., Myers, E.W., and Svoboda, K. (2010b). Vibrissa-based object localization in head-fixed mice. J. Neurosci. *30*, 1947–1967.

Oberlaender, M., Boudewijns, Z.S.R.M., Kleele, T., Mansvelder, H.D., Sakmann, B., and de Kock, C.P.J. (2011). Three-dimensional axon morphologies of individual layer 5 neurons indicate cell type-specific intracortical pathways for whisker motion and touch. Proc. Natl. Acad. Sci. U. S. A. *108*, 4188–4193.

Ollerenshaw, D.R., Bari, B.A., Millard, D.C., Orr, L.E., Wang, Q., and Stanley, G.B. (2012). Detection of tactile inputs in the rat vibrissa pathway . J. Neurophysiol. *108*, 479–490.

Ollerenshaw, D.R., Zheng, H.J. V, Millard, D.C., Wang, Q., and Stanley, G.B. (2014). The adaptive trade-off between detection and discrimination in cortical representations and behavior. Neuron *81*, 1152–1164.

Pluta, S., Naka, A., Veit, J., Telian, G., Yao, L., Hakim, R., Taylor, D., and Adesnik, H. (2015). A direct translaminar inhibitory circuit tunes cortical output. Nat. Neurosci. *18*, 1631–1640.

Pokay, M. (1991). The Barrelettes-Vibrissal Representations in the Brainstem Trigeminal Complex of the Mouse. I. Normal Structural Organization. J. Comp. Neurol. *199*, 161–199.

Ritt, J.T., Andermann, M.L., and Moore, C.I. (2008). Embodied information processing: vibrissa mechanics and texture features shape micromotions in actively sensing rats. Neuron *57*, 599–613.

Sachidhanandam, S., Sreenivasan, V., Kyriakatos, A., Kremer, Y., and Petersen, C.C.H. (2013). Membrane potential correlates of sensory perception in mouse barrel cortex. Nat. Neurosci. *16*, 1671–1677.

Sarid, L., Feldmeyer, D., Gidon, A., Sakmann, B., and Segev, I. (2015). Contribution of Intracolumnar Layer 2/3-to-Layer 2/3 Excitatory Connections in Shaping the Response to Whisker Deflection in Rat Barrel Cortex. Cereb. Cortex *25*, 849–858.

Schwarz, C. (2016). The Slip Hypothesis: Tactile Perception and its Neuronal Bases. Trends Neurosci. *39*, 449–462.

Shuler, M.G., Krupa, D.J., and Nicolelis, M. a L. (2002). Integration of bilateral whisker stimuli in rats: role of the whisker barrel cortices. Cereb. Cortex *12*, 86–97.

Sinclair, R.J., and Burton, H. (1991). Neuronal activity in the primary somatosensory cortex in monkeys (Macaca mulatta) during active touch of textured surface gratings: responses to groove width, applied force, and velocity of motion. J. Neurophysiol. *66*, 153–169.

Sofroniew, N.J., Cohen, J.D., Lee, a. K., and Svoboda, K. (2014). Natural Whisker-Guided Behavior by Head-Fixed Mice in Tactile Virtual Reality. J. Neurosci. *34*, 9537–9550.

Sofroniew, N.J., Vlasov, Y. a, Andrew Hires, S., Freeman, J., and Svoboda, K. (2015). Neural coding in barrel cortex during whisker-guided locomotion. Elife *4*, 1–36.

Stern, E.A., Maravall, M., and Svoboda, K. (2001). Rapid development and plasticity of layer 2/3 maps in rat barrel cortex in vivo. Neuron *31*, 305–315.

Stüttgen, M.C., and Schwarz, C. (2008). Psychophysical and neurometric detection performance under stimulus uncertainty. Nat. Neurosci. *11*, 1091–1099.

Stüttgen, M.C., Rüter, J., and Schwarz, C. (2006). Two psychophysical channels of whisker deflection in rats align with two neuronal classes of primary afferents. J. Neurosci. *26*, 7933–7941.

Szwed, M., Bagdasarian, K., and Ahissar, E. (2003). Encoding of vibrissal active touch. Neuron *40*, 621–630.

Szwed, M., Bagdasarian, K., Blumenfeld, B., Barak, O., Derdikman, D., and Ahissar, E. (2006). Responses of trigeminal ganglion neurons to the radial distance of contact during active vibrissal touch. J. Neurophysiol. *95*, 791–802.

Vincent, S.B. (1912). The functions of the vibrissae in the behavior of the white rat.

Waiblinger, C., Brugger, D., and Schwarz, C. (2015a). Vibrotactile discrimination in the rat whisker system is based on neuronal coding of instantaneous kinematic cues. Cereb. Cortex *25*, 1093–1106.

Waiblinger, C., Brugger, D., Whitmire, C.J., Stanley, G.B., and Schwarz, C. (2015b). Support for the slip hypothesis from whisker-related tactile perception of rats in a noisy environment. Front. Integr. Neurosci. *9*, e53.

Wolfe, J., Hill, D.N., Pahlavan, S., Drew, P.J., Kleinfeld, D., and Feldman, D.E. (2008). Texture coding in the rat whisker system: slip-stick versus differential resonance. PLoS Biol. *6*, e215.

Woolsey, T.A. (2010). Sensorimotor Integration: Barrels, Vibrissae and Topographic Representations. Encycl. Neurosci. 601–606.

Woolsey, T.A.. van D.L.H. (1970). The structural organization of layer IV in the somatosensory region (S1) of mouse cerebral. Brain Res. *17*, 205–242.

Yu, J., Gutnisky, D.A., Hires, S.A., and Svoboda, K. (2016). Layer 4 fast-spiking

interneurons filter thalamocortical signals during active somatosensation. Nat. Neurosci. *19*, 1–14.

Zhang, S., Xu, M., Kamigaki, T., Do, J., Chang, W.-C., Jenvay, S., Miyamichi, K., Luo, L., and Dan, Y. (2014). Long-range and local circuits for top-down modulation of visual cortex processing. Science (80-.). *345*, 660–665.

Zuo, Y., Perkon, I., and Diamond, M.E. (2011). Whisking and whisker kinematics during a texture classification task. Philos. Trans. R. Soc. Lond. B. Biol. Sci. *366*, 3058–3069.

Chapter 2

Plasticity of Recurrent L2/3 Inhibition and Gamma Oscillations by Whisker Experience

Yu R. Shao, Brian R. Isett, Toshio Miyashita, Jason Chung, Olivia Pourzia, Robert J. Gasperini, and Daniel E. Feldman

This chapter, in full, is a republication of the material as it appears in Shao,Y.R., Isett, B.R., Miyashita, T., Chung, J., Pourzia, O., Gasperini, R.J., and Feldman, D.E. 2013. Plasticity of recurrent L2/3 inhibition and gamma oscillations by whisker experience. *Neuron*, 80, 210-222.

2.1 Summary

Local recurrent networks in neocortex are critical nodes for sensory processing, but their regulation by experience is much less understood than for long-distance (translaminar or cross-columnar) projections. We studied local L2/3 recurrent networks in rat somatosensory cortex during deprivation-induced whisker map plasticity, by expressing channelrhodopsin-2 (ChR2) in L2/3 pyramidal cells and measuring light-evoked synaptic currents in ex vivo S1 slices. In columns with intact whiskers, brief light impulses evoked recurrent excitation and supralinear inhibition. Deprived columns showed modestly reduced excitation and profoundly reduced inhibition, providing a

circuit locus for disinhibition of whisker-evoked responses observed in L2/3 in vivo. Slower light ramps elicited sustained gamma frequency oscillations, which were nearly abolished in deprived columns. Reduction in gamma power was also observed in spontaneous LFP oscillations in L2/3 of deprived columns in vivo. Thus, L2/3 recurrent networks are a powerful site for homeostatic modulation of excitation-inhibition balance and regulation of gamma oscillations.

2.2 Introduction

Experience regulates multiple components of cortical microcircuits to mediate sensory map plasticity. Plasticity in long-range excitatory circuits (thalamocortical, translaminar and cross-columnar) is well characterized and often follows Hebbian rules in which deprived inputs weaken or lose synapses, and spared inputs strengthen or add synapses (e.g., Antonini and Stryker, 1993; Allen et al., 2003; Trachtenberg and Stryker 2001; Broser et al., 2008; Yamahachi et al., 2009). In contrast, the contribution of local recurrent circuits to cortical plasticity is much less understood. Local recurrent circuits help generate sensory tuning (Schummers et al., 2002) and include both recurrent excitation and inhibition whose ratio regulates sensory gain and information flow (Adesnik and Scanziani, 2010; Atallah et al., 2012). Recurrent inhibition from fast-spiking (FS) interneurons generates gamma oscillations (30–90 Hz), which synchronize local spikes and may promote formation of cell assemblies and information transfer to higher areas (Fries, 2009; Buzsaki and Wang, 2012). Thus, local recurrent circuits may be a powerful nexus for regulation of cortical information processing. Experience can alter some components of recurrent circuits (Maffei et al., 2004, 2006; Cheetham et al., 2007; Maffei and Turrigiano 2008), but the net functional effect, and whether this plasticity is functionally distinct from plasticity in long-range circuits, is not known. Local circuits are intermixed with long-range axons and therefore cannot be studied selectively using classical extracellular stimulation. Here, we use optogenetics to selectively activate local recurrent circuits and measure the functional changes that accompany map plasticity.

We focus on L2/3 of somatosensory cortex, which is a major site of receptive field reorganization during whisker map plasticity (Glazewski and Fox, 1996). Rats have five rows of whiskers, termed A–E, represented in S1 by an isomorphic map of cortical columns. Thalamocortical input arrives principally in L4, which projects to L2/3. L2/3 pyramidal (PYR) cells make glutamatergic synapses on nearby PYR cells (recurrent excitation) and on L2/3 and L5 interneurons that inhibit L2/3 PYR cells (recurrent inhibition) (Reyes et al., 1998; Kapfer et al., 2007; Lefort et al., 2009). Plucking the D row of whiskers in juvenile animals causes whisker map plasticity in which spiking responses to deprived whiskers are depressed in L2/3 of deprived columns, while L4 remains relatively unaffected (Drew and Feldman, 2009; Jacob et al., 2012). Major loci of this Hebbian weakening are the L4/L2/3 feedforward projection (Allen et al., 2003; Shepherd et al., 2003; Bender et al., 2006) and L2/3 cross-columnar projections (Broser et al., 2008). How deprivation alters L2/3 recurrent circuit function is unknown.

We hypothesized that local recurrent L2/3 circuits are a major site of

compensatory (homeostatic) plasticity that stabilizes, rather than weakens, cortical firing during whisker deprivation. This could occur if deprivation preferentially weakened recurrent inhibition relative to excitation. Such disinhibition could explain the reduction in whisker-evoked inhibition observed in L2/3 pyramidal cells in vivo (Gambino and Holtmaat, 2012). Homeostasis is critical for cortical function but remains much less understood than Hebbian plasticity (Turrigiano, 2012), and identification of L2/3 recurrent circuits as a major site for homeostatic plasticity would be novel. If a referential loss of inhibition occurs within recurrent L2/3 circuits, it may also have an effect on gamma oscillations. Plasticity of gamma oscillations is a predicted effect of synaptic plasticity in cortical fast-spiking networks (Paik and Glaser, 2010) but has not yet been directly observed.

2.3 Results

We studied functional activation of L2/3 recurrent circuits by optogenetic activation of L2/3 pyramidal cells using channelrhodopsin-2 (ChR2). (L2/3 recurrent circuits cannot be selectively activated by extracellular electrical stimulation because of intermixed feedforward and cross-columnar axons.) ChR2(H134R)-EYFP fusion protein (Nagel et al., 2005), cytosolic GFP, and the red fluorescent protein DsRed were

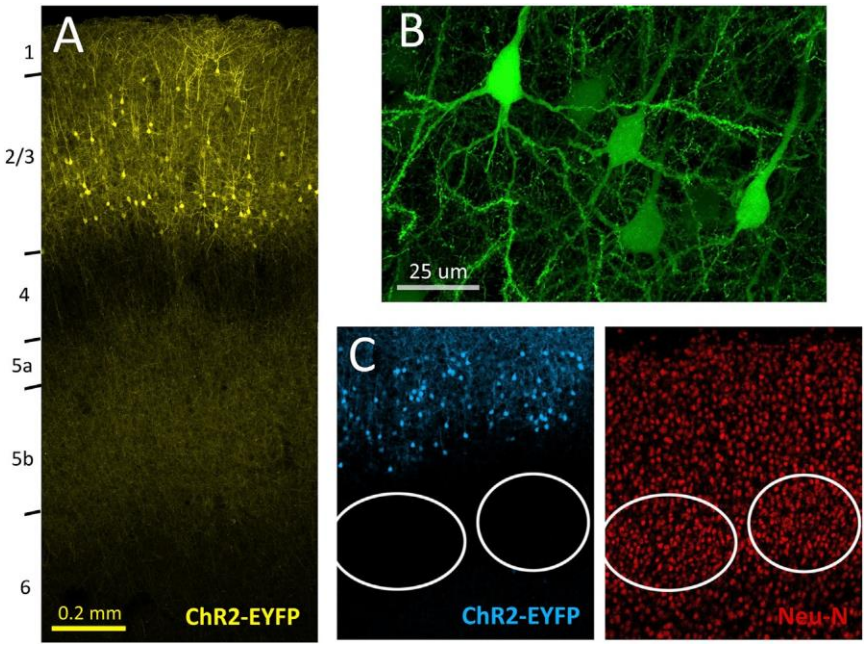

Figure 2.1. ChR2 Expression in L2/3 Pyramidal Neurons following In Utero Electroporation (A) ChR2-EYFP expression in S1 of a P24 rat, showing somatodendritic labeling in L2/3 pyramidal cells and axonal branches in L2/3 and L5. Laminar boundaries were determined from DAPI staining (data not shown). (B) Labeled pyramidal cells. (C) Double immunostaining for ChR2-EYFP and the neuronal marker Neu-N. Ovals are L4 barrels.

coexpressed (using three independent plasmids) in L2/3 pyramidal cells by in utero DNA electroporation of Long-Evans rat embryos at E18 (Saito and Nakatsuji, 2001; Tabata and Nakajima, 2001; Petreanu et al., 2007; Miyashita et al., 2010). The separate GFP plasmid was needed to drive sufficient fluorescence for transcranial identification of P1 pups with strong S1 expression. We confirmed histologically that fluorescence expression was confined to L2/3 pyramidal cells and their axons, with no expression in L4 or L5 neurons (Figures 1A and 1B). As expected, 100% of fluorescent cells had pyramidal morphology (n = 399 neurons, four histological sections, two rats). Overall, 21.1% ± 0.9% of L2/3 neurons (identified by immunostaining for Neu-N) also expressed fluorescence in the EYFP/GFP emission band (Figure 2.1C) (n = 10 rats, 37 columns), consistent with a prior study in mouse S1 (Adesnik and Scanziani, 2010). Linear spectral unmixing of GFP and EYFP signals (Zeiss 780 confocal with multispectral detector) confirmed strong EYFP expression in axonal and dendritic membranes (data not shown).

Optogenetic activation of L2/3 recurrent circuits

Circuit function was studied in acute S1 slices prepared at P17–P21. Slices were cut in the ‘‘across-row’’ plane that allows identification of columns corresponding to A–E whisker rows using transillumination (Finnerty et al., 1999). Whole-cell recordings were targeted to presumptive ChR2-expressing or ChR2-nonexpressing cells based on DsRed fluorescence. This approach avoids unwanted ChR2 activation by GFP excitation light. We confirmed in histological sections that 94% ± 1% of DsRed+ L2/3 pyramidal cells also exhibited fluorescence in the EYFP/GFP emission band (n = 1,421 neurons, 37 columns, 10 rats). Moreover, all DsRed+ cells exhibited direct ChR2-mediated photocurrent when patched (see below). Thus, single cells expressed multiple plasmids, and DsRed fluorescence was a valid indicator for putative ChR2+ neurons.

Only slices with strong, uniform expression of DsRed across all S1 columns were used (Figure 2.2A). A 443 nm blue laser beam (CrystaLaser DL-445-040) was shaped using a pinhole and focusing optics and was routed through a 43 air objective to the slice. Beam diameter (2 SD of Gaussian profile) was either 312 mm (spike threshold experiment) or 238 mm (synaptic physiology experiments), both of which fit in a single column (diameter 375–500 mm; Wimmer et al., 2010).

We first measured ChR2-elicited spike thresholds to determine the light stimulation parameters that achieve single-column photostimulation in L2/3. We made whole-cell current clamp recordings from DsRed+ (putative ChR2+) neurons (n = 13) in L2/3 of the C column and applied 2 ms light pulses centered in L2/3 of either the C column or adjacent columns (Figure 2.2B). Synaptic transmission was intact, so that both direct photocurrent and network synaptic activation contributed to spiking. At each stimulation site, we identified the threshold photostimulation intensity required to elicit a single spike from V_{rest} (Figure 2.2C). In the home column, low-intensity light (0.2 ± .05 mW) evoked spikes in every DsRed+ neuron, with < 0.2 ms latency to initial

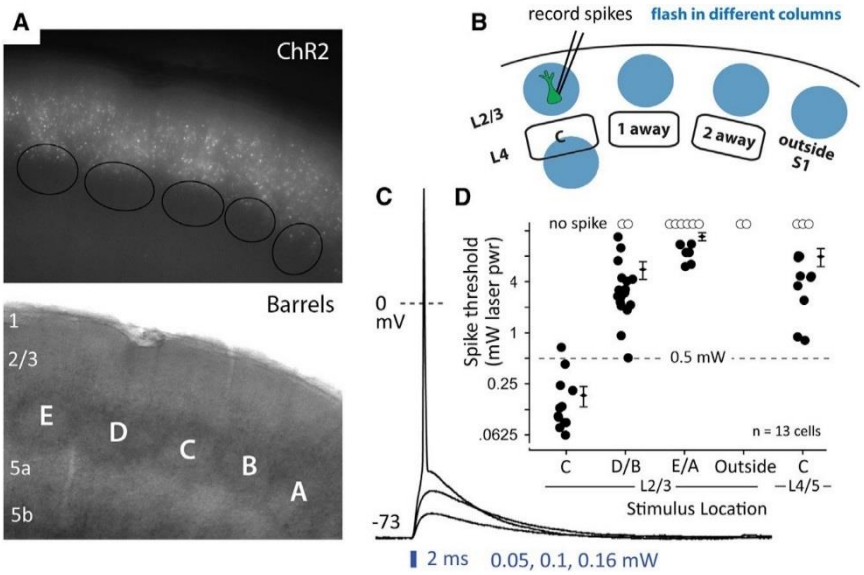

Figure 2.2. Single-Column Activation of L2/3 Recurrent Networks
(A) Ds-Red epifluorescence in a living slice, with barrels visualized by transillumination. (B) Schematic of the spike threshold experiment used to calibrate single-column stimulation. (C) Photostimulation-evoked depolarization and spiking in one DsRed+ pyramidal cell to light stimulation centered in L2/3 of the C column. (D) Photostimulation intensity required to evoke a spike as a function of photostimulus location. Each circle is a cell. Diamonds and error bars show population mean and SEM.

subthreshold) depolarization. This latency is too short to be mediated synaptically and is indicative of ChR2 expression in the recorded neuron (Cruikshank et al., 2010). Higher photostimulation intensity (>0.5 mW) was required to evoke spikes from stimulation sites in adjacent columns and at the L4-L5 border in the home column (Figure 2.2D). Thus, 2 ms light impulses of <0.5 mW in L2/3 drive spikes in L2/3 pyramidal cells only within a single S1 column. All subsequent experiments used light intensity within the column-specific range.

Synaptic responses from the L2/3 recurrent network

To measure the functional output of the L2/3 recurrent network, we made voltage-clamp recordings from DsRed-negative L2/3 pyramidal neurons and measured excitatory postsynaptic currents (EPSCs) and inhibitory postsynaptic current (IPSCs) evoked by light centered in L2/3 of the neuron's home column. D-APV (50 mM) and saclofen (100 mM) were bath applied to isolate AMPAR-EPSCs and GABAA-IPSCs. EPSCs and IPSCs were measured at -68 and 0 mV, respectively (ECl and EAMPA in our solutions). Unlike DsRed+ cells, which uniformly exhibited short-latency responses (<0.2 ms), most DsRed-cells exhibited long-latency responses (>1.5 ms) consistent with

network-mediated synaptic currents (Figure 2.3A). Synaptic responses were only analyzed in long-latency cells that lacked direct ChR2 photocurrent. We confirmed that

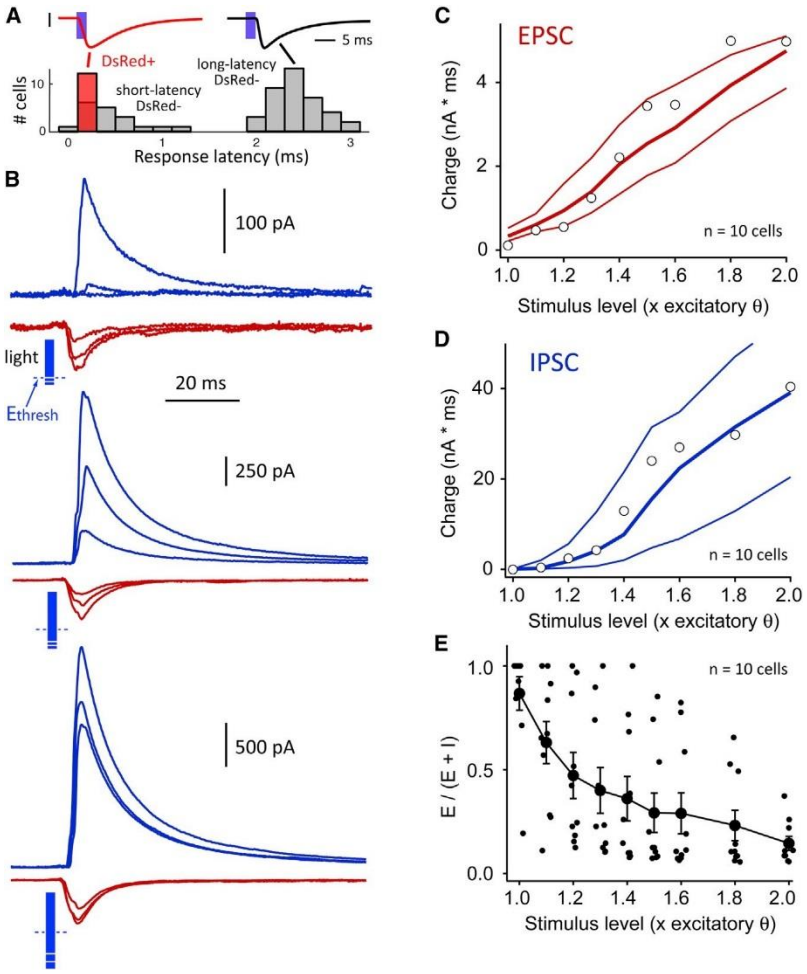

Figure 2.3. Activation of the Recurrent L2/3 Network by a 2 ms Light Pulse (A) Bimodal distribution of response latency allowed identification of directly light-responsive versus synaptically responsive cells. Gray bars, DsRed-negative cells under normal recording conditions. Red bar, DsRed+ cells with TTX, kynurenic acid, and PTX present in the bath (in addition to the standard APV and saclofen). (B) Recruitment of recurrent EPSCs (red) and IPSCs (blue) in an example neuron. Each trace is mean of 10–14 sweeps. Top: 1.0, 1.1, and 1.2 x E_{thresh}. Middle: 1.3, 1.4, and 1.5 x E_{thresh}. Bottom; 1.6, 1.8, and 2.03Ethresh. Blue bar length indicates photostimulus intensity relative to E_{thresh} (dashed line). Cell was located in B column. (C and D) EPSC and IPSC charge as a function of light intensity, for all cells in B columns (n = 10 cells). Open symbols show cell in (B). Lines are bootstrapped 25th, 50th, and 75th percentiles. (E) Fractional excitatory charge for all cells in B columns. Error bars are SEM.

ChR2-evoked EPSCs were blocked by NBQX (10 mM), but not gabazine (1 mM), whereas IPSCs were blocked by both NBQX and gabazine (applied independently), as expected for disynaptic GABA-A inhibition (n = 4 cells). TTX (1 mM) completely blocked ChR2-evoked currents (n = 4 cells), indicating that synaptic currents were not due to direct ChR2-mediated release from terminals. Pharmacologically isolated EPSCs and IPSCs reversed at 0.4 ± 2.5 mV and -66.7 ± 0.8 mV (n = 5 and 6 cells), confirming that recording at -68 and 0 mV isolated EPSCs and IPSCs, respectively.

Prior studies of synaptic activation within the local L2/3 recurrent network in S1 focused on output of a single pyramidal cell (Reyes et al., 1998; Feldmeyer et al., 2006; Lefort et al., 2009), recruitment of inhibition by spiking of 1–2 pyramidal cells (Kapfer et al., 2007), or excitation-inhibition balance evoked by strong or sustained network activation (Adesnik and Scanziani, 2010; Mateo et al., 2011). How progressive activation of the L2/3 pyramidal cell population recruits recurrent excitation and inhibition is unknown. We therefore first characterized recruitment of recurrent excitation and inhibition in response to increasing photostimulation of the ChR2-expressing L2/3 pyramidal cell population. Experiments were performed in whisker-intact B columns from P17–P21 rats that had the D row of whiskers plucked for plasticity experiments (see below).

For each neuron (n = 10), we identified the excitatory stimulation threshold (E_{thresh}), defined as the photostimulation intensity that reliably evoked a detectable EPSC. We used a 2 ms light pulse to mimic transient sensory-driven spiking (Simons, 1978; Jadhav et al., 2009). IPSCs were invariably absent at E_{thresh}. Increasing photostimulation intensity (in multiples from 1.0 to
x E_{thresh}) evoked steadily larger EPSCs (quantified as charge integrated over the first 50 ms of the response) but more steeply larger IPSCs (Figures 3B–3D). IPSC charge increased particularly steeply between 1.0 and 1.4 x E_{thresh}, consistent with supralinear recruitment of a subset of recurrent inhibition (Kapfer et al., 2007). To compare relative recruitment of excitation and inhibition, we calculated fractional excitation (defined as E/(E + I)) at each stimulus intensity. Fractional excitation varied inversely with stimulus intensity, reflecting preferential recruitment of inhibition over excitation as L2/3 network activation increased (Figures 3C–3E).

To determine the relationship between light intensity and spiking in the L2/3 network, we first measured how E_{thresh} for ChR2-negative cells compares with spike threshold for ChR2-positive cells in the same column (n = 7 columns, 21 ChR2-cells, 20 ChR2+ cells). All co-columnar ChR2-cells had similar E_{thresh}, but intermixed ChR2+ cells showed a range of spike thresholds from 1.0 to 2.03 mean E_{thresh} for the ChR2-cells in that column. This is expected because each pyramidal cell receives excitatory synapses from many neighbors, so E_{thresh} in ChR2- cells must approximate the lowest spike threshold of local ChR2+ cells. As photostimulus intensity was increased from 1.0 to 2.03 mean column E_{thresh}, the fraction of ChR2+ cells that spiked increased nearly linearly, but ChR2- cells were not recruited to spike (0/15 cells, six columns). Thus, ChR2 stimulation does not drive positive-feedback recruitment of the L2/3 pyramidal cell network. This was due to powerful disynaptic IPSPs that prevented spiking in ChR2- pyramidal cells, as shown previously for ChR2 activation of the L2/3 network in vivo

(Mateo et al., 2011). Both fast-spiking (FS) and non-FS L2/3 interneurons are known to mediate this recurrent inhibition (Mateo et al., 2011).

Effects of whisker deprivation

To drive whisker map plasticity, the D row of whiskers was plucked from P12 until the day of recording (P17–P21). This manipulation drives weakening of principal whisker-evoked spiking responses in L2/3 of deprived columns, which is a major component of plasticity in juveniles (Glazewski and Fox, 1996; Feldman and Brecht, 2005; Drew and Feldman, 2009). To understand how L2/3 recurrent network function is altered by deprivation, we compared ChR2-evoked synaptic responses in deprived (D) columns with spared (B, C, and E) columns. Example cells from the B and D columns of

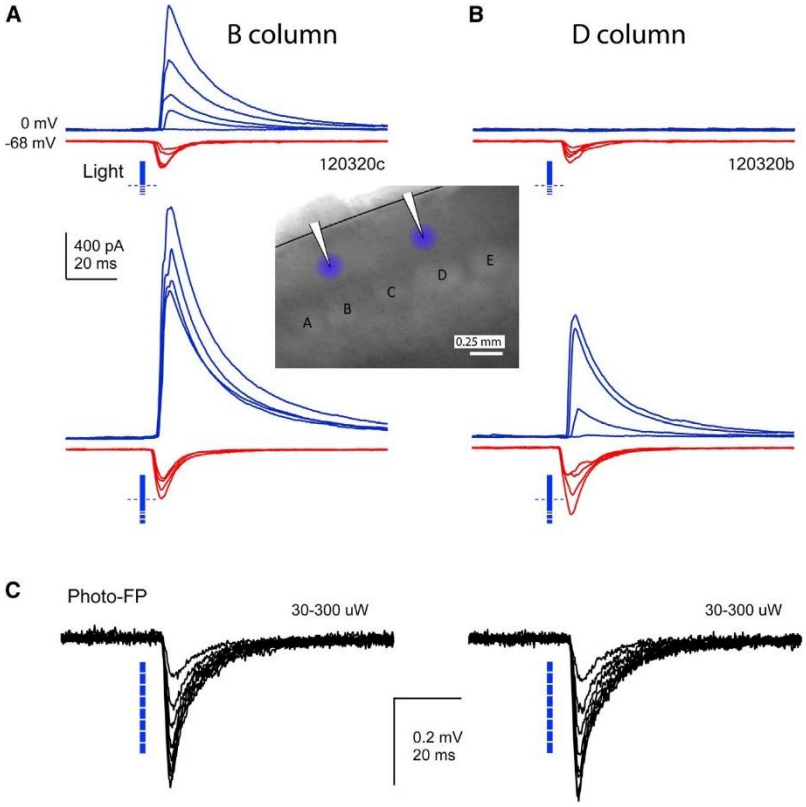

Figure 2.4. Effect of D-Row Deprivation on Two Representative Cells in B and D Columns of a Single Slice (A and B) IPSCs (blue) and EPSCs (red) recorded in response to 1.0 - 1.4 x E_{thresh} (top) and 1.5, 1.6, 1.8, and 2.0 x E_{thresh} (bottom). Inset: recording and photostimulus locations for these two neurons. (C) Photocurrent-LFPs recorded at the location of each neuron in the presence of TTX, kynurenic acid, and picrotoxin. Photocurrent-LFPs were recorded in response to the same series of photostimulation intensities (30–300 mW) and were identical in both columns.

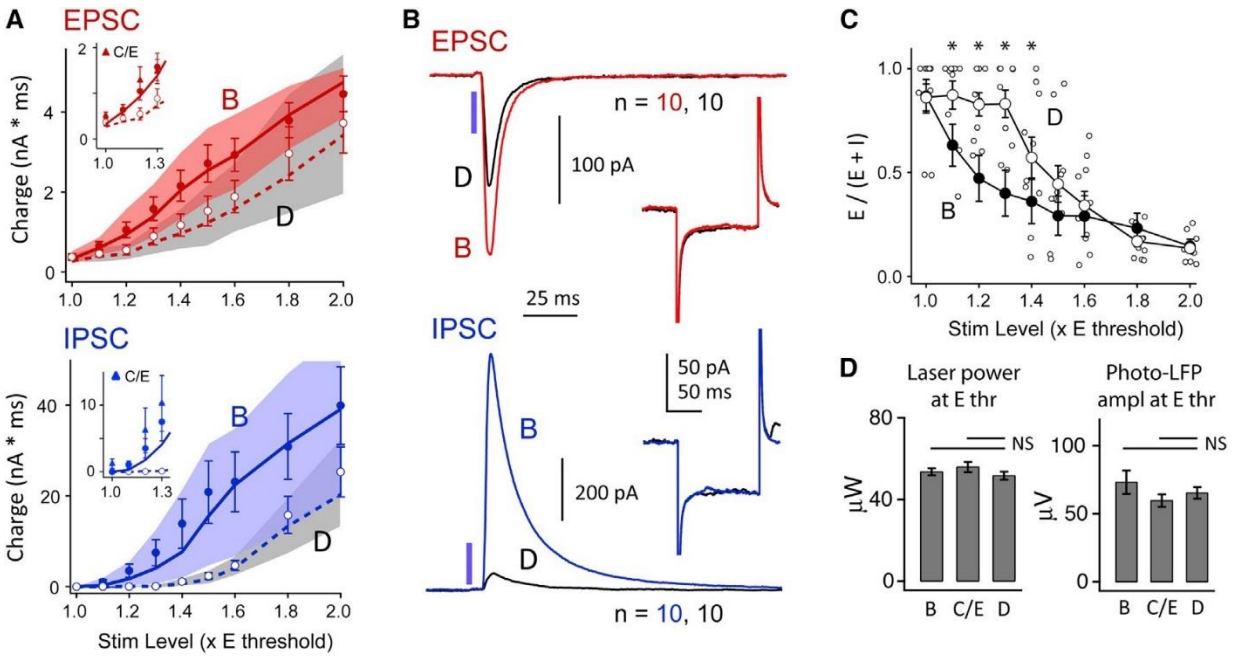

Figure 2.5. Effect of D-Row Deprivation on Synaptic Responses Elicited by 2 ms Light Pulse
(A) Recruitment of recurrent EPSCs and IPSCs in spared B versus deprived D columns. Circles: mean ± SEM. Lines and shaded region: median and 25th–75th quartiles. Insets: EPSCs and IPSCs measured in spared C and E columns (triangles), relative to B and D columns (circles and lines). (B) Mean population EPSC and IPSC at 1.4 x E_{thresh} in B and D columns (n = 10 cells each). Inset: the average response to a -5 mV current step was not altered by deprivation. (C) Fractional excitatory charge was higher in D columns, consistent with reduced IPSCs. *p < 0.05, Tukey HSD. B column mean (not individual cells) is replotted from Figure 2.3E. (D) Mean effective stimulation intensity was not different between B and D columns, as assessed by laser intensity required to elicit a threshold EPSC or by amplitude of photocurrent-LFP at E_{thresh}. Error bars are SEM.

a single slice are shown in Figure 2.4. In the B column, EPSCs grew slowly with photostimulation intensity, whereas IPSCs grew more steeply, so that inhibition dominated excitation for all photostimulation intensities >1.2 x E_{thresh}. In the D column, EPSCs were recruited similarly, but IPSCs were undetectable until 1.5 x E_{thresh}, and inhibition did not exceed excitation until 1.8 x E_{thresh}. To rule out differences in functional expression of ChR2 between columns, we recorded the local field potential evoked by photostimulation in the presence of TTX, kynurenic acid, picrotoxin, D-APV, and saclofen to block spikes and fast synaptic transmission. This ‘‘photocurrent-local field potential (LFP)’’ reflects summed photocurrents from the population of pyramidal neurons near the field potential pipette. Photocurrent-LFP magnitude was identical in the two columns across a wide range of photostimulation intensities (Figure 2.4C).

Across cells, IPSC charge was smaller in D columns than B columns across a wide range of photostimulation intensity ($p < 0.000001$, two-factor ANOVA, B versus D, n = 10 cells each). The largest reductions were observed for $IPSC_{1.1}$ to $IPSC_{1.4}$, with 96.7% smaller IPSCs, on average, in D columns (Figure 2.5A). EPSC charge was also

reduced ($p < 0.001$, two-factor ANOVA, B versus D) but by a smaller amount ($EPSC_{1.1}$ - $EPSC_{1.4}$ were 41.5% smaller in D than in B columns). To take $IPSC_{1.4}$ and $EPSC_{1.4}$ as examples (Figure 2.5B), $IPSC_{1.4}$ was 92% smaller in D than in B columns (D: 69 ± 29 pA peak, 1.4 ± 0.4 nA*ms charge; B: 880 ± 352 pA peak, 13.9 ± 5.4 nA*ms charge, $p < 0.05$, t test). $EPSC_{1.4}$ was 45% smaller in D than in B columns (D: 139 ± 37 pA peak, 1.2 ± 0.27 nA*ms charge; B: 272 ± 53 pA peak, 2.2 ± 0.4 nA*ms charge, $p < 0.05$ and $p = 0.054$, respectively). In contrast, there was no difference in V_{rest} (B: -69.5 ± 1 mV D: -68.3 ± 2 mV, $p = 0.6$, t test) or R_{input} (at -68 mV, B: 329 ± 50 MU; D: 279 ± 31 MU, $p = 0.4$) (Figure 2.5B, inset). To determine whether excitation- inhibition ratio was changed, we calculated fractional excitation (E/(E + I)) for each cell and stimulation intensity. Fractional excitation was significantly higher in D than in B columns at 1.1–1.4x E_{thresh} (two-factor ANOVA, deprivation effect $p = 0.001$, interaction $p < 0.05$, Tukey HSD post hoc test, $p < 0.05$ for 1.1–1.4x E_{thresh}) (Figure 2.5C).

These changes in network-mediated synaptic responses occurred without systematic differences in direct ChR2 photocurrent (as assayed by photocurrent-LFP amplitude at E_{thresh}) or in the ability of light stimulation to drive initial EPSCs (assayed by the laser intensity required to elicit $EPSC_{1.0}$), indicating that ChR2 activation was equally effective in driving spikes in ChR2+ cells in D versus in B columns (Figure 2.5D). To determine whether deprivation effects were confined to deprived D columns, we recorded neurons (n = 10) in spared C and E columns, using a subset of stimulus intensities (1.0, 1.2, and 1.3x E_{thresh}). EPSCs and IPSCs in C and E columns were identical to B columns (ANOVA, $p > 0.05$) and were larger than in deprived D columns (ANOVA, $p < 0.05$) (Figure 2.5B, inset). Again, ChR2 activation was equally effective in C/E versus D columns (Figure 2.5D). Together, these results indicate that D-row deprivation powerfully reduced recurrent inhibition in L2/3 of deprived columns and more modestly reduced recurrent excitation.

Effect of Deprivation on Network Oscillations In Vitro

A major function of local recurrent inhibition, particularly via fast-spiking (FS) interneurons, is to synchronize spiking activity in the gamma frequency band, generating oscillations that are measurable both intracellularly and in local field potentials (Cardin et al., 2009; Buzsáki and Wang, 2012). Gamma oscillations have been proposed to promote synaptic integration, to select or bind cell assemblies, and to enable efficient area-to-area coupling for information transfer (Fries, 2009; Wang, 2010). Gamma occurs in awake rodent S1 (Sirota et al., 2008; Pritchett et al., 2012, Soc. Neurosci., abstract, 377.11), but its functional role there is not understood. We predicted that reduced recurrent inhibition may reduce the capacity of L2/3 to generate gamma oscillations.

To measure gamma oscillations within L2/3 recurrent circuits, we photostimulated with light ramps (1.2 s duration, linear ramp to 2.5, 5, or 10x E_{thresh}, 238 mm spot diameter centered in L2/3 of one column). Calibration experiments showed that these ramps evoked spikes largely in the home column. We made voltage-clamp recordings from DsRed-negative pyramidal cells and measured ramp-evoked EPSCs and IPSCs. In spared B columns (n = 16 cells), evoked IPSCs (measured at 0 mV)

showed prominent oscillations in the low gamma range (20–60 Hz), as shown previously in slices from whisker-intact mice (Adesnik and Scanziani, 2010). Evoked EPSCs (measured at -68 mV) had substantially less gamma power (Figure 2.6A). In deprived D columns (n = 16 cells), the sustained component of the IPSC was attenuated and gamma oscillations were substantially reduced (Figures 6B–BF). This was true for all ramp intensities. For $IPSC_{10}$, the sustained component (0.3–1.2 s after ramp onset) was 68% smaller in D columns (B: 142 ± 27 pA; D: 45 ± 17 pA) and had 70% less gamma power (mean in 20–60 Hz band; B: 43.4 ± 14 pA2; D: 12.9 ± 6.4 pA2 in D columns), whereas the early peak (0–0.3 s) was not much affected (B: 611 ± 73 pA; D: 497 ± 80 pA). Two-factor ANOVA (whisker experience 3 ramp intensity) showed a significant effect of experience on sustained IPSC amplitude ($p < 0.00005$) and gamma power ($p < 0.005$). In contrast, EPSC sustained amplitude was indistinguishable between spared and deprived columns (ANOVA, $p > 0.05$), and EPSC gamma power

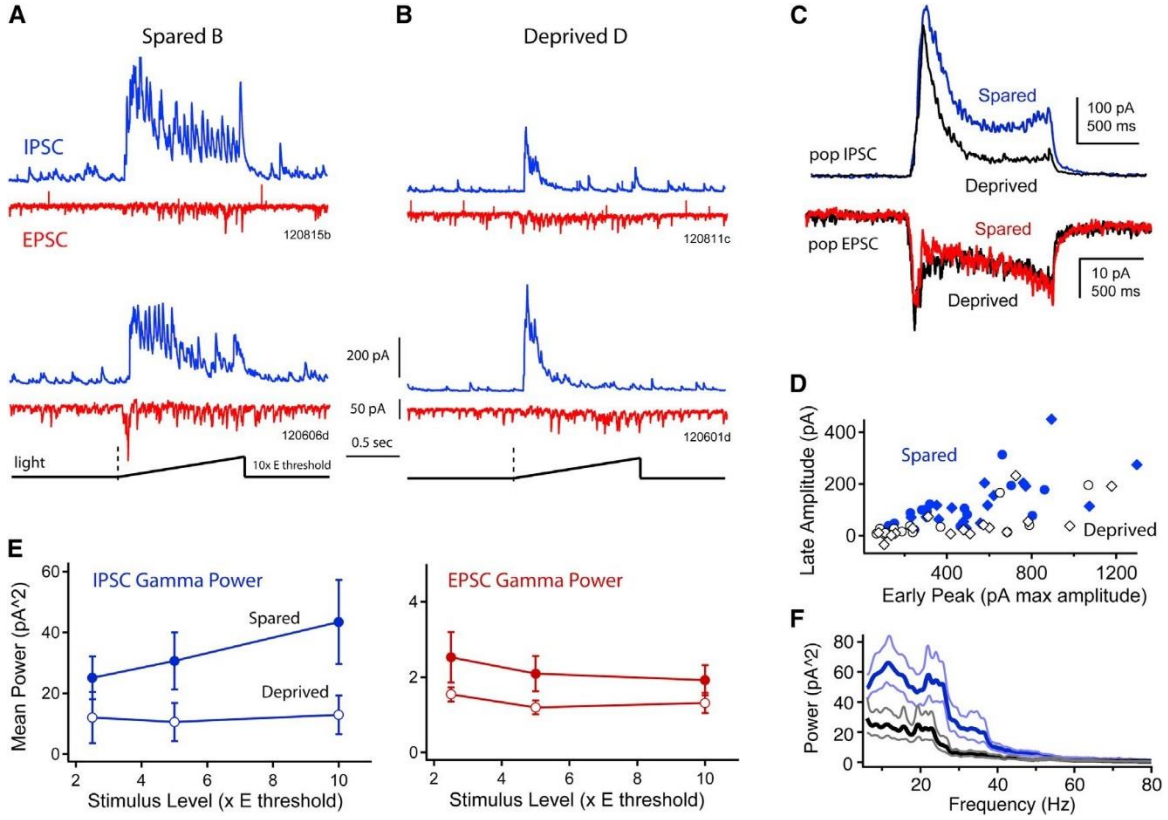

Figure 2.6. Effect of Deprivation on Intrinsic Gamma Oscillations Evoked by Ramp Photostimulation (A) Two example B column cells, showing EPSCs and IPSCs evoked by a light ramp to 10 x E_{thresh}. Each trace is a single sweep. (B) Two example D column cells, using the identical light ramp. (C) Population mean EPSC and IPSC in spared (B) versus deprived (D) columns, calculated for 10 x E_{thresh} stimuli. (D) Effect of deprivation on early IPSC amplitude versus late IPSC amplitude (0–0.3 and 0.3–1.2 s after ramp onset). Each symbol is one cell tested at 5 x E_{thresh} (circles) or 10 x E_{thresh} (diamonds). (E) Mean gamma power (20–60 Hz) for late component of IPSCs and EPSCs. Bars are SEM. (F) Mean power spectrum for late IPSCs in spared B columns (blue) versus deprived D columns (black), for 10 x E_{thresh} ramps.

showed a modest decrease (Figures 6C and 6E) ($p < 0.05$). Thus, deprivation powerfully reduced the ability of L2/3 local circuits to generate endogenous gamma oscillations.

Spontaneous Network Oscillations In Vivo

To test whether reduced oscillations also occurred in vivo, we measured spontaneous LFPs in spared and deprived S1 cortical columns in urethane anesthetized rats. Rats (n = 5) were deprived of D-row whiskers from P12, and recordings were made at P30–P37 after 14 days deprivation followed by 4–11 days of partial whisker regrowth. LFP recordings (500 ms duration) were made in L4 and L2/3 of D (deprived) and C or E

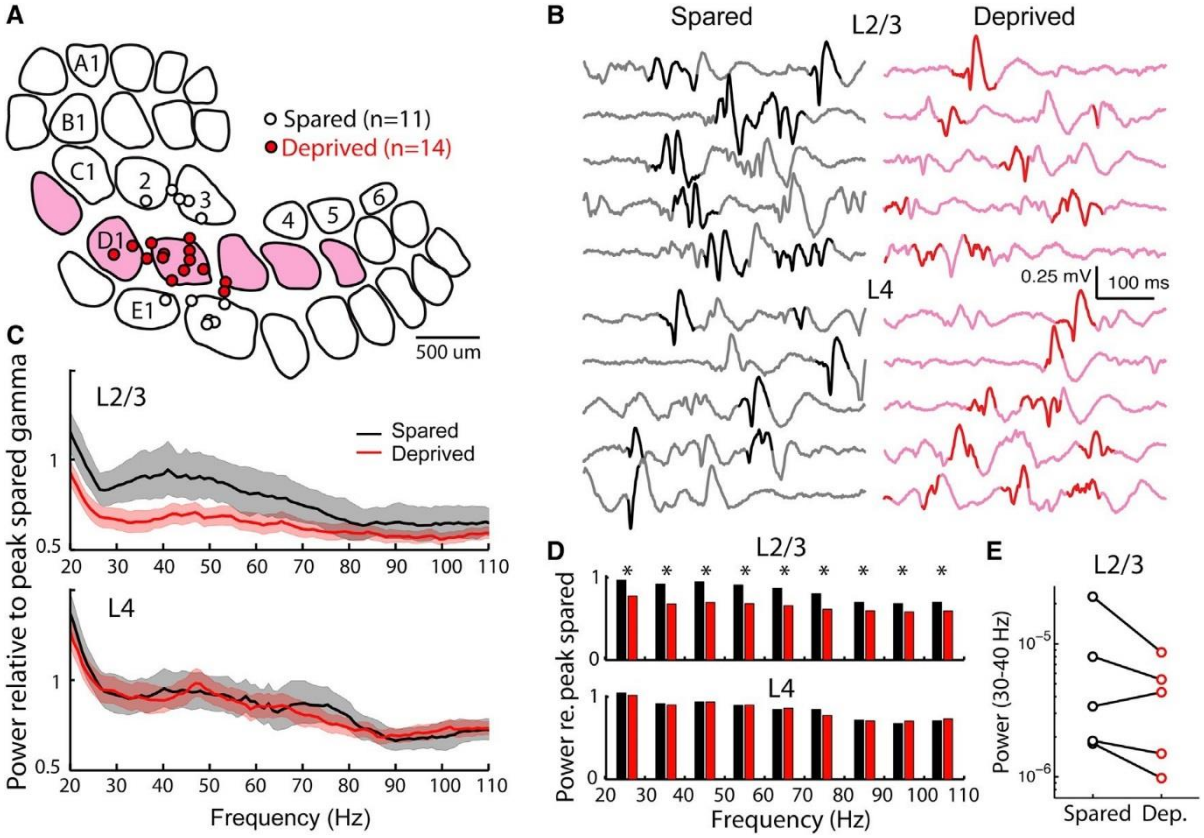

Figure 2.7. D-Row Deprivation Reduces Spontaneous Gamma Oscillations in L2/3 of Anesthetized S1 In Vivo. (A) Recording locations for deprived (D) and spared (C and E) penetrations, reconstructed from marking lesions and plotted on representative barrel outlines. Deprived columns are shaded. (B) Example raw LFP traces from a spared and a deprived column of one animal. Traces were chosen based on maximum similarity to mean LFP spectra for this animal. Bold indicates LFP segments with highest 40 Hz power (see the Experimental Procedures). (C) Mean normalized LFP spectra for spared and deprived columns across all animals. Shading: 99% confidence intervals. (D) Mean normalized LFP power in 10 Hz bins. Top: L2/3 recordings. Bottom: L4 recordings. *$p < 0.05$, random permutation test. (E) Mean LFP power in 30–40 Hz band for L2/3 recordings in each of the five rats separately. (E) Mean LFP power in 30–40 Hz band for L2/3 recordings in each of the five rats separately.

(spared) columns in each animal (Figures 7A and 7B). Spontaneous LFPs were dominated by low frequencies but included periods with enhanced gamma power (Figure 2.7B, bold epochs), as observed previously (Cardin et al., 2009). We compared LFP spectra between spared and deprived columns within each animal by normalizing all spectra to the average peak gamma power (30–50 Hz band) measured in spared columns for that animal. For L2/3, the resulting normalized spectra (averaged across animals) show that spectral power was reduced in deprived columns across a broad range of frequencies, with maximal decrease of 26% ± 12% in the 30–40 Hz range (n = 3,070 sweeps in 14 deprived columns, 2,617 sweeps in 11 spared columns, 5 rats). Power was significantly decreased in all gamma frequencies (20–80 Hz, tested in 10 Hz bands, a = 0.05, permutation test) (Figure 2.7D). This effect was consistent in 4/5 animals (Figure 2.7E). Reduced gamma power was observable in raw LFPs as reduced LFP amplitude during gamma- containing epochs (Figure 2.7B). In contrast, in L4 of the same penetrations, deprivation had no effect on average gamma power (3162 sweeps in deprived columns, 2,517 sweeps in spared columns, Figures 7C and 7D). Thus, deprivation decreases spontaneous (resting) gamma in L2/3 in vivo. We did not analyze whisker deflection-evoked gamma because any reduction is trivially attributed to the weakened L4 input to L2/3 (Allen et al., 2003; House et al., 2011).

2.4 Discussion

L2/3 is a major locus of whisker map plasticity in postneonatal rodents (Fox, 2002; Feldman, 2009), but prior studies of cellular plasticity mechanisms in L2/3 have focused on excitatory circuits almost exclusively. Whisker deprivation alters cross- columnar excitation (Finnerty et al., 1999; Marik et al., 2010), L4-L2/3 feedforward excitation (Allen et al., 2003; Shepherd et al., 2003; Clem and Barth, 2006; Bender et al., 2006; Hardingham et al., 2008; House et al., 2011), and local recurrent excitation in single columns (Cheetham et al., 2007, 2008; Bruno et al., 2009; Wen and Barth, 2011). These excitatory circuit changes are mostly consistent with reduced feedforward and local excitation within deprived columns, increased feedforward excitation into spared columns, and increased cross-columnar excitation from spared to deprived columns. These are appropriate to explain basic Hebbian features of map reorganization, including the reduction in responses to deprived whiskers and the strengthening and expansion of spared whisker representations.

In contrast, the role of L2/3 inhibitory circuits in plasticity is not understood. We hypothesized that deprivation preferentially weakens local recurrent inhibition in L2/3 relative to excitation. This disinhibition would constitute a homeostatic (compensatory) response to whisker deprivation (Turrigiano, 2012), which would be a significant modification of classical Hebbian models of L2/3 plasticity (e.g., Buonomano and Merzenich, 1998). Recently, in vivo measurements have detected deprivation- induced disinhibition in whisker-evoked sensory responses in L2/3 of S1 (Li and Feldman, 2010, Soc. Neurosci., abstract, 284.1; Gambino and Holtmaat, 2012). However, whether L2/3 recurrent circuits are a site of this disinhibition was not known.

We used ChR2 activation of L2/3 pyramidal cells to measure AMPA-mediated

excitation and GABA-A mediated inhibition in local L2/3 recurrent networks (Adesnik and Scanziani, 2010; Mateo et al., 2011). Whisker deprivation moderately reduced L2/3 recurrent excitation (by r-40%, for $EPSC_{1.1–1.4}$), consistent with the known reduction in PYR-PYR local connectivity (Cheetham et al., 2007). However, a much larger decrease (r-95%) was observed for recurrent inhibition, resulting in a substantial increase in excitation-inhibition ratio. These effects were observed in deprived D columns relative to spared B, C, and E columns, suggesting that disinhibition was column specific. Increased excitation-inhibition ratio was most pronounced at stimulus levels of 1.1–1.4x E_{thresh}, corresponding to initial network recruitment (Figure 2.5). This is likely to be the most physiologically relevant activity regime, because L2/3 neurons spike sparsely in vivo (Jadhav et al., 2009; O'Connor et al., 2010). Thus, L2/3 recurrent circuits are a major site of disinhibition following whisker deprivation and of homeostatic plasticity within deprived columns. We do not know how NMDA- or GABAB-receptor mediated currents were affected by deprivation.

Optogenetic stimulation provided several key advantages to examine changes in recurrent circuit function after experience-dependent plasticity. Optogenetic activation was critical to enable selective, single-column activation of the L2/3 recurrent network without contamination from fibers of passage, feedforward input, or direct stimulation of interneurons. Furthermore, graded stimulation by increasing light intensity allowed us to characterize the progressive recruitment of excitation and inhibition in the active recurrent network, which provides substantial additional information beyond unitary synaptic physiology using dual whole-cell recording. Light ramp stimulation confirmed that recurrent inhibition was reduced substantially more than excitation and showed that the ability of deprived L2/3 networks to generate gamma oscillations was profoundly reduced (Figure 2.6). This reduction was also observed in vivo, suggesting that L2/3 network changes are physiologically relevant (Figure 2.7). In contrast, prior studies of recurrent circuit plasticity were restricted to selected unitary connections or inferred recurrent network function from spontaneous activity, which is relatively nonselective and influenced by multiple circuit components (Cheetham et al., 2007; Maffei et al., 2004, 2006).

Reduced inhibition as a homeostatic mechanism during critical period plasticity

Deprivation is known to weaken or delay early development of inhibition in L4 (Chattopadhyaya et al., 2004; Maffei et al., 2004; Jiao et al., 2006; Chittajallu and Isaac, 2010), but its effects during the critical period for plasticity and in L2/3 have been unclear. Visual deprivation during the critical period potentiates recurrent inhibition in L4 of V1 (Maffei et al., 2006), but evidence for such potentiation in L2/3 or in S1 has been lacking. We performed deprivation during the P10–P14 critical period for maximal L2/3 plasticity in S1 (Stern et al., 2001) and found that L2/3 recurrent inhibition was strongly reduced. This is consistent with several structural measures of plasticity in L2/3 interneurons (Marik et al., 2010; Chen et al., 2011; Keck et al., 2011; van Versendaal et al., 2012) and provides a circuit locus for the disinhibition observed in vivo for whisker-evoked sensory responses in L2/3 of deprived (Li and Feldman, 2010, Soc. Neurosci.,

abstract, 284.1) and spared (Gambino and Holtmaat, 2012) columns. Thus, the current results show that L2/3 recurrent circuits are a major site of disinhibition for critical period plasticity. The preferential reduction in inhibition is unlike the L4-L2/3 feedforward projection, where deprivation drives a parallel (balanced) reduction in excitation and inhibition (House et al., 2011). Because local recurrent inhibition was not reduced in spared columns (Figure 2.5), disinhibition to surround whiskers in spared columns in vivo (Gambino and Holtmaat, 2012) must reflect either reduced cross-columnar drive onto local L2/3 interneurons or reduced efficacy of cross-columnar inhibitory axons (Helmstaedter et al., 2009). Deprivation also weakens L4-L2/3 feedforward inhibition in V1 and increases L2/3 network excitability, but whether local recurrent circuits are affected is not known (Maffei and Turrigiano, 2008).

Preferential reduction of L2/3 inhibition will increase network excitability and promote whisker-evoked spiking and therefore is a homeostatic response to deprivation that co-occurs with Hebbian weakening of excitatory input (Turrigiano, 2012). Reduced inhibition may also broaden sensory tuning, depending on which interneuron subtypes are affected (Atallah et al., 2012; Wilson et al., 2012). Deprivation-induced disinhibition in L2/3 of S1 also promotes LTP of spared whisker responses (Gambino and Holtmaat, 2012) and thus may be a permissive gate for subsequent steps in whisker map plasticity (Gandhi et al., 2008; Yazaki-Sugiyama et al., 2009; House et al., 2011). Consistent with this idea, disinhibition precedes associative learning and receptive field plasticity in L2/3 of auditory cortex (Froemke et al., 2007; Letzkus et al., 2011), and reduction of inhibition restores ocular dominance plasticity in adult V1 (Sale et al., 2010).

Sites and Mechanisms for Inhibitory Plasticity

Reduced recurrent excitation and inhibition may represent the functional outcome of known structural plasticity in L2/3 circuits. Deprivation reduces PYR-PYR unitary connection rate in deprived columns by reorganization of synaptic contacts and local axons (Cheetham et al., 2007, 2008; Bruno et al., 2009) without altering intrinsic excitability or unitary EPSP amplitude (Allen et al., 2003; Bender et al., 2006; Cheetham et al., 2007). This is likely to underlie the reduction in L2/3 recurrent excitation. In addition, deprivation drives rapid loss of inhibitory cell axons (in S1; Marik et al., 2010), dendritic and spine retraction by L2/3 interneurons, loss of inhibitory axonal boutons, and loss of inhibitory synapses on PYR dendrites (in V1; Chen et al., 2011; Keck et al., 2011; van Versendaal et al., 2012). These changes are likely to contribute to the loss of L2/3 recurrent inhibition observed here. Reduced inhibition may also reflect physiological weakening of excitatory synapses onto L2/3 interneurons (Lu et al., 2007). Many inhibitory cell types exist in L2/3 that could mediate the loss of recurrent inhibition (Gentet, 2012). One likely candidate is FS basket cells, which contribute strongly to disynaptic inhibition elicited by brief ChR2 stimulation in L2/3 pyramidal cells (Mateo et al., 2011) and generate perisomatic recurrent inhibition. Deprivation increases FS/PYR unitary IPSPs and does not alter FS intrinsic excitability (House et al., 2011), suggesting that reduced recurrent inhibition to the 2 ms pulse may reflect a reduction in the strength or number of PYR/FS synapses. This is also consistent with the loss of

gamma oscillations (see below). We speculate that recurrent inhibition evoked by ramp stimuli also involves somatostatin-positive Martinotti cells, which generate dendritic inhibition (Reyes et al., 1998; Kapfer et al., 2007). The reduction in ramp-evoked inhibition may reflect reduced activation or output of these cells, including structural loss of dendritic inhibitory synapses.

Plasticity of gamma oscillations

A major function of L2/3 FS inhibitory networks is to synchronize PYR cell spiking in the gamma frequency range (Cardin et al., 2009; Sohal et al., 2009). Gamma oscillations are a characteristic feature of cortical processing and have been proposed to promote synaptic integration, bind activity in cell assemblies, and regulate information transfer between neighboring neurons and distant cortical areas (Fries, 2009; Sohal et al., 2009; Wang, 2010). In rat S1, short bursts of tightly spatially localized gamma occur during exploration, though their behavioral relevance remains unclear (Sirota et al., 2008). Synaptic plasticity within PYR-FS circuits has been proposed to alter gamma oscillations (Paik and Glaser, 2010), but experimental evidence for plasticity of gamma (or other cortical rhythms) is lacking. We hypothesized that by reducing L2/3 inhibition, deprivation may reduce the capacity for gamma oscillations in deprived columns. Indeed, we observed a 70% reduction in ramp-evoked gamma power in L2/3 of S1 slices and a 25% reduction in spontaneous gamma power in L2/3 of deprived columns in S1 in vivo (Figures 6 and 7). Thus, the capacity for gamma oscillations is plastic and depends on sensory experience, likely reflecting local plasticity in FS recurrent circuits.

We speculate that this reduction in gamma power may impair sensory computation and reduce the ability of deprived whisker input to be relayed to higher cortical areas. If so, this would act to reduce the effective perceptual impact of deprived whiskers beyond the Hebbian reduction in whisker-evoked spike count alone. Thus, modulation of gamma could be an additional mechanism by which sensory experience regulates sensory processing or perception.

Conclusion

We used optogenetics to investigate the functional recruitment of L2/3 recurrent circuits during deprivation-induced whisker map plasticity. Deprivation modestly reduced recurrent excitation but powerfully reduced recurrent inhibition, suggesting that L2/3 recurrent circuits are a major site of homeostatic plasticity. At the same time, the capacity for gamma oscillations were powerfully reduced, which is likely to reduce the effective representation of deprived whiskers.

2.5 Experimental Procedures

Long-Evans rats (both sexes) were used. Procedures were approved by UC Berkeley Institutional Animal Care and Use Committee and meet the National Institutes of

Health's guidelines.

In Utero Electroporation

Timed-pregnant rats (18 days postcoitum) were anesthetized with isoflurane. The uterus was lifted from the abdominal cavity, and embryos were visualized and electroporated through the uterine wall. A glass pipette (30–40 mm tip diameter) was placed inside the left lateral cerebral ventricle, and r-1 ml of plasmid DNA solution was injected. The DNA solution contained: pCAG- ChR2(H134R)EYFP-WPRE plasmid (1 mg/ml), pCAG-DsRed plasmid (0.5 mg/ml), pCAG-GFP (0.5 mg/ml) plasmid, and 0.05% Fast Green. The capillary was removed, and electrode forceps (CUY650-5; NEPA GENE) were placed on either side of the head, outside the uterine wall. Five 50 V square pulses (50 ms duration, 950 ms interval) were delivered via an electroporator (BTX ECM830, Harvard Apparatus). The uterus was returned to the abdominal cavity, and the abdominal wall and skin were sutured. Buprenorphine was given for postoperative analgesia (0.05 mg/kg, twice at 8 hr interval). Pups were born by natural delivery. The purpose of the GFP plasmid was to increase overall fluorescence intensity to enable identification of expressing pups by transcranial imaging at postnatal day (P) 1. Only pups showing strong fluorescence in the EYFP/ GFP emission band in S1 on P1 were used in later experiments. The purpose of the DsRed plasmid was to enable fluorescently targeted patching of expressing cells during brain slice physiology (EYFP/GFP fluorescence was not imaged during physiology experiments, to avoid activating ChR2 with GFP excitation wavelengths). All DsRed cells expressed ChR2 (see the Re- sults), indicating that individual cells take up multiple plasmids.

Whisker Deprivation

Starting at postnatal day (P) 12, D-row whiskers D1–D6 and g were plucked from the right side of the face under transient isoflurane anesthesia (3.5% in O2). This is a standard manipulation to drive whisker map plasticity in L2/3 of S1 (Drew and Feldman, 2009). Plucking continued every other day (for 5–9 days) until recording.

Slice Preparation

Acute S1 slices were prepared at P17–P21 using standard techniques. Pups were anesthetized with isoflurane; the brain was isolated; and slices (0.4 mm) were cut in a semicoronal plane (Feldmeyer et al., 2002) that allows identification of A–E whisker columns (Finnerty et al., 1999; Allen et al., 2003). Slices were cut in low-sodium cutting solution (mM: NaCl 85, sucrose 75, D-(+)-glucose 25, NaHCO3 25, KCL 2.5, NaH2PO4 1.25, ascorbic acid 0.5, MgCl2 4, CaCl2 0.5, bubbled with 95:5 O2:CO2 [pH 7.2]) and collected into standard Ringer's solution (mM: 119 NaCl, 26.2 NaHCO3, 11 D-(+)-glucose, 1.3 MgSO4, 2.5 KCl, 1 NaH2PO4, and 2.5 CaCl2). Slices were incubated 30 min at 32oC and then stored 1–4 hr at room temperature (RT) before use. Column boundaries were identified with transillumination. In each slice, the spatial extent and level of expression were evaluated by visualizing DsRed fluorescence with low-power epifluorescence imaging using a Rolera XR camera (Q Imaging). (DsRed was used to avoid GFP excitation, which activates ChR2.) Only slices with strong, spatially uniform

DsRed expression over all five barrels of S1 (e.g., Figure 2.2A) were used in experiments. Whole-cell recordings were targeted to presumptive ChR2-expressing or ChR2-nonexpressing cells based on DsRed fluorescence using a 403 objective. In histological sections (n = 37 columns, ten rats), we determined that 94% ± 1% of DsRed+ L2/3 pyramidal cells also showed EYFP/GFP fluorescence, and 100% of DsRed+ cells showed direct ChR2 photocurrents, indicating that cells took up multiple plasmids (see below). This validates use of DsRed fluorescence to identify putative ChR2+ neurons.

Electrophysiology

Whole-cell recordings were made at 31oC using 2.5–4 MU pipettes and a Multiclamp 700B amplifier (Molecular Devices). Current clamp recordings to measure ChR2-evoked spiking were made using K gluconate internal (mM: 116 K gluconate, 20 HEPES, 6 KCl, 2 NaCl, 0.5 EGTA, 4 MgATP, 0.3 NaGTP, 5 Na2phosphocreatine; pH 7.2 and 295 mOsm). Recordings were made in Ringer's solution. Voltage clamp recordings to measure ChR2-evoked synaptic currents were made using Cs gluconate internal with QX-314 and BAPTA (mM: 108 D-gluconic acid, 108 CsOH, 20 HEPES, 5 tetraethylammonium-Cl, 2.8 NaCl, 0.4 EGTA, 4 MgATP, 0.3 NaGTP, 5 BAPTA, 5 QX-314 bromide; pH 7.2 and 290 mOsm). Pipette capacitance was neutralized, and whole-cell capacitance and series resistance were compensated (prediction and correction, 80%). The bath solution was Ringer's with D-APV (50 mM) and saclofen (100 mM). To measure the photo-LFP associated with direct ChR2 photocurrents, a 1.8–2.2 MU field potential pipette was used, and TTX citrate (50 mM), kynurenic acid (2 mM) and picrotoxin (100 mM) were added to the bath. All drugs were from Tocris. R_{input} and R_{series} were monitored in each sweep in response to a 5 mV test pulse. Recordings were targeted to pyramidal-shaped somata. Cells were excluded if Vm at break-in was >-60 mV, R_{series} >20 MU or R_{input} <100 MU. Vm values for voltage clamp recordings were corrected for the measured liquid junction potential (12 mV). Data acquisition and analysis used custom software in IGOR Pro (Wavemetrics) and Matlab.

ChR2 Activation

A 443 nm blue laser (40 mW, CrystaLaser DL445-040) was coupled via a multimodal fiber to the microscope epifluorescence arm and projected to the slice through a 43 air objective. Focusing optics and a pinhole set the beam diameter at the slice to 238 mm (2 3 SD of Gaussian profile) for synaptic physiology experiments or 312 mm for the spike threshold experiment. Both of these are smaller than the width of a single barrel column in rats (diameter 375– 500 mm; Wimmer et al., 2010). Laser intensity and timing were controlled by analog voltage commands generated in IGOR Pro. All laser intensity values represent intensity at the sample, calibrated using a light meter (Newport 1918-C). The lowest possible light intensities were always used to avoid phototoxicity.

Synaptic Responses

Synaptic responses were defined as light-evoked currents with latency >1 ms in nonfluorescent L2/3 pyramidal neurons (see below). Synaptic responses were

measured in D-APV (50 mM) and saclofen (100 mM) and thus primarily reflect AMPA and GABA-A currents. The light stimulus was centered in L2/3 of the home column for the recorded neuron. For each cell, we first determined the light intensity (using a 2 ms light pulse) required to elicit a reliable synaptic response, which was invariably an EPSC. This light intensity was defined as excitatory threshold (E_{thresh}).
For cells in the impulse experiment, we measured light-evoked currents at -68 mV (presumed EPSCs) and 0 mV (presumed IPSCs) at 1.0, 1.1, 1.2, 1.3, 1.4, 1.5, 1.6, 1.8, and 2.0 x E_{thresh} to define an input-output curve for synaptic currents (10–14 sweeps at each holding potential and stimulus intensity, 10 s interspike interval [isi]). Note that because driving force is equal for EPSCs and IPSCs, reporting current or conductance is equivalent. PSC magnitude was measured as charge (integrated current) in the first 50 ms of the response, relative to a 2 ms baseline prior to the light stimulus. Fractional excitation (E/(E + I)) was calculated from PSC charge. R_{series} compensation was checked and corrected several times during each recording, and cells were discarded if uncompensated R_{series} exceeded 20 MU. For cells in the ramp experiment, we measured currents at -68 and 0 mV in response to a linear ramp of light intensity (1.2 s duration) from 0 mW to 2.5, 5, or 10 x E_{thresh} (five sweeps at each holding potential at each stimulus intensity, 30 s isi). Oscillations were analyzed during the last 900 ms of the ramp stimulus, by calculating power spectra on individual sweeps, in both Igor and Matlab (Chronux toolbox). Gamma in slices was defined as power at 20–80 Hz, which is slightly lower than in vivo (Adesnik and Scanziani, 2010).

In Vivo LFP Recording

D-row whiskers were plucked from P12–P26 under transient isoflurane anesthesia. At P30–P37, rats were anesthetized with urethane (1.5 g/kg i.p., plus 10% maintenance doses as needed). A craniotomy was made over S1 (2.5 mm caudal, 5.2 mm lateral from bregma). LFPs were recorded using a tungsten electrode (5 ± 1 MU, FHC), amplified 1,000x, bandpass filtered (10–300 Hz), digitized at 44.1 kHz using custom routines in Igor Pro, and downsampled to 1 kHz offline. Data are from 500 ms spontaneous activity periods (no whisker stimulation) collected every 10 s. A small whisker deflection was applied after each spontaneous period but was not analyzed here. Recording depth was 491 ± 12 mm (n = 24) for L2/3 and 772.8 ± 7 mm for L4 (n = 24), as previously calibrated for Long-Evans rats at this age (Celikel et al., 2004). Penetrations were targeted to both deprived (D) and spared (C or E) columns in each animal, with randomized recording order. Approximately 240 sweeps were recorded in each layer per penetration (L2/3: 237 ± 4 sweeps, L4: 237 ± 9 sweeps). After all recordings were finished, electrolytic lesions were made in L4 (5 mA, 10 s, tip negative), and recording sites were reconstructed relative to barrel boundaries, as revealed by cytochrome oxidase staining in flattened tangential sections (Li et al., 2009). At least one deprived and one spared column was recorded in each animal, enabling within-animal comparison of deprived versus spared column LFPs. The in vivo gamma experiments used longer deprivation (14 days) than the slice experiments (5–9 days). Deprivation from 7–20 days duration drives similar weakening of whisker responses in L2/3 in vivo (Glazewski and Fox, 1996). While network function and plasticity

mechanisms can differ with age, gamma was reduced in both experiments, suggesting it is a conserved feature of plasticity across this age range.

In Vivo LFP Analysis

L2/3 and L4 spectra were analyzed separately. In 2/5 animals, slight 60 Hz recording noise was present, so LFP waveforms were notch filtered at 60 Hz (0.05 dB stopband attenuation, applied to all spared and all deprived recordings in those animals). LFPs were whitened using a second-order autoregression algorithm (Schneider and Neumaier, 2001; Minlebaev et al., 2011) whose coefficients were determined by fitting all LFPs as a group. Spectra were calculated from each whitened LFP segment using the Chronux toolbox in MATLAB (three tapers, 4 Hz bandwidth, 500 ms windows). To compare spectra between deprived and spared columns, all spectra from a single animal were divided by the peak power in the 30–50 Hz band of the average spared spectrum for that animal. These normalized spectra were then averaged across animals to determine the mean normalized spectra in spared and deprived columns. Confidence intervals (99%) were determined by jackknifing (Chronux). Statistical differences were tested for average power in 10 Hz bins using a random permutation test in which spared/deprived labels were randomized without replacement (5 3 105 permutations, a = 0.05, Bonferroni correction for multiple comparisons). Representative LFP segments (Figure 2.7B) were selected as those segments whose spectra showed the minimum least-squared error relative to the average spectrum. The highlighted 40 Hz epochs were identified by band-pass filtering the raw LFP (40 ± 7.5 Hz, Butterworth) and highlighting segments with band-passed amplitude >1 SD above the mean for that layer and condition (spared or deprived).

Histology

Rats were deeply anesthetized with isoflurane and perfused transcardially with 4% paraformaldehyde in 0.1 M phosphate buffer (PB), and the brain was removed. Brains were postfixed for 2 hr, cryoprotected in 30% sucrose in 0.1 M PB, and sectioned (50 um) coronally on a freezing microtome. To determine the fraction of electroporated cells, sections were costained for the pan-neuronal marker Neu-N by incubating free-floating sections for 40–48 hr at 4oC with mouse anti-NeuN antibody (1:400, Millipore, MAB377) in phosphate- buffered saline (PBS) containing 0.5% Triton X-100 and 5% normal goat serum. Sections were rinsed with PBS and incubated for 90 min at room temperature in Alexa-594 conjugated goat anti-mouse secondary (1:200, Invitrogen). Sections were rinsed three times in PB and mounted in Vectashield. Images were obtained by confocal microscopy (Zeiss LSM 710 Axio Observer).

Statistics

Reported values are mean ± SEM, unless otherwise noted. Medians and 95% confidence intervals were generated by bootstrapping (1,000 resamplings) from the original distributions.

2.6 Acknowledgements

This chapter, in full, is a republication of the material as it appears in Shao,Y.R., Isett, B.R., Miyashita, T., Chung, J., Pourzia, O., Gasperini, R.J., and Feldman, D.E. 2013. Plasticity of recurrent L2/3 inhibition and gamma oscillations by whisker experience. *Neuron*, 80, 210-222. The dissertation author was the second author of this paper. RS performed slice experiments, data analysis, and contributed to writing the paper. BI performed in vivo experiments, data analysis, and contributed to writing the paper. TM and JC characterized optogenetic methods. OP and RG performed slice experiments. DF supervised the study and co-wrote the paper. We thank Prof. K. Deisseroth Stanford University) for the ChR2-H134R-EYFPWPRE construct. This work was supported by grants from the National Institutes of Health (1R01 NS073912) and the National Science Foundation (NSF) (# SMA 1041755) to the Temporal Dynamics of Learning Center, an NSF Science of Learning Center. B.R.I. was supported by National Science Foundation predoctoral fellowship (DGE 1106400).

2.7 References

Adesnik, H., and Scanziani, M. (2010). Lateral competition for cortical space by layer-specific horizontal circuits. Nature 464, 1155–1160.

Allen, C.B., Celikel, T., and Feldman, D.E. (2003). Long-term depression induced by sensory deprivation during cortical map plasticity in vivo. Nat. Neurosci. 6, 291–299.

Antonini, A., and Stryker, M.P. (1993). Rapid remodeling of axonal arbors in the visual cortex. Science 260, 1819–1821.

Atallah, B.V., Bruns, W., Carandini, M., and Scanziani, M. (2012). Parvalbumin-expressing interneurons linearly transform cortical responses to visual stimuli. Neuron 73, 159–170.

Bender, K.J., Allen, C.B., Bender, V.A., and Feldman, D.E. (2006). Synaptic basis for whisker deprivation-induced synaptic depression in rat somatosensory cortex. J. Neurosci. 26, 4155–4165.

Broser, P., Grinevich, V., Osten, P., Sakmann, B., and Wallace, D.J. (2008). Critical period plasticity of axonal arbors of layer 2/3 pyramidal neurons in rat somatosensory cortex: layer-specific reduction of projections into deprived cortical columns. Cereb. Cortex 18, 1588–1603.

Bruno, R.M., Hahn, T.T., Wallace, D.J., de Kock, C.P., and Sakmann, B. (2009). Sensory experience alters specific branches of individual corticocortical axons during development. J. Neurosci. 29, 3172–3181.

Buonomano, D.V., and Merzenich, M.M. (1998). Cortical plasticity: from synapses to maps. Annu. Rev. Neurosci. 21, 149–186.

Buzsaki, G., and Wang, X.-J. (2012). Mechanisms of gamma oscillations. Annu. Rev. Neurosci. 35, 203–225.

Cardin, J.A., Carlen, M., Meletis, K., Knoblich, U., Zhang, F., Deisseroth, K., Tsai, L.H., and Moore, C.I. (2009). Driving fast-spiking cells induces gamma rhythm and controls sensory responses. Nature 459, 663–667.

Celikel, T., Szostak, V.A., and Feldman, D.E. (2004). Modulation of spike timing by sensory deprivation during induction of cortical map plasticity. Nat. Neurosci. 7, 534–541.

Chattopadhyaya, B., Di Cristo, G., Higashiyama, H., Knott, G.W., Kuhlman, S.J., Welker, E., and Huang, Z.J. (2004). Experience and activity-dependent maturation of

perisomatic GABAergic innervation in primary visual cortex during a postnatal critical period. J. Neurosci. 24, 9598–9611.

Cheetham, C.E., Hammond, M.S., Edwards, C.E., and Finnerty, G.T. (2007). Sensory experience alters cortical connectivity and synaptic function site specifically. J. Neurosci. 27, 3456–3465.

Cheetham, C.E., Hammond, M.S., McFarlane, R., and Finnerty, G.T. (2008). Altered sensory experience induces targeted rewiring of local excitatory connections in mature neocortex. J. Neurosci. 28, 9249–9260.

Chittajallu, R., and Isaac, J.T. (2010). Emergence of cortical inhibition by coordinated sensory-driven plasticity at distinct synaptic loci. Nat. Neurosci. 13, 1240–1248.

Chen, J.L., Lin, W.C., Cha, J.W., So, P.T., Kubota, Y., and Nedivi, E. (2011). Structural basis for the role of inhibition in facilitating adult brain plasticity. Nat. Neurosci. 14, 587–594.

Clem, R.L., and Barth, A. (2006). Pathway-specific trafficking of native AMPARs by in vivo experience. Neuron 49, 663–670.

Cruikshank, S.J., Urabe, H., Nurmikko, A.V., and Connors, B.W. (2010). Pathway-specific feedforward circuits between thalamus and neocortex revealed by selective optical stimulation of axons. Neuron 65, 230–245.

Drew, P.J., and Feldman, D.E. (2009). Intrinsic signal imaging of deprivation- induced contraction of whisker representations in rat somatosensory cortex. Cereb. Cortex 19, 331–348.

Feldman, D.E., and Brecht, M. (2005). Map plasticity in somatosensory cortex. Science 310, 810–815.

Feldman, D.E. (2009). Synaptic mechanisms for plasticity in neocortex. Annu. Rev. Neurosci 32, 33–55.

Feldmeyer, D., Lubke, J., Silver, R.A., and Sakmann, B. (2002). Synaptic connections between layer 4 spiny neurone-layer 2/3 pyramidal cell pairs in juvenile rat barrel cortex: physiology and anatomy of interlaminar signalling within a cortical column. J. Physiol. 538, 803–822.

Feldmeyer, D., Lubke, J., and Sakmann, B. (2006). Efficacy and connectivity of intracolumnar pairs of layer 2/3 pyramidal cells in the barrel cortex of juvenile rats. J. Physiol. 575, 583–602.

Finnerty, G.T., Roberts, L.S., and Connors, B.W. (1999). Sensory experience modifies the short-term dynamics of neocortical synapses. Nature 400, 367–371.
Fox, K. (2002). Anatomical pathways and molecular mechanisms for plasticity in the barrel cortex. Neuroscience 111, 799–814.

Fries, P. (2009). Neuronal gamma-band synchronization as a fundamental process in cortical computation. Annu. Rev. Neurosci. 32, 209–224.

Froemke, R.C., Merzenich, M.M., and Schreiner, C.E. (2007). A synaptic memory trace for cortical receptive field plasticity. Nature 450, 425–429.

Gambino, F., and Holtmaat, A. (2012). Spike-timing-dependent potentiation of sensory surround in the somatosensory cortex is facilitated by deprivation- mediated disinhibition. Neuron 75, 490–502.

Gandhi, S.P., Yanagawa, Y., and Stryker, M.P. (2008). Delayed plasticity of inhibitory neurons in developing visual cortex. Proc. Natl. Acad. Sci. USA 105, 16797–16802.

Gentet, L.J. (2012). Functional diversity of supragranular GABAergic neurons in the barrel cortex. Front. Neural Circuits 6, 52.

Glazewski, S., and Fox, K. (1996). Time course of experience-dependent synaptic potentiation and depression in barrel cortex of adolescent rats.
J. Neurophysiol. 75, 1714–1729.

Hardingham, N., Wright, N., Dachtler, J., and Fox, K. (2008). Sensory deprivation unmasks a PKA-dependent synaptic plasticity mechanism that operates in parallel with CaMKII. Neuron 60, 861–874.

Helmstaedter, M., Sakmann, B., and Feldmeyer, D. (2009). Neuronal correlates of local, lateral, and translaminar inhibition with reference to cortical columns. Cereb. Cortex 19, 926–937.

House, D.R., Elstrott, J., Koh, E., Chung, J., and Feldman, D.E. (2011). Parallel regulation of feedforward inhibition and excitation during whisker map plasticity. Neuron 72, 819–831.

Jacob, V., Petreanu, L., Wright, N., Svoboda, K., and Fox, K. (2012). Regular spiking and intrinsic bursting pyramidal cells show orthogonal forms of experience-dependent plasticity in layer V of barrel cortex. Neuron 73, 391–404.

Jadhav, S.P., Wolfe, J., and Feldman, D.E. (2009). Sparse temporal coding of elementary tactile features during active whisker sensation. Nat. Neurosci. 12, 792–800.

Jiao, Y., Zhang, C., Yanagawa, Y., and Sun, Q.Q. (2006). Major effects of sensory experiences on the neocortical inhibitory circuits. J. Neurosci. 26, 8691–8701.

Kapfer, C., Glickfeld, L.L., Atallah, B.V., and Scanziani, M. (2007). Supralinear increase of recurrent inhibition during sparse activity in the somatosensory cortex. Nat. Neurosci. 10, 743–753.

Keck, T., Scheuss, V., Jacobsen, R.I., Wierenga, C.J., Eysel, U.T., Bonhoeffer, T., and Hubener, M. (2011). Loss of sensory input causes rapid structural changes of inhibitory neurons in adult mouse visual cortex. Neuron 71, 869–882.

Lefort, S., Tomm, C., Floyd Sarria, J.C., and Petersen, C.C. (2009). The excitatory neuronal network of the C2 barrel column in mouse primary somatosensory cortex. Neuron 61, 301–316.

Letzkus, J.J., Wolff, S.B., Meyer, E.M., Tovote, P., Courtin, J., Herry, C., and Lu¨ thi, A. (2011). A disinhibitory microcircuit for associative fear learning in the auditory cortex. Nature 480, 331–335.

Li, L., Bender, K.J., Drew, P.J., Jadhav, S.P., Sylwestrak, E., and Feldman, D.E. (2009). Endocannabinoid signaling is required for development and critical period plasticity of the whisker map in somatosensory cortex. Neuron 64, 537–549.

Lu, J.T., Li, C.Y., Zhao, J.P., Poo, M.M., and Zhang, X.H. (2007). Spike-timing-dependent plasticity of neocortical excitatory synapses on inhibitory interneurons depends on target cell type. J. Neurosci. 27, 9711–9720.

Maffei, A., and Turrigiano, G.G. (2008). Multiple modes of network homeostasis in visual cortical layer 2/3. J. Neurosci. 28, 4377–4384.

Maffei, A., Nelson, S.B., and Turrigiano, G.G. (2004). Selective reconfiguration of layer 4 visual cortical circuitry by visual deprivation. Nat. Neurosci. 7, 1353– 1359.

Maffei, A., Nataraj, K., Nelson, S.B., and Turrigiano, G.G. (2006). Potentiation of cortical inhibition by visual deprivation. Nature 443, 81–84.

Mateo, C., Avermann, M., Gentet, L.J., Zhang, F., Deisseroth, K., and Petersen, C.C. (2011). In vivo optogenetic stimulation of neocortical excitatory neurons drives brain-state-dependent inhibition. Curr. Biol. 21, 1593–1602.

Marik, S.A., Yamahachi, H., McManus, J.N., Szabo, G., and Gilbert, C.D. (2010). Axonal dynamics of excitatory and inhibitory neurons in somatosensory cortex. PLoS Biol. 8, e1000395.

Minlebaev, M., Colonnese, M., Tsintsadze, T., Sirota, A., and Khazipov, R. (2011). Early g oscillations synchronize developing thalamus and cortex. Science 334, 226–229.

Miyashita, T., Wintzer, M., Kurotani, T., Konishi, T., Ichinohe, N., and Rockland, K.S. (2010). Neurotrophin-3 is involved in the formation of apical dendritic bundles in cortical layer 2 of the rat. Cereb. Cortex 20, 229–240.

Nagel, G., Brauner, M., Liewald, J.F., Adeishvili, N., Bamberg, E., and Gottschalk, A. (2005). Light activation of channelrhodopsin-2 in excitable cells of Caenorhabditis elegans triggers rapid behavioral responses. Curr. Biol. 15, 2279–2284.

O'Connor, D.H., Peron, S.P., Huber, D., and Svoboda, K. (2010). Neural activity in barrel cortex underlying vibrissa-based object localization in mice. Neuron 67, 1048–1061.

Paik, S.B., and Glaser, D.A. (2010). Synaptic plasticity controls sensory responses through frequency-dependent gamma oscillation resonance. PLoS Comput. Biol. 6, e1000927.

Petreanu, L., Huber, D., Sobczyk, A., and Svoboda, K. (2007). Channelrhodopsin-2-assisted circuit mapping of long-range callosal projections. Nat. Neurosci. 10, 663–668.

Reyes, A., Lujan, R., Rozov, A., Burnashev, N., Somogyi, P., and Sakmann, B. (1998). Target-cell-specific facilitation and depression in neocortical circuits. Nat. Neurosci. 1, 279–285.

Sale, A., Berardi, N., Spolidoro, M., Baroncelli, L., and Maffei, L. (2010). GABAergic inhibition in visual cortical plasticity. Front. Cell Neurosci. 4, 10.

Saito, T., and Nakatsuji, N. (2001). Efficient gene transfer into the embryonic mouse brain using in vivo electroporation. Dev. Biol. 240, 237–246.

Schneider, T., and Neumaier, A. (2001). Algorithm 808: ARfit - a Matlab package for the estimation of parameters and eigenmodes of multivariate autoregressive models. ACM Trans. Math. Softw. 27, 58–65.

Schummers, J., Marin˜ o, J., and Sur, M. (2002). Synaptic integration by V1 neurons depends on location within the orientation map. Neuron 36, 969–978.

Shepherd, G.M., Pologruto, T.A., and Svoboda, K. (2003). Circuit analysis of experience-dependent plasticity in the developing rat barrel cortex. Neuron 38, 277–289.

Simons, D.J. (1978). Response properties of vibrissa units in rat SI somatosensory neocortex. J. Neurophysiol. 41, 798–820.

Sirota, A., Montgomery, S., Fujisawa, S., Isomura, Y., Zugaro, M., and Buzsáki, G. (2008). Entrainment of neocortical neurons and gamma oscillations by the hippocampal theta rhythm. Neuron 60, 683–697.

Sohal, V.S., Zhang, F., Yizhar, O., and Deisseroth, K. (2009). Parvalbumin neurons and gamma rhythms enhance cortical circuit performance. Nature 459, 698–702.

Stern, E.A., Maravall, M., and Svoboda, K. (2001). Rapid development and plasticity of layer 2/3 maps in rat barrel cortex in vivo. Neuron 31, 305–315.

Tabata, H., and Nakajima, K. (2001). Efficient in utero gene transfer system to the developing mouse brain using electroporation: visualization of neuronal migration in the developing cortex. Neuroscience 103, 865–872.

Trachtenberg, J.T., and Stryker, M.P. (2001). Rapid anatomical plasticity of horizontal connections in the developing visual cortex. J. Neurosci. 21, 3476–3482.

Turrigiano, G. (2012). Homeostatic synaptic plasticity: local and global mechanisms for stabilizing neuronal function. Cold Spring Harb. Perspect. Biol. 4, a005736.

van Versendaal, D., Rajendran, R., Saiepour, M.H., Klooster, J., Smit-Rigter, L., Sommeijer, J.P., De Zeeuw, C.I., Hofer, S.B., Heimel, J.A., and Levelt, C.N. (2012). Elimination of inhibitory synapses is a major component of adult ocular dominance plasticity. Neuron 74, 374–383.

Wang, X.J. (2010). Neurophysiological and computational principles of cortical rhythms in cognition. Physiol. Rev. 90, 1195–1268.

Wen, J.A., and Barth, A.L. (2011). Input-specific critical periods for experience-dependent plasticity in layer 2/3 pyramidal neurons. J. Neurosci. 31, 4456– 4465.
Wilson, N.R., Runyan, C.A., Wang, F.L., and Sur, M. (2012). Division and subtraction by distinct cortical inhibitory networks in vivo. Nature 488, 343–348.

Wimmer, V.C., Bruno, R.M., de Kock, C.P., Kuner, T., and Sakmann, B. (2010). Dimensions of a projection column and architecture of VPM and POm axons in rat vibrissal cortex. Cereb. Cortex 20, 2265–2276.

Yamahachi, H., Marik, S.A., McManus, J.N., Denk, W., and Gilbert, C.D. (2009). Rapid axonal sprouting and pruning accompany functional reorganization in primary visual cortex. Neuron 64, 719–729.

Yazaki-Sugiyama, Y., Kang, S., Cateau, H., Fukai, T., and Hensch, T.K. (2009). Bidirectional plasticity in fast-spiking GABA circuits by visual experience. Nature 462, 218–221.

Chapter 3

Simultaneous Codes for Microscopic and Macroscopic Tactile Features in Mouse Somatosensory Cortex

Isett, Brian R. & Feldman, Daniel E.

3.1 Summary

The whisker system is thought to encode texture by aggregating vibrissal micromotions over successive whisks, which in turn drive temporally precise spikes in S1. However, it is unknown whether these micromotions also encode spatial features. We trained head-fixed mice to discriminate smooth surfaces from a set of rough surfaces including raised gratings and sandpaper while running on a 1D virtual track. Whisker imaging revealed stick-slip micromotions locked to ridges, which in turn evoked spatially and temporally precise spikes in S1. S1 contained overlapping touch-, texture- and slip-responsive neurons. Mean firing rate was higher on rough surfaces due to increased slip-evoked spikes, but individually weighted neural responses were necessary to accurately decoded rough vs. smooth trials. At the same time, 20% of neurons showed selectivity among rough textures, including tuning for specific spatial periods. Thus, neurons with spatial and temporal selectivity simultaneously coded microscope (slips, ridges) and macroscopic (touch, roughness) tactile features.

3.2 Introduction

The rodent whisker system is exquisitely sensitive to touch (Carvell and Simons, 1990), and can be used to extract precise information about object location and texture (Jadhav and Feldman, 2010; Kleinfeld and Deschênes, 2011; Morita et al., 2011). However, much less is known about how the whisker system encodes spatial properties like shape. As mice rhythmically sweep their whiskers in rostro-caudal space, they acquire tactile information through a series of contacts, bends, and whisker vibrations (Arabzadeh et al., 2003; Gerdjikov et al., 2010; O'Connor et al., 2010; Zuo et al., 2011). Successful readout of local spatial features requires a temporal whisker position signal, as well as a precise tactile input signal capturing spatial variation in the environment (Ahissar and Arieli, 2001; Diamond et al., 2008). Whisker position signals have been observed in primary somatosensory cortex (S1), primary motor cortex (M1) as well as cerebellum (Chen et al., 2016; Curtis and Kleinfeld, 2009; Kleinfeld and Deschênes, 2011). Whether whisker kinematics encode local surface variation with sufficient precision to represent discrete spatial features is unknown (Garion et al., 2014; von Heimendahl et al., 2007; Schwarz, 2016).

The transition from fine textures to sufficiently coarse textures marks an important boundary between temporal and spatial tactile coding (Katz, 1989; Weber et al., 2013). It is thought that stick-slip motions ("kinetic signatures"), triggered by frictional interactions between the whisker tip and surface microgeometry represent a fundamental unit of tactile information (Arabzadeh et al., 2005; Hires et al., 2013; Jadhav et al., 2009; Ritt et al., 2008; Schwarz, 2016; Waiblinger et al., 2015; Wolfe et al., 2008). Slips increase in amplitude and rate with increased texture roughness (Wolfe et al., 2008), and neurons in primary whisker somatosensory cortex (S1) respond by increasing firing rate with sparse, temporally precise spikes (Jadhav et al., 2009). Within the slip hypothesis (Schwarz, 2016), roughness is coded by an increase in slip-evoked spikes, which increases S1 firing rate and synchrony (Jadhav and Feldman, 2010). Despite this, no studies have shown whether slips, nor the spikes caused by slips, accurately predict rough and smooth surfaces at the resolution of single trials.

To examine these questions, we trained head-fixed mice to discriminate smooth from rough surfaces while running past stimuli on a virtual track. Rough stimuli consisted of raised gratings with 2, 4, 8 and 10mm spatial period, as well as coarse sandpaper (P150). By simultaneously measuring whisker position and neural responses across cortical layers in S1 columns, we found that slips increased on rough surfaces and provided sufficient information to decode single rough vs. smooth trials. In addition, we found that slips accumulated along ridges, local spatial features of raised gratings, recapitulating grating spatial period. Neurons in S1 responded to touch, roughness, and local features such as slips and ridges. Like slips, spikes accumulated in space along ridges, providing a potential mechanism for encoding spatial period. Indeed, neurons in

layer 5 (L5) showed diverse spatial selectivity, with many selective units showing tuning for specific spatial frequencies. Thus, unlike V1 where hierarchical receptive fields are narrowly tuned for precise stimulus features, S1 neurons may participate in a multiplexed coding scheme that simultaneously represents microscopic and macroscopic touch features.

3.3 Results

Mice discriminate Smooth vs. Rough surfaces on a virtual track

We trained head-fixed mice to run on a freely rotating disk and discriminate smooth from rough surface patches presented on a rotating cylinder (Figure 3.3.1). Surface patches were 3cm long and consisted of smooth cylinder, raised ridge gratings (0.8 mm ridge height, 2, 4, 8 or 10 mm spatial period), or rough P150 sandpaper (raised 0.8 mm above the cylinder). Mice ran and actively whisked against the cylinder, which rotated in proportion to the mouse's running velocity, creating a 1D virtual track (see: Experimental Procedures). Mice were trained in a Go/No-go task design to lick for water reward when they felt a ridge or sandpaper stimulus (collectively termed "Rough" stimuli), and to withhold licking for a Smooth stimulus. Training was performed in the dark. Thus, mice performed a virtual tactile foraging task in which they were rewarded for finding rough patches along an otherwise smooth surface.

On each contact trial, a smooth surface was translated medially to contact the whiskers (Figure 3.3.1B, static introduction). This smooth surface preceded the randomly chosen stimulus patch for that trial. The mouse then self-initiated a trial by running forward, causing the stimulus to rotate proportional to run velocity (Figure 3.31B, closed loop). The mouse ran 4-5 cm to bring the stimulus patch into whisker contact (1-2cm caudal stimulus rotation). At this point, a 1-2s response window opened and mice licked or withheld licking to indicate choice (Figure 3.3.1B). An example trial is shown in Figure 3.3.1C. On Rough trials, licking in the response window triggered a 3µl water reward (Hit). On Smooth trials, licking triggered a 5s time out (False Alarm). No action was taken on Correct Rejection (CR) and Miss trials. If mice ran to the end of the stimulus patch, wheel rotation stopped. When the response window elapsed, the cylinder was retracted (inter-trial epoch). The ratio of Rough:Smooth trials was 50:50, and 7% of trials were catch trials in which the wheel was only translated part way to the whiskers, so that the mouse initiated trials while whisking in air.

During each trial, we imaged whisker motion in the rostro-caudal plane using a custom CCD imaging system (4 kHz sampling rate, 3s imaging per trial, see: Experimental Procedures). From this we calculated the spatial point of contact of each whisker on the surface at each time point in the trial. Because the spatial position of each ridge is known, we calculated the time and spatial position of first whisker contact with the leading edge of Rough stimuli (i.e., the onset of the first ridge or the P150 sandpaper), and the corresponding position for the Smooth stimulus (Figure 1C, asterisk; mean ± CI_{95} position error for C1 = 0.15 ± 0.16 mm, C2 = 0.41 ± 0.16mm;

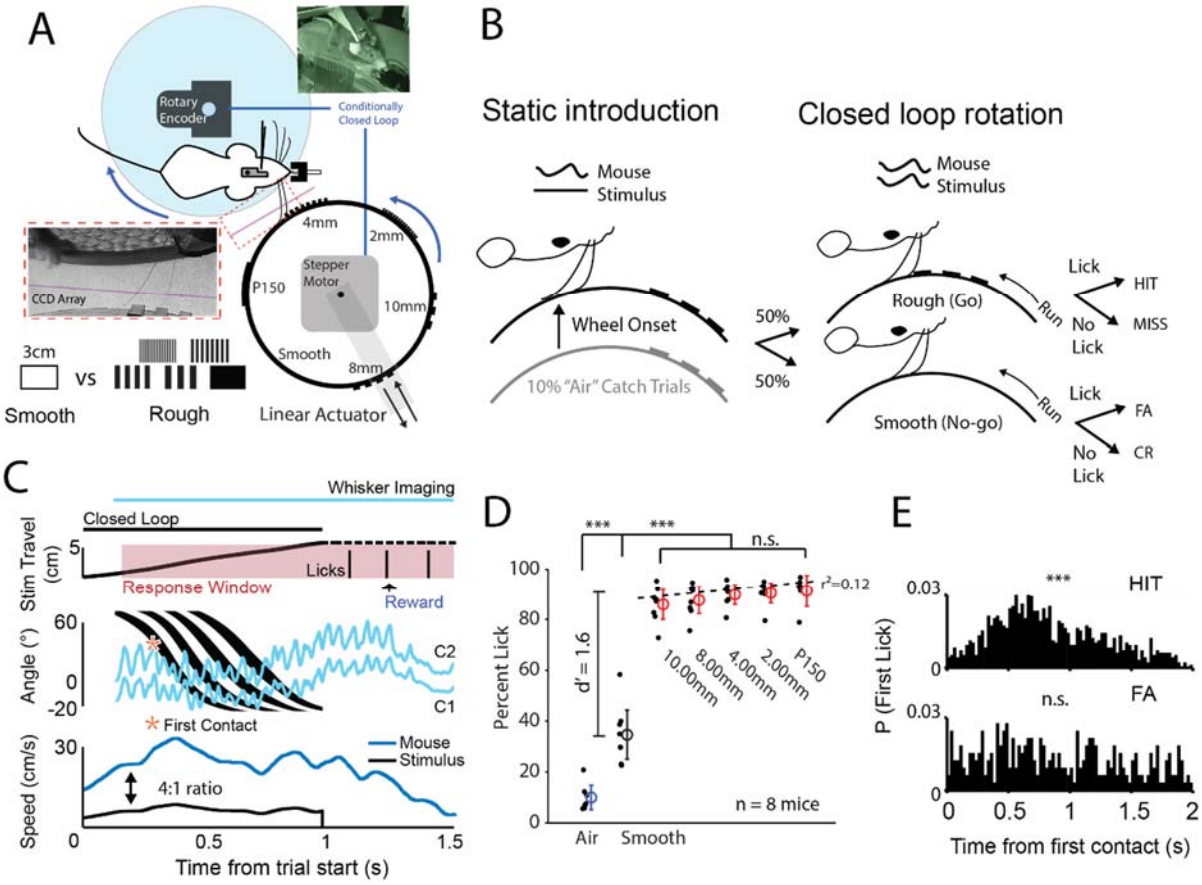

Figure 3.1. **Mice discriminate smooth and rough surfaces in a virtual tactile foraging task.** (A) Head-fixed mice ran on a disk while a stepper motor rotated smooth (No-go) or rough (Go) stimuli through the whisker field. Rough stimuli consisted of 4 gratings with 2 to 10mm spatial period, and one P150 sandpaper. Smooth stimuli consisted of acetate plastic. (B) The stimulus cylinder translated medially to the whisker field in a static, neutral position. Trials began when stimulus rotation became closed-loop with rodent velocity. Licking responses were scored into Hit, Miss, False Alarms (FA) and Correct Rejections (CR). In 10% of trials the stimulus cylinder never returned completely to whisker field ("Air" catch trials). (C) Top: An example Go trial shown from trial start to mouse reward. Middle: Whiskers were imaged at 4 kHz for 1-2s during stimulus exploration and the first moment of stimulus patch contact was calculated post hoc from whisker tracking ("First Contact"). Bottom: Mouse and stimulus velocity. (D Percent licks to rough (red) and smooth trials (black) compared to catch trials in air (blue; n=8 mice, ANOVA and post-hoc paired t-test, controlled for multiple comparisons). (E) Probability of first lick occurring in 25ms bins relative to first contact on Hit and False Alarm (FA) trials (*** $p<0.001$, n.s. $p> 0.05$; χ^2 test of uniformity, d.f.=79).

Figure 3.3.S1A). There was substantial trial-to-trial variability in mouse locomotion and active whisking, which led to heterogeneous whisker exploration patterns across trials as the mice acquired tactile information.

Training was performed in stages initially using blocks of fixed velocity stimuli (open loop), then random fixed velocity stimuli, and finally random closed-loop stimuli. Criterion performance (>75% correct for 2 consecutive days) was achieved in 21 ± 10 training sessions (mean $\pm CI_{95}$, n=8 mice), with all whiskers intact (Figure 3.S2A), at

which point the right whiskers were trimmed to leave only C1 and C2 whiskers intact. Final discrimination was above chance (77 ± 3.5% correct, n= 8 mice), with more licks to Rough trials than Smooth trials ($p<0.001$, one-way ANOVA with post hoc t-test; Figure 3.1D). This corresponded to a mean d' of 1.6 ± 0.09 per day above criterion (n=291 days in 8 mice). There was no difference in response rate for individual Rough stimuli ($p=0.400$, one-way ANOVA, n=8 mice), however response rate was weakly correlated with spatial frequency ($r^2=0.12$, $p<0.05$ linear regression t-test; Figure 3.1D). For Hit trials, licks occurred 781 ± 29 ms after first contact (mean ± CI_{95}, n = 1215 imaged hit trials), while on false alarm trials, licks were uniformly distributed across the trial ($p=0.19$, $\chi^2 = 89.63$, d.f. =79, test for uniformity; Figure 3.1E). Mean running speed did not differ between Rough and Smooth trials ($p=0.21$, paired t-test, n = 7 mice; Rough =16.1 ±3 cm/s, Smooth = 17.14 ± 4 cm/s; Figure 3.S2B-C).

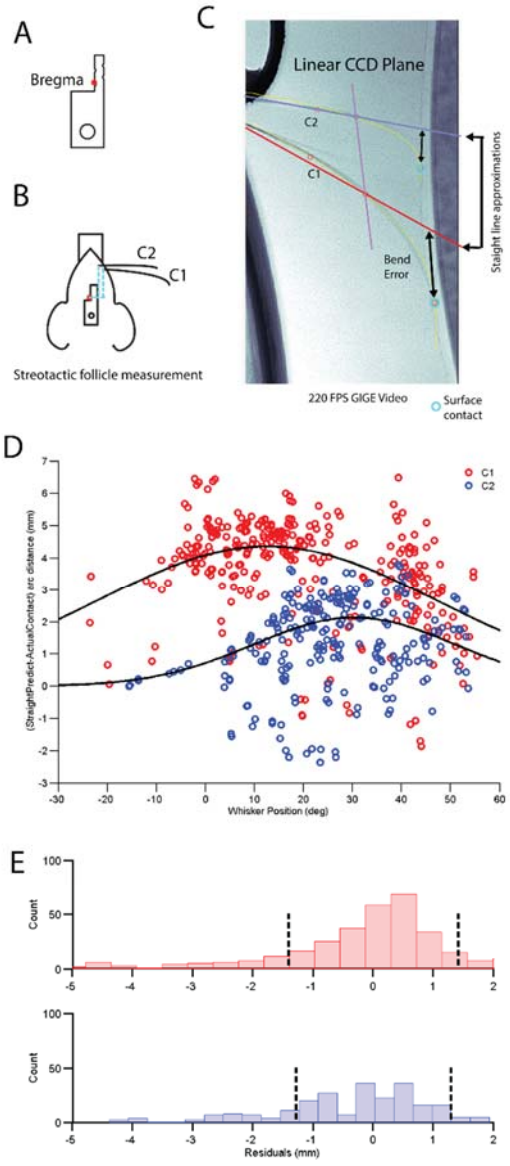

Supplemental Figure 3.1. Whisker bend correction and surface position accuracy. (A) Head-plate design and implantation relative to Bregma. (B) Follicle position was measured at rest in X, Y stereotactic coordinates from Bregma. (C) A subset of trials were imaged with a high-speed camera (220 FPS, GC660 camera, Allied Vision) calibrated to measure distances within the plane of the whiskers (MATLAB 2014b Machine Vision Toolbox). The high speed linear CCD array (4 kHz) used for whisker imaging in the study was projected into this plane (purple) and a straight line was projected from the follicle (imaged separately) to the stimulus cylinder (C1, red; C2, blue). These projections are identical to those inferred from the CCD array imaging alone. True whisker position is shown in yellow with true surface contacts identified manually (blue circles). Black double arrows indicate C1 and C2 bend error arc distances (straight line projection – true contact position). (D) C1 (red) and C2 (blue) bend error are plotted vs. whisker position in degrees. Each point is one frame (n= 316 C1 frames and n= 240 C2 frames measured in 1 mouse), which were then fit with a Gaussian curve. (E) Histograms of bend error residuals from Gaussian fit for C1 (top; |mean error| ± CI_{95} = 0.15 ± 0.16 mm) and C2 (bottom; 0.41 ± 0.16 mm). Dashed lines show ± 1 standard deviation (C1 = 1.4mm, C2= 1.28 mm).

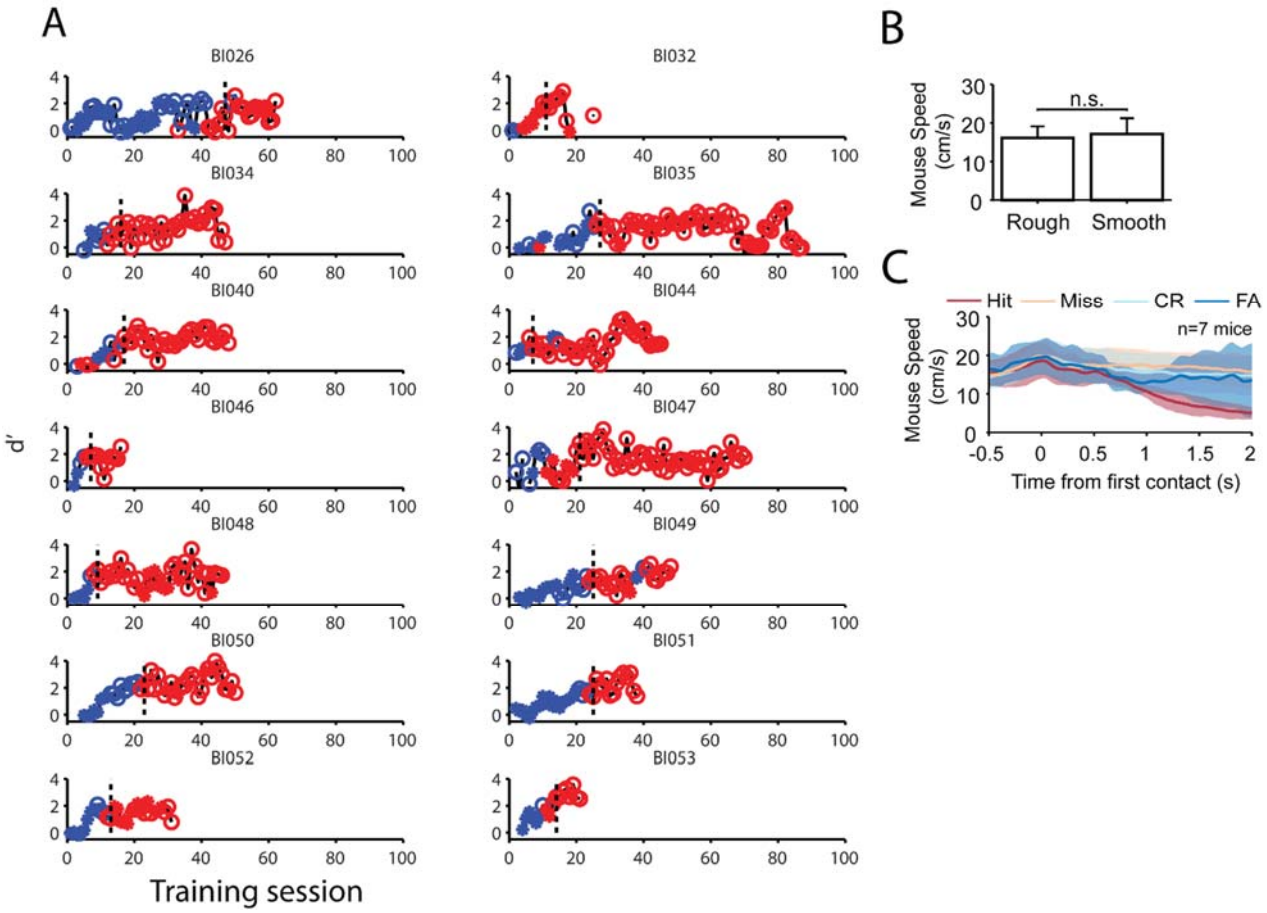

Supplemental Figure 3.2. Behavior training time course and running speed. (A) Rough vs. Smooth d' vs. training session in all mice that learned the task (n= 14). Four different stages of training were used: starting with fixed velocity delivery (blue) in blocks (asterisk) then randomized (circle), followed by closed-loop delivery (red) in blocks (asterisk), and finally randomized (circle). Dashed lines indicate criterion performance (2 days above 75% correct on closed-loop, random). (B) Mean running speed on Rough and Smooth trials (p= 0.22, paired t-test, n=7 mice). Bars represent mean ± CI_{95}. (C) Mean running time course for each behavioral outcome (Hit, Miss, Correct Rejection (CR), False Alarm (FA)) centered on first contact (Figure 3.1C). Mean ± CI_{95}. (n=7 mice).

Slip whisker motion events are a potential cue for Roughness

To investigate the mechanisms underlying Rough vs. Smooth texture discrimination, we examined transient high-amplitude whisker acceleration micromotions (slips) previously shown to correlate with surface roughness (Ritt et al., 2008; Wolfe et al., 2008). We identified all slips above a ±2.5 s.d. threshold (Figure 3.2A). This threshold was chosen because we observed that slips > ±2.5 s.d. began to drive spikes in S1 single units (see below). We analyzed whisker slips and other whisker kinematics in a palpation window defined as beginning 50ms before First Contact and ending 200ms before first lick (Figure 3.2B). Palpation window duration varied from trial to trial due to differences in

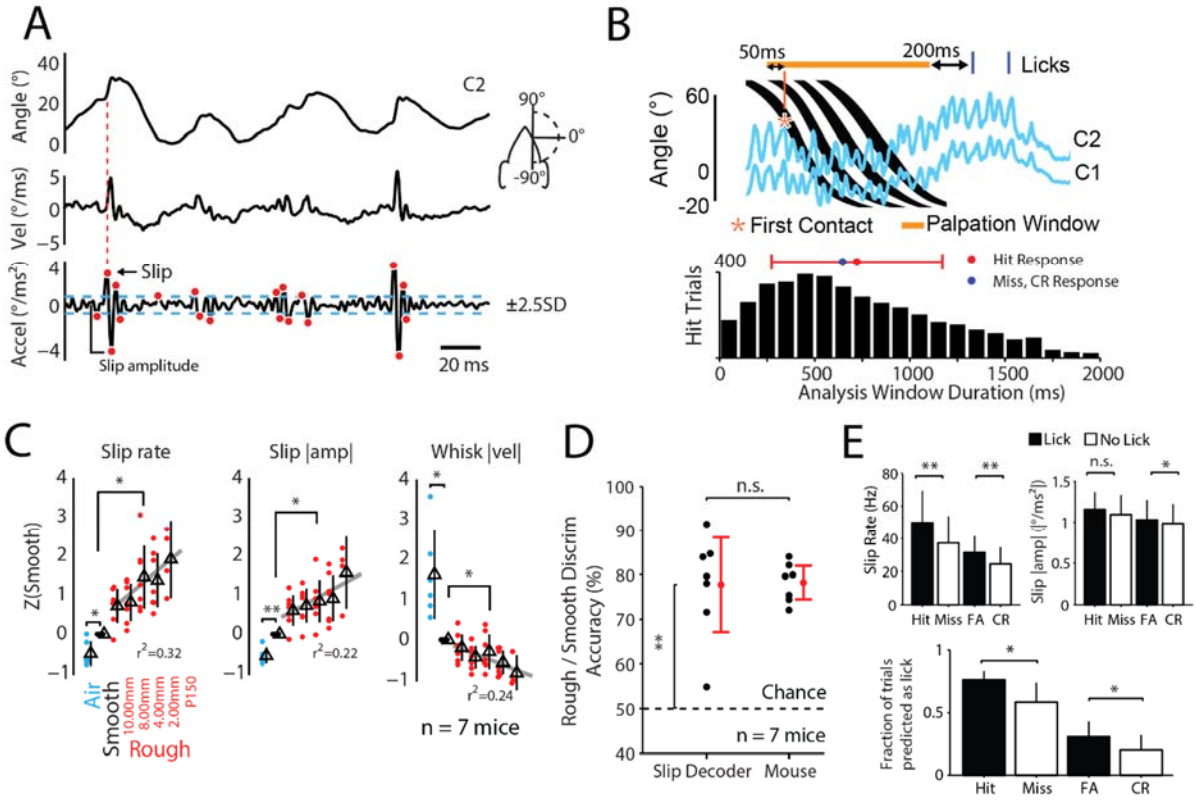

Figure 3.2. Slip events are a potential cue for rough surfaces. (A) Whisker position, velocity and acceleration example from C2 whisker. Bottom: Slips (red) identified from ±2.5SD thresholded on acceleration traces and absolute slip amplitude measurement method ("Slip amplitude"). (B) Hit trial palpation window (orange bar) defined as 50ms before first contact (asterisk) to 200ms before the first lick (blue ticks; Top). Bottom: Distribution of palpation window durations from Hit trials. Mean ±SD in red. The 650ms window used for Miss and Correct Rejection (CR) non-response trials is indicated in blue. (C) Mean slip rate, slip |amplitude|, and whisker speed (|velocity|) during palpation windows described in (B), z-scored to Smooth for each animal (averaged over C1 and C2 whiskers, one-way ANOVA with post-hoc paired t-test on air (blue) , Smooth (black), and combined Rough (red); points are individual mice; n=7 mice). Grey lines and r-square values describe linear fit of z-score vs. spatial frequency (arbitrary units with uniform spacing) in Rough stimuli. All slopes significant at α= 0.05, linear regression t-test. (D) Accuracy of a logistic GLM using C1 and C2 whisker slip rate and |amp| as predictors for whether a trial was Rough or Smooth ("Slip decoder", 10-fold cross-validated accuracy within mouse (black dots), n=7,284 imaged trials). Model accuracy compared to chance (50%, one way t-test) and mouse behavioral accuracy on same trials (p=0.91, paired t-test, n=7 mice). (E) Top: Left, Mean slip rate (Left); Right, |amp| compared between Lick (black) and No Lick (white) trial types within Rough (Hit, Miss) and Smooth (FA, CR) trials. Bottom: fraction of trials classified as "Lick" trials from slip rate and |amp| (model implemented as in (D)). Error bars represent mean ± CI_{95} ; * $p < 0.05$, ** $p < 0.01$, paired t-test with n=7 mice unless otherwise noted; Dunn–Šidák corrections for MC; a.u. = arbitrary units.

running speed and lick time (722ms ± 454ms, mean ± s.d.; Figure 3.2B). On non-response trials (CR, Miss), a 650ms window was used.

We measured mean absolute slip amplitude, slip rate, and mean absolute whisker velocity (speed) within this palpation window. Results are given for C2 whisker data unless stated otherwise. Smooth surfaces generated 28.3 ±0.8 slips/s at a mean amplitude of 1.0 ±0.01 $^{\circ}/ms^2$ (n=3,355 Smooth trials; 29 imaging sessions in 7 mice). We z-scored slip rate and amplitude to Smooth data values in each mouse. Slips were significantly greater on Rough surfaces and decreased in air, relative to Smooth trials (Figure 3.2C). Within Rough stimuli, slip rate and amplitude increased with spatial frequency (Figure 3.2C). By contrast, mean speed was reduced on Rough surfaces and decreased with increasing spatial frequency (Figure 3.2C). Decreased whisker speed correlated with decreased whisking amplitude (Figure 3.S3A-B) while whisking frequency remained constant (18 ± 0.1 Hz; Figure 3.S3C-D). Therefore, surface

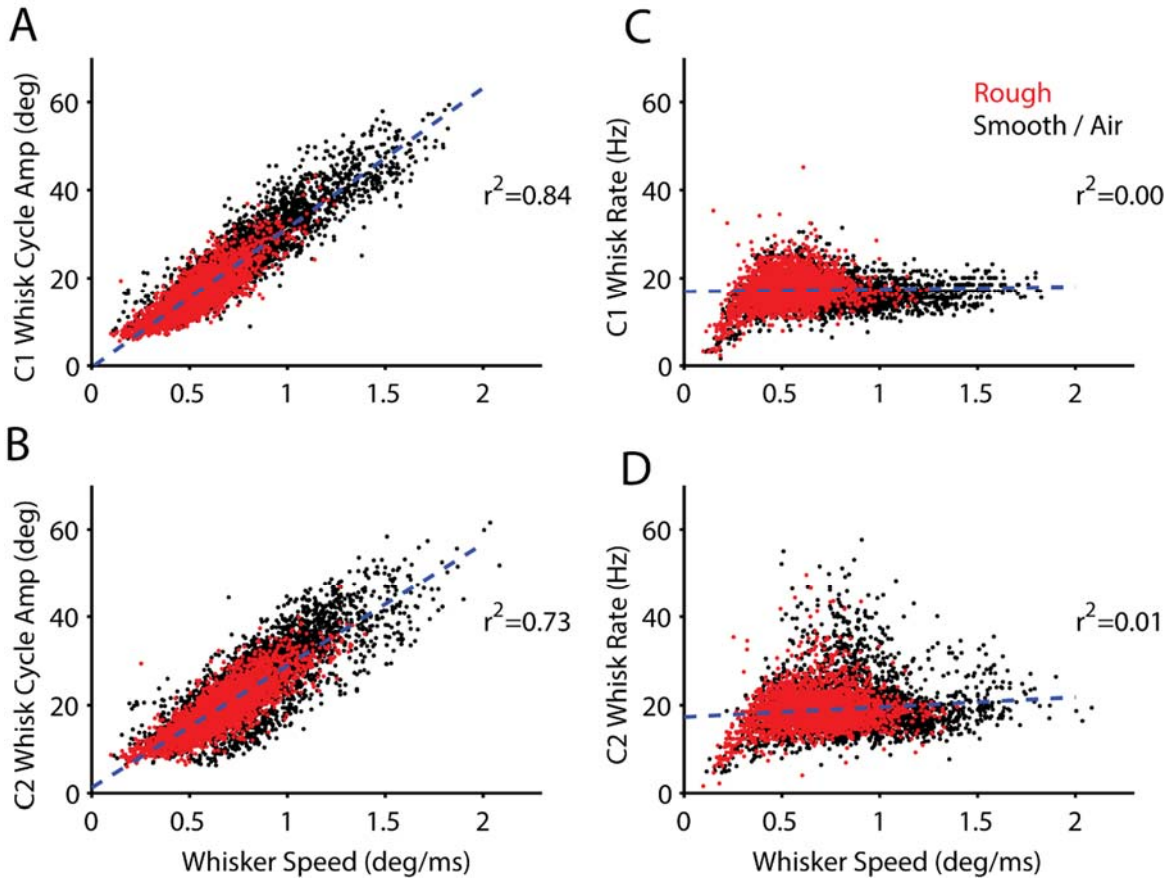

Supplemental Figure 3.3. Whisk amplitude changes with whisker velocity while whisk rate remains constant. (A) C1 mean whisk cycle amplitude in degrees (per trial) vs. mean whisker speed (per trial; absolute velocity). Each point is one trial (n= 7,463 imaged trials), 3,402 Rough (red), 4,061 Smooth or Air trials (black). R-squared indicated for linear fit to all trials (dashed blue line). (B) Same as (A) but for C2 whisker. (C) C1 mean whisk rate in Hz (per trial), vs. mean whisker speed (per trial). (D) Same as (C) for C2 whisker.

roughness was accompanied by increased slip rate and amplitude, as observed previously on sandpapers (Jadhav et al., 2009; Wolfe et al., 2008), and decreased whisker speed due to lower whisk amplitude.

Whether slips can accurately code roughness on a single-trial basis is unknown. To test this, we fit a logistic GLM to classify Smooth and Rough trials based on C1 and C2 whisker slip rate and amplitude (10-fold cross-validation; see Data Analysis methods). This model predicted stimulus identity on hold-out trials with 77.6 ± 11% accuracy**,** significantly above chance ($p < 0.001$, one-way t-test against chance, n=7 mice; Figure 3.2D). This discrimination accuracy was significantly different from individual mouse behavioral discrimination accuracy (78 ± 4%) on the same trials ($p=0.91$, paired t-test, n=7 mice; Figure 3.2D).

If slips contributed to the mouse's decision, we would expect more slips on trials that generated Lick responses than during trials with No Lick response. To examine this, we measured slip rate and amplitude in Lick and No-Lick trials (Figure 3.2E; Lick: Black; No-Lick: White). We found a higher rate of slips and higher amplitude slips during FA trials than CR trials, and a similar trend in Hit vs. Miss trials (Figure 3.2E; Top). To examine whether this difference could predict lick behavior, the slip logistic GLM described above was refit to classify Lick and No-Lick trials. The slip-based model predicted licks significantly more often on trials that indeed caused mice to lick (Figure 3.2E; Bottom). This suggests some lick responses may have been the result of strong slip input to the whisker system, even on Smooth trials. Taken as a whole, these findings suggest slips are a potent cue for stimulus roughness in behaving mice and that slips carry information that can predict mouse discrimination behavior.

Slips cluster at bar edges, potential cue for local geometric features

How the whisker system detects specific local surface features, like bar edges, is unknown. Because gratings are raised and have spatially sharp edges, they are likely to locally increase whisker bend and the local coefficient of friction, which may increase the probability of whisker slip events. To test whether slips cluster at bar edges, we plotted the prevalence of slips as a function of position of the whisker on the stimulus surface (Figure 3.3). Slips did not occur homogenously across surfaces (Figure 3.3A; single trial example). This clustering was especially apparent across trials (Figure 3.3B; single daily session). Across mice, slips were spatially modulated and tended to cluster at leading bar edges (Figure 3.3C, n=29 session in 7 mice). The leading edge of the P150 sandpaper (which was raised to match grating height: 0.8mm) also caused a cluster of slips (Figure 3.3B and 3.3C, "P150"). Slips tracked the spatial modulation of bar onsets for 4-10mm periods, but become less spatially precise for the 2mm, where the whisker tips often bent across two bars instead of hitting individual edges (Figure 3.S4A).

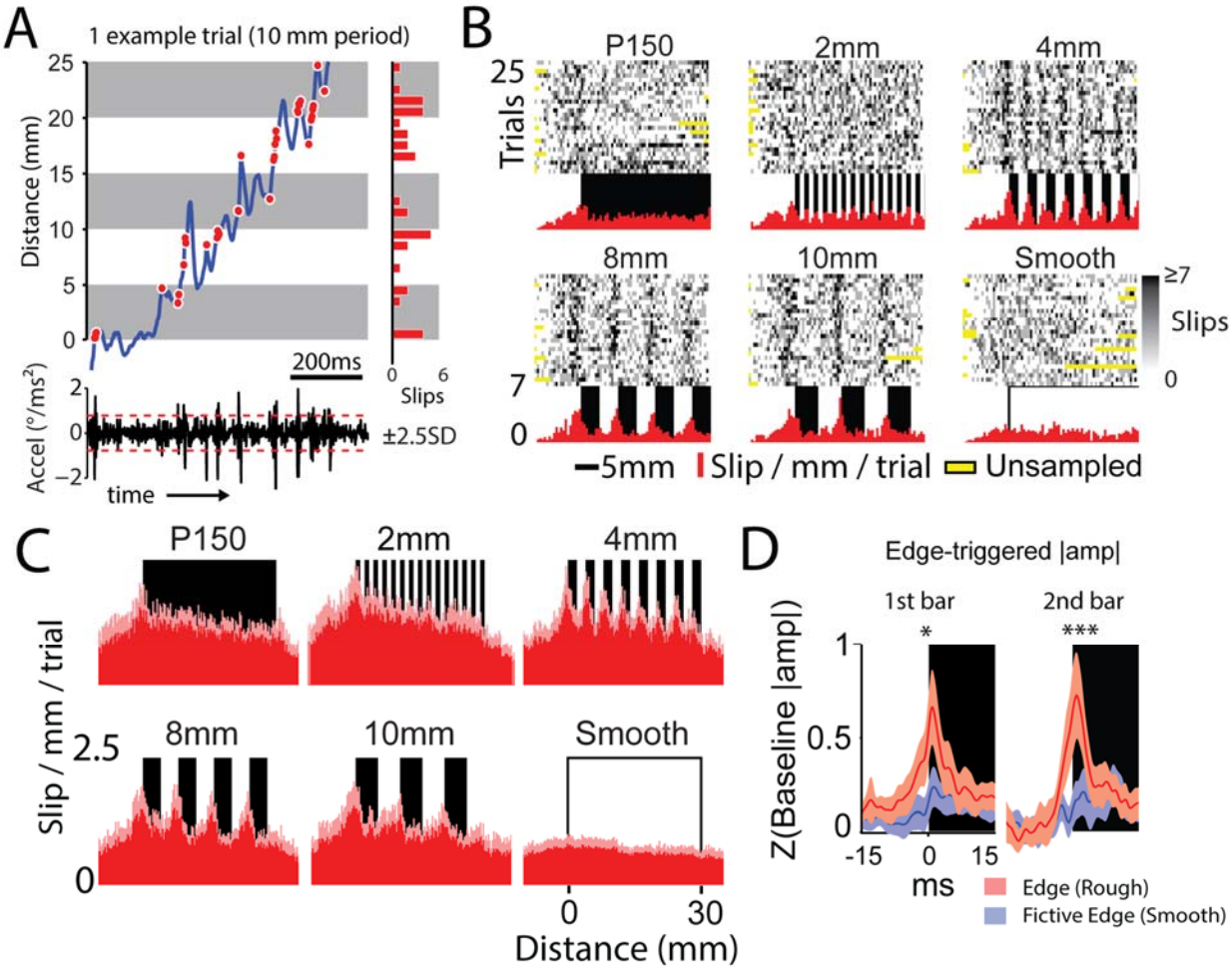

Figure 3.3. Slips cluster on stimulus micro-features, including ridges. (A) Left: C2 whisker position during a single trial on the 10mm grating. Slips are red dots. Right: histogram of slips/mm aligned to grating bars for (Left). (B) Top: mean slip density for each trial (rows) on one example day; yellow, unsampled areas. Bottom: mean spatial histogram (slips / mm / trial) for each stimulus (n=25 trials). (C) Mean spatial histogram across all imaging sessions with CI_{95} (pink; n=29 sessions, 7 mice). (D) Mean ± CI_{95} edge-triggered |amp| for C2 whisker across first and second bar edges for all grating stimuli (red) and equivalent cylinder positions on the Smooth stimulus (blue; n=28 sessions, 6 mice). Traces were z-scored to a 30ms baseline preceding edge-crossing (-40 to -10ms). * $p < 0.05$, *** $p < 0.001$; 2-way ANOVA with repeated measures with Rough and Smooth as factors; n=6 mice, 28 sessions, analyzed across time points ± 5ms from edge.

The above analysis identified slips exceeding a specific acceleration threshold. In an alternative analysis without thresholding, we calculated the edge-triggered acceleration amplitude as the C2 whisker first crossed bar edges in the forward direction (Figure 3.3D; red), or crossed equivalent cylinder positions on the Smooth stimulus (fictive edges; Figure 3.3D; blue; n=28 imaging sessions in 6 mice). Upon crossing a bar edge, C2 whisker acceleration amplitude increased above baseline

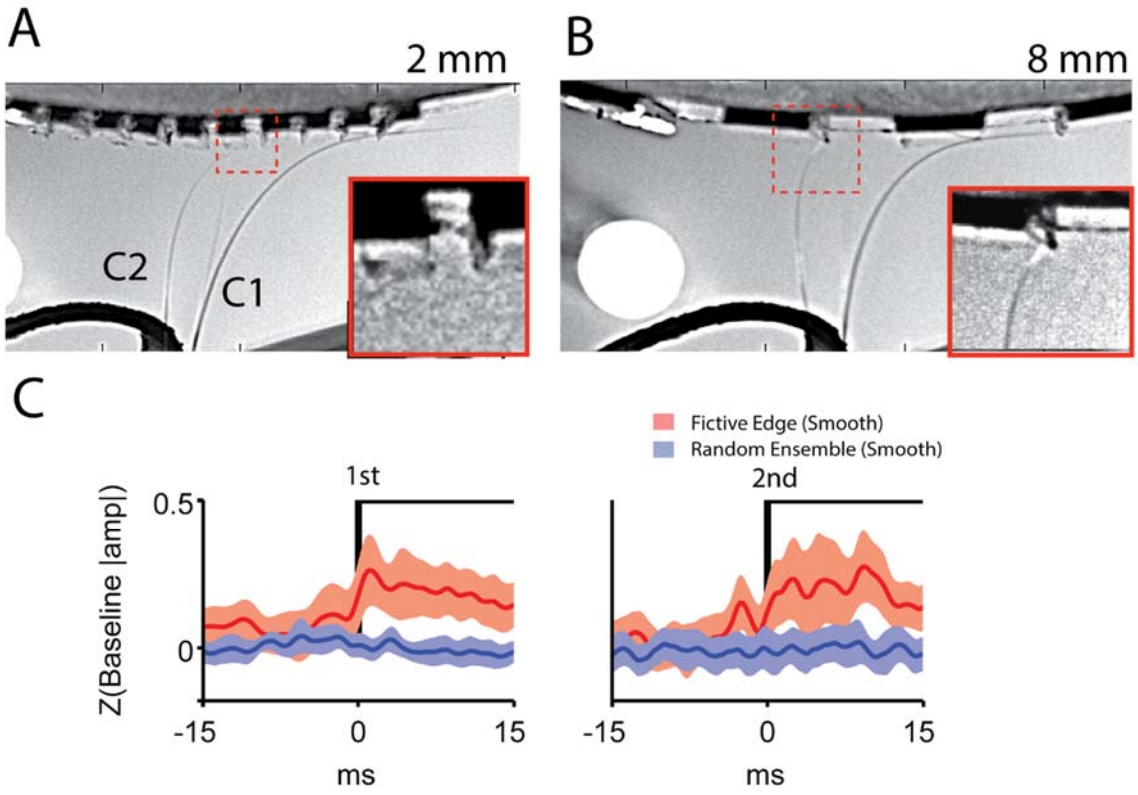

Supplemental Figure 3.4. Details for whisker behavior on gratings and Smooth. (A) Image of C1 and C2 whiskers on 2 mm grating. Inset image shows C2 whisker bent across gap (corresponds to dashed red box in larger image). (B) Image of C1 and C2 whiskers on 8 mm grating. Inset image shows C2 whisker hitting ridge of bar. (C) Mean ± CI_{95} 1st and 2nd fictive edge-triggered accelerations (|amp|) for C2 whisker, z-scored to a 30ms baseline on Smooth trials (red; re-plotted from Figure 3.3D). In blue: the mean |amp| when acceleration clips were sampled randomly from Smooth trials using same number of events per trial as Fictive Edge crossing (n=6 mice, 28 sessions). Random clips include epochs of the whisker moving forwards as well as backwards while fictive edge crossings are biased towards forward movement.

(Figure 3.3D; Left, 1st bar increase: 0.73 ±0.22 SD; 2nd bar increase: 0.81 ±0.26 SD; mean ± CI_{95} of z-score; n=28 sessions in 6 mice).

A small increase in acceleration amplitude also occurred when the whisker first crossed fictive edges (1st bar increase: 0.26 ± 0.12 SD, 2nd bar increase: 0.27 ± 0.12 SD, mean ± CI_{95} of z-score; n= 28 sessions in 6 mice). Because we only analyzed first position crossings, the ensemble was biased towards forward whisker movements resulting in a non-zero average acceleration. This bias was not apparent in acceleration ensembles drawn randomly from Smooth trials, which includes forward and backward movements (Figure 3.S4B). Comparing the bar-edge and fictive edge-triggered acceleration amplitude averages revealed a significantly larger acceleration on bar edges compared to fictive edges (Figure 3.3D). Thus, edges caused an increase in the local number and magnitude of slip whisker micromotions.

S1 coding of whisker touch and surface roughness

To determine how whisker touch, roughness, and local ridge geometry are encoded in S1 we made extracellular single-unit recordings using multi-site linear probes in 15 penetrations in 5 mice while they performed the Rough-Smooth discrimination task. Measurements were made in C1 or C2 whisker columns, targeted by intrinsic signal

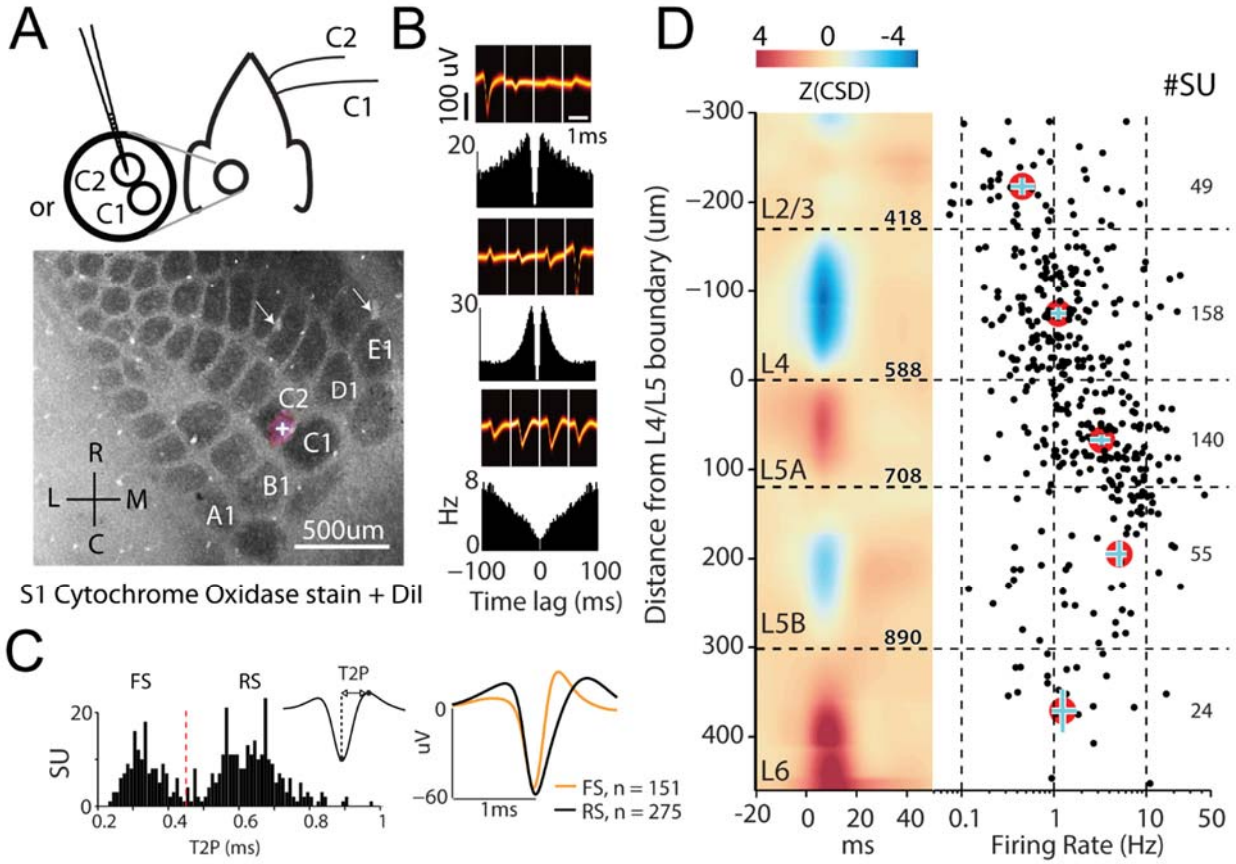

Figure 3.4. Extracellular single units recorded in S1. (A) C1 or C2 column targeted with intrinsic signal optical imaging (ISOI) before recording. Below, example S1 barrel field stained with cytochrome oxidase to reveal L4 barrels; fluorescent DiI electrode track shown in C2 column (pink + white arrow). Rostral white arrows indicate fiducial tracks (500µm). (B) Spike waveforms from 3 example single units (SU) measured simultaneously in an example recording. Top: 2D histograms of overlapping SU waveforms (orange) recorded on four adjacent electrode sites of linear probe. Bottom, spike auto-correlation for each unit. (C) Left: Trough-to-peak time (T2P) measurements on example spike waveform (inset). Histogram of SU T2P times with FS threshold indicated at 0.45ms (red dashed line). Right: mean FS and RS waveforms using this threshold. (D) Left: mean slip-evoked current source density (CSD) across all recordings (n=15 recordings, 5 mice, z-scored within mouse). CSDs were aligned to L4-L5 boundary. Layer depths from pia inset in black (Lefort et al., 2009). Right: mean firing rate for each SU (black dots) across all behavioral epochs (n=426 SU). Inset: units identified per layer. For each layer, red circle centered on ($median_{rate}$, $mean_{depth}$) with bootstrapped ± CI_{95} in blue.

optical imaging (ISOI) and multi-unit (MU) whisker tuning under transient isoflurane anesthesia and confirmed by fluorescent tracer relative to histologically stained barrels (Figure 3.4A). We isolated single units by spike-sorting from 4 adjacent channels treated as one tetrode (Figure 3.4B; see: Experimental Procedures). We distinguished fast spiking (FS) from regular spiking (RS) units based on trough-to-peak width (T2P) of the average spike waveform from the peak channel (0.45ms threshold, Figure 3.4C). Unit depth was determined relative to the location of the L4-L5A border, inferred from slip-evoked current source density (CSD; Figure 3.S5) calculated from simultaneously recorded local field potentials (LFP) (Figure 3.4D, Left; see: Experimental Procedures). Overall, 426 units were isolated spanning L2/3 to L6 (Figure 3.4D, Right). Firing rates were low and skewed

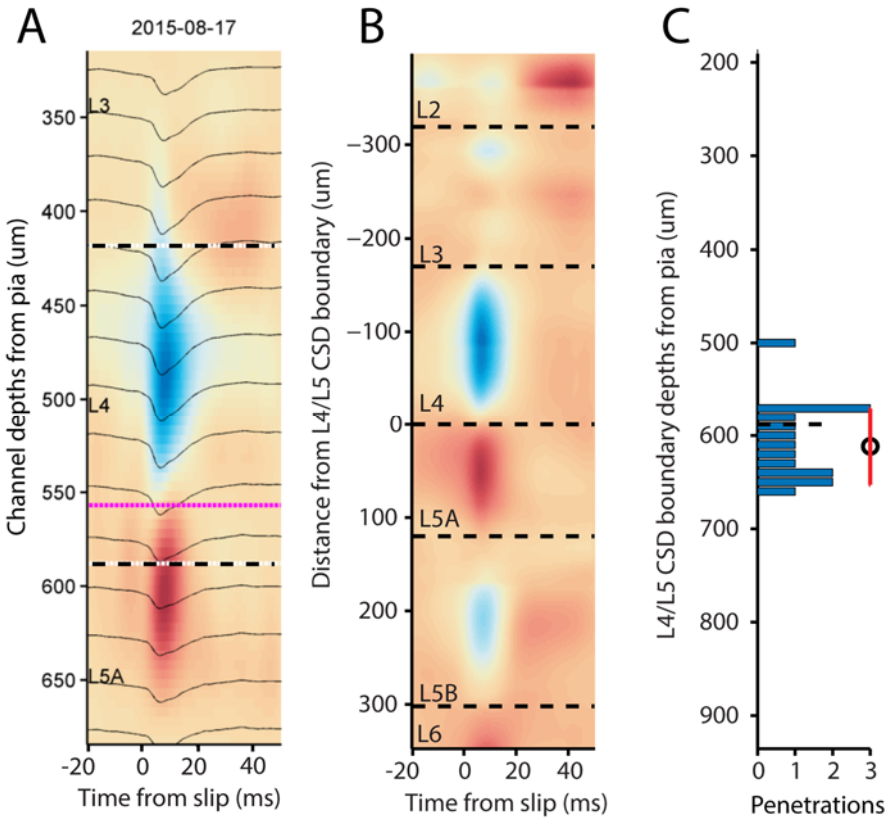

Supplemental Figure 3.5. Current source density L4 / L5 boundary. (A) Example CSD from one penetration calculated from n= 4,720 slips. Mean LFP traces (black) for 15 of 16 channels on linear probe (25um site spacing). Black dashed lines indicate S1 cortical layer boundaries as reported in (Lefort et al., 2009). Pink line indicates the L4/L5 boundary detected in the CSD. (B) Mean composite CSD from n= 15 penetrations aligned to L4/L5A boundary. (C) Histogram of CSD L4/L5A boundary depth from pia measured for each penetration (mean depth = 611.6 ± 22.8 μm; 10 μm bins). Black dashed line indicates 588 μm layer boundary (Lefort et al., 2009).

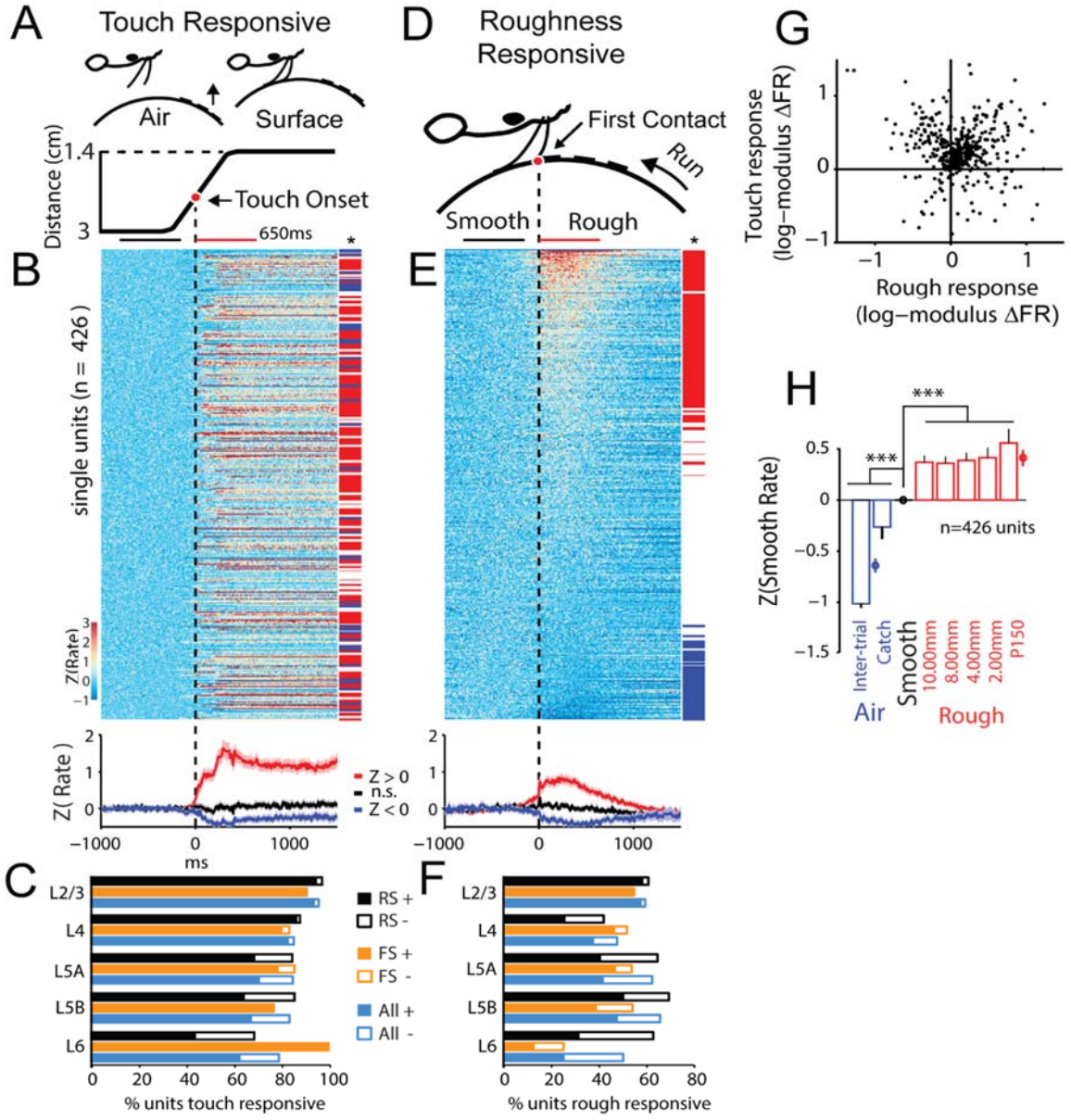

Figure 3.5. S1 coding of whisker touch and surface roughness. (A-C) Measurement of touch responsiveness from static stimulus cylinder onset before trials. (A) Time course of stimulus cylinder distance during translation towards mystacial pad. 650ms palpation windows indicated for Air (black) and surface contact (red). Touch onset (red dot) occurred ~2.2cm from the mystacial pad. (B) Top: Mean response of each unit (rows, n = 426 SU, 5 mice), z-scored to firing rate in Air (zPSTHs, see: Experimental Procedures). Right: SU touch responses indicated with tick for $p < 0.05$ (paired t-test of firing rate between palpation windows in (A)). Within responsive units, red ticks indicate SU that increased firing to touch ($Z > 0$), blue, decrease ($Z < 0$). Bottom: mean ±CI95 zPSTH for categories of SU response: increased (red), decreased (blue), or not responsive (black). (C) Percent of FS (orange), RS (black), or all units (blue) in each layer that showed significant responsiveness via increases (+) or decreases (- , white fill) in spiking. (D-F) Same as (A-C) but for roughness onset. (D) Schematic of closed-loop roughness onset with 650ms

palpation windows for measuring preceding smooth (black) and onset of roughness (black). (E) Top: zPSTHs sorted by roughness response with significance indicated by ticks, as in (B). Rows of (E) and (B) correspond to the same SU. (F) Percent of FS and RS in each layer that showed roughness responsiveness, as analyzed in (C). (G) Log-modulus of mean firing rate changes for touch vs. roughness (n = 426 units, see: Experimental Procedures) (H) Bars indicate mean ± CI95 unit response to each behavioral trial type (Catch n= 561, Rough n= 2,447, Smooth n= 2,083) or epoch ("inter-trial," n= 5,688), z-scored to Smooth trials. Unit responses analyzed in identical window to slip analysis in Figure 3.3. Mean ± CI95 for Air (blue), Smooth (black), and Rough (red), indicated as circles ($p<0.001$, ANOVA with post hoc paired t-test, Dunn–Šidák correction for MC). * $p < 0.05$, *** $p<0.001$.

in L4, L2/3 and L6, and higher in L5. Median firing rates per layer were, L2/3: 0.45 ± 0.14 Hz; L4: 1.12 ± 0.22 Hz; L5A: 3.29 ± 0.82 Hz; L5B: 5.10 ± 1.26 Hz; L6: 1.24 ± 0.41 Hz (± CI_{95} of median).

We first quantified unit responses to touch and roughness (Figure 3.5). Touch responsiveness was measured by comparing firing rates in 650ms windows before and after the static introduction of the stimulus cylinder (Figure 3.5A). Touch onset was defined as occurring 400ms before the final stimulus cylinder position (1.4cm), equal to a distance of 2.22 ± 0.05 cm from the mystacial pad. As expected in S1, touch drove a significant change in firing rate in the majority of units ($p < 0.05$, paired-t-test on firing rate; 85.9%, n=366 units; Figure 3.5B, colored ticks), distributed evenly across layers (Figure 3.5C). Of touch responsive units, 89.6% were touch-excited (Figure 3.5B, red) and 10.4% were touch-inhibited (Figure 3.5B, blue). The majority of touch-inhibited units were RS units in L5-6 (78.0%, n=46; Figure 3.5C).

Prior literature has suggested that rough and smooth surfaces are encoded by different mean firing rates in S1 (Arabzadeh et al., 2005; von Heimendahl et al., 2007; Jadhav et al., 2009). We quantified this by measuring unit firing rate to Rough trials centered on First Contact (Figure 3.5D), which marks the forward movement of a whisker from smooth to the onset of a rough surface. Rough surface onset drove significant changes in the firing rate of 56.1% of units ($p <0.05$, paired t-test on firing rate, n=239; Figure 3.5E, colored ticks), 74.1% of which increased firing on roughness (red) and 25.9% of which decreased firing (blue). To provide a visual comparison of touch and roughness responses, units in Figure 3.5B and 3.5E were sorted by roughness response and again compared across layers (Figure 3.5F). While many units that increased firing to touch increased further to roughness, 31.8% of touch-increased units decreased firing to roughness (Figure 3.5G), exposing a response non-linearity. There was a significant interaction between RS unit roughness responsiveness and unit location (in L4 vs. outside L4; $p=0.001$, $\chi^2=10.72$, d.f. = 1; Figure 3.5F). Indeed, 82.7% (134 / 162) of responsive RS units were located outside of L4 (extragranular, L2/3 and L5-6). This interaction was not observed in FS units ($p= 0.84$, $\chi^2=0.04$, d.f. = 1).

Finally, we tested whether average unit responses to Rough and Smooth stimulus trials differed in the palpation window. Firing rates for each unit were z-scored to Smooth trial responses (Figure 3.5H). On average, units in S1 fired more during Rough trials than Smooth trials ($p < 0.001$; paired t-test, n = 426 units). As expected, units fired less than Smooth during epochs of whisking in air, which consisted of Air

catch trials with trial structure but no touch, and quiescent inter-trial epochs with no

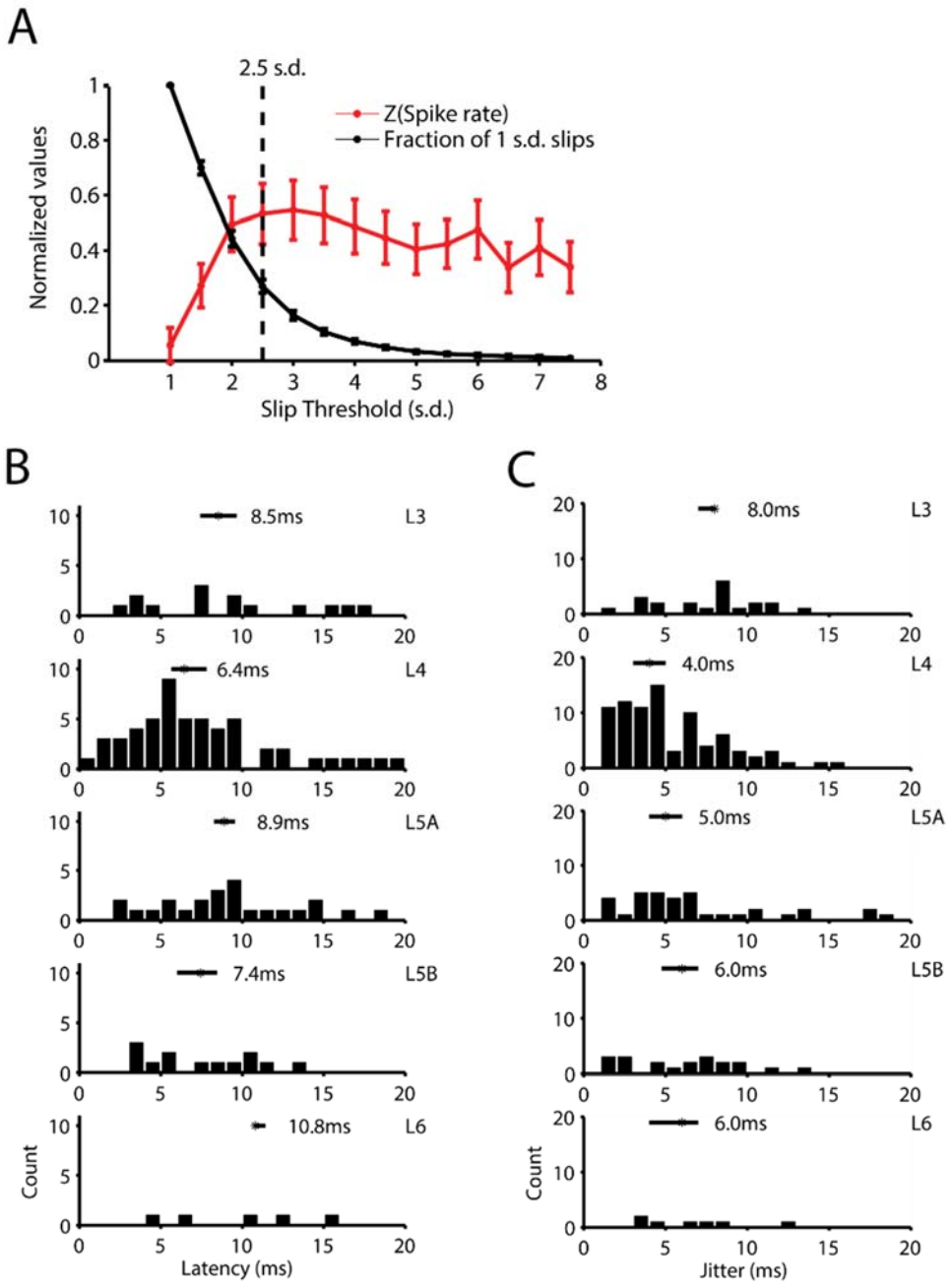

Supplemental Figure 3.6. Slip spike response characteristics. (A) In black: the mean fraction of 1 s.d. slips used per session at each slip threshold (mean ± CI_{95}). Mean number of slips per recording at 1 s.d. = 9,084 ± 2,373 slips (n= 15 recordings). In red: the mean slip-evoked spikes z-scored to baseline (n=426 units) vs. slip threshold (mean ± CI_{95}). (B) Histograms of spike latency for slip-responsive units in each layer using the bin-less Poisson method (median ± bootstrapped CI_{95}). (C) Histograms of spike jitter for slip-responsive units in each layer using full width at half maximum of response peak (median ± bootstrapped CI_{95}).

touch and no trial structure ($p < 0.001$; paired t-test, n=426 units; Figure 3.5H). Therefore, touch strongly increased S1 unit firing across cortical layers, while surface roughness drove more varied responses, particularly within extragranular RS units.

S1 coding of slips and ridges

How S1 neurons encode spatially localized surface features is unknown. We studied how S1 encodes localized features by focusing on slips (temporally localized features) and ridges (spatially localized features. We first analyzed coding of slips by firing rate in individual S1 units. We identified all slips ≥ 2.5 SD for a recording session, and compared spike rate in 20ms windows before and after the peak of slip. A slip-aligned raster for an example unit is shown in Fig. 6A. Slips altered firing rate in 43.9% of S1 units (n=187/426 units). Across units, average spike responses increased with slip amplitude (Figure 3.6B, all layers), with strongest responses occurring for slips ≥ 2.5 s.d. (Figure 3.6B, red dashed line, Figure 3.S6A). L4 had the shortest slip response latency (6.4 ± 1 ms, median ± bootstrapped CI_{95} Figure 3.S6B), and highest temporal precision (4 ± 1 ms jitter, median ± bootstrapped CI_{95}, full width at half maximum of response peak; Figure 3.S6C). L4 also contained the highest proportion of slip responsive units (55.7%; Figure 3.6C, L4 blue bar). Across layers, significantly more FS units (64.9%) responded to slips than RS units (32.7%; $p<0.001$, $z=6.47$, 2-way z-test of proportions; Figure 3.6C). In addition, while the majority of slip responsive units (88.8%) increased firing in response to slips (Figure 3.6C, solid bars), 20.2% of slip responsive RS units decreased in response to slips, compared to only 3.1% of slip responsive FS units (Figure 3.6C, open bars).

We analyzed coding of ridges similarly, comparing firing rate in a 20ms window before and after the whisker crossed each ridge (Figure 3.6D). We considered whiskers crossing onto and off of bars as ridge-crossing events. 11% of units were significantly responsive to ridges (n = 48 units). On average, units showed a small increase in firing rate to ridge crossing (Figure 3.6E), with ridge responses most prevalent in L5B (21.5% of L5B units, Figure 3.6F). Ridges evoked firing rate increases in most L2/3, L4 and L5B units, but decreases in most L5A and L6 units. We next asked whether units that responded to localized features (slips and ridges) also responded to touch and roughness (Figure 3.5). Unit responses were highly overlapping across stimulus categories, with 28.6% of units responding to all three features of touch (n=122/426 units; Figure 3.6G). 94.4% of slip and ridge responsive units were also touch responsive (Figure 3.6G, blue and black), and 61.9% were also roughness responsive (Figure 3.6G, red and blue). Only 5.6% of units did not respond to one of these three features (n = 24, Figure 3.6G, white).

The tactile system, up to the level of S1, is widely thought to generate a spatially isomorphic representation of the tactile world, but this has not been studied during natural, active tactile sensation, where irregular sensor movements, variable forces, and sensory reafferent signals will complicate coding (Weber et al., 2013). To address this, we tested whether S1 spikes clustered in space near individual ridges, similar to whisker slips (Figure 3.3). We plotted the mean spatial density of spikes for each unit, relative to spatial position of the whisker along the stimulus surface (Figure 3.6H). Spike

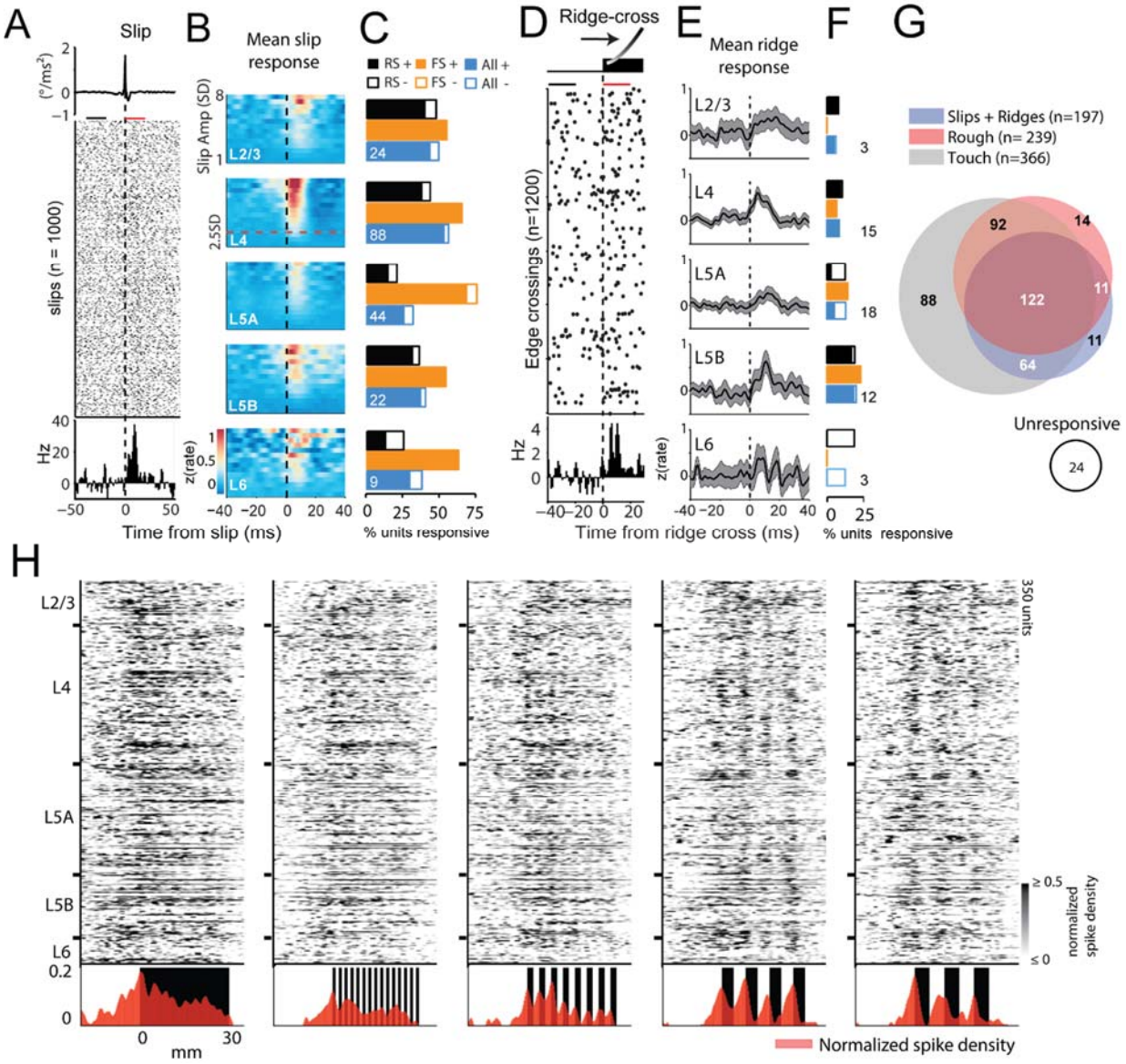

Figure 3.6. S1 coding of slips and ridges. (A) Slip aligned spike raster for an example L4 FS unit, shown relative to the mean whisker slip event (top). Bottom, baseline-subtracted slip-locked PSTH for this unit. (B) Average slip-locked zPSTHs for each layer. Rows in each pseudocolor plot correspond to different amplitudes (1-8 s.d. in 0.5 s.d. bins, n = 426 units). PSTHs were z-scored to a 20ms pre-slip baseline (black bar in A). Red dashed line, 2.5 S.D. threshold for slip analyses. (C) Fraction of units that were significantly slip-activated (solid) or slip-inhibited (open) for all units (blue), RS (black) or FS (orange) in each layer. Significance for each unit was determined by paired t-test on spike counts from baseline vs. response windows (a = 0.05). Numbers show total number of responsive units per layer. (D-F) Same as (A-C) but for ridges. (D) Spike raster for example unit aligned to ridge crossing. (E) Average ridge-locked zPSTHs for each layer for all units (n=426 units). PSTHs were z-scored to the pre-ridge baseline period (black bar in D). (F) Fraction of ridge-responsive units in each layer, plotted as in (C). (G) Venn diagram of how kinematic responsive units (slips + ridges, blue) overlap with touch (black), and roughness (red) units as identified in Figure 3.5.

Units that did not respond to any of these features are shown in a separate circle ("unresponsive", n=24 units). Numbers indicate unique units (total = 426 units). (H) Mean normalized spike density for each unit recorded in the C2 column, relative to spatial position of the whisker along stimulus cylinder (n=350 units). Rows are sorted by unit depth; layer boundaries indicated. Normalized spike density = (SCrough – SCsmooth) / max(SCrough– SCsmooth), for each unit (SC = mean spike count / mm). Bottom: Population mean normalized spike density per unit, relative to position of bars or sandpaper patch.

density was normalized relative to the corresponding spatial position on Smooth as $(SC_{rough} – SC_{smooth})$ / $max(SC_{rough}– SC_{smooth})$, where SC = mean spike count per mm of whisker travel. We observed clear structure in which spike density increased at ridges on the 4, 8 and 10 mm gratings, and increased broadly for sandpaper and 2 mm grating. This locally increased spike density reflects both local spike rate increases and increased whisker dwell time on ridges, thus accumulating S1 spikes when the whisker is at specific spatial locations. Note that time is not explicitly represented in this calculation, but that this spatial spike code could be created in the brain if S1 spikes were combined with a whisker position signal, such as has been reported in primary motor cortex (Kleinfeld and Deschênes, 2011) and cerebellum (Chen et al., 2016). Thus, ridge- and slip-evoked spikes in S1 are a potential building block of a spatial representation of local surface geometry in the brain. Together, these results show that slip- and ridge-evoked spikes contribute to both spatial coding of fine surface geometry, and a mean rate code for roughness generated by increased spiking to local features.

Decoding single Smooth and Rough trials with and without slip-associated spikes

While whisker slips and S1 firing rate correlate with roughness (von Heimendahl et al., 2007; Jadhav et al., 2009), inter-trial variability is high, and it remains unknown whether Rough vs. Smooth can be accurately decoded from S1 and whether slip-evoked spikes contribute to stimulus decodability. To test these questions, we analyzed spiking in simultaneously recorded units from 15 sessions in 5 mice (range 6 - 50 units, mean = 28.4 units/session). An example Rough trial with spikes of 32 units is shown in Figure 3.7A. For each trial, we calculated mean firing rate for each unit (Figure 3.7A; bar plot) within the palpation window. The mean firing rate per unit was higher on Rough (5.61 ± 0.76 Hz, n=426 units, 2,447 trials), than Smooth (4.57 ± 0.68 Hz, n=426 units, 2,083 trials; $p < 0.001$; z-test on z-scored Rough responses; Figure 3.7B).

To determine whether this increased firing rate was due to increased slips, we removed all spikes associated with slips of the columnar whisker, defined as spikes <20ms after slip peak (slip spikes removed (SSR); Figure 3.7C). This approach removed an equal proportion of time on Rough (22.9 ± 3% time removed / trial / session, n= 15 sessions) and Smooth (22.8 ±3% time removed; p=0.66, paired t-test, n= 15 sessions; Figure 3.S7A). SSR abolished the difference in mean unit firing rate between Rough and Smooth (p=0.374, z-test on z-scored Rough responses, Rough: 2.72 ± 0.38 Hz, Smooth: 2.93 ± 0.42 Hz; n=426 units; Figure 3.7D). As a control, we removed spikes in an equal number of 20ms windows that did not contain slips (non-slip spikes removed (NSR); Figure 3.7E). With NSR, mean firing per unit remained higher on Rough (4.42 ± 0.60 Hz) vs. Smooth (3.41 ± 0.51 Hz; $p <0.001$, z-test on z-scored

Rough responses, n=426 units; Figure 3.7F), despite the fact that NSR removed a greater fraction of time than SSR ($p < 0.001$, paired t-test, n=15 sessions; SSR: 22.8 ± 3% time removed, NSR: 33.4 ± 4 % removed; Figure 3.S7A). Thus, slip-associated spikes make a dominant contribution to increased firing on rough surfaces during the behaviorally relevant time window for texture discrimination.

To test whether Rough and Smooth trials can be accurately decoded on a single-trial basis from S1 activity, we built a population decoder based on a logistic GLM. For each recording session, we trained a logistic GLM (10-fold cross-validation, see: Experimental Procedures) to predict Rough vs. Smooth stimuli using the mean firing rate of each simultaneously recorded unit as weighted predictors (single unit population, Figure 3.7G, Top). In a second version of the decoder, we predicted Rough vs. Smooth from the summed spiking of all units (multi-unit, Figure 3.7G, Bottom; n=15 sessions, 5 mice). Each model was used to classify Rough vs. Smooth trials from single-trial spike

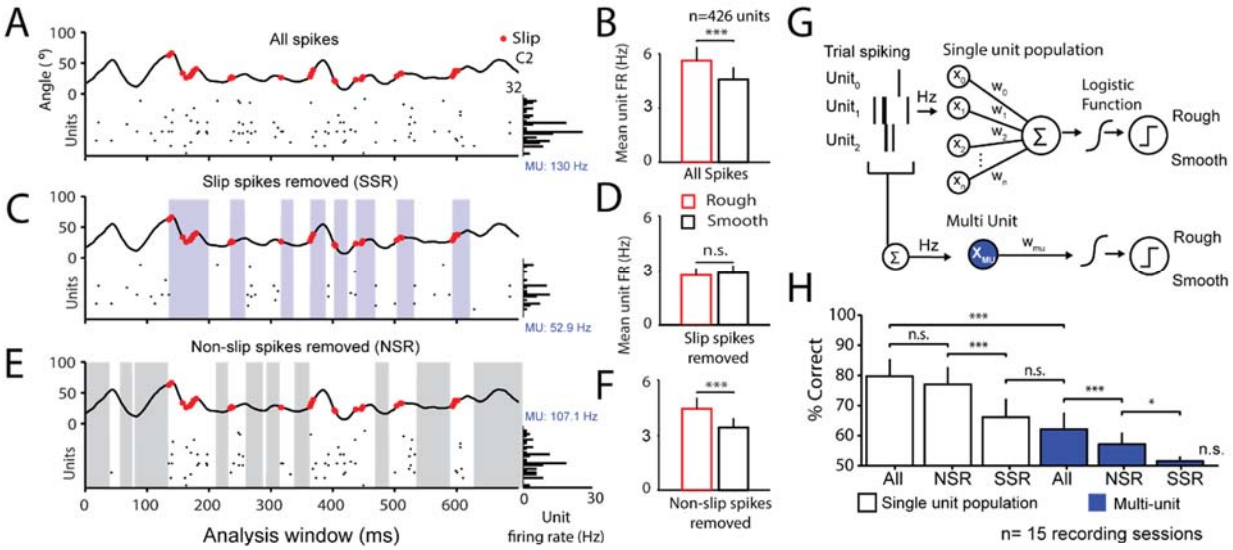

Figure 3.7. Decoding Rough vs. Smooth stimuli from spike rates. (A) Top: C2 whisker angle during 8 mm Rough stimulus trial; red dots are slips. Bottom: raster for 32 units recorded on this trial. Right: bar plot of each unit's mean firing rate within 700ms window. (B) Mean firing rate per unit on Rough trials (red) and Smooth trials (black). Error bars who CI_{95} (*** $p<0.001$; z-test of unit rate, Rough z-scored to Smooth; n=426 units). (C) Same trial as in (A) but with slip spikes removed (SSR) from 20ms windows after slips (purple). (D) Mean firing rate per unit on Rough and Smooth trials as in (B) but with SSR (n.s. = $p > 0.05$, analyzed as (B)). (E) Same trial as (A) but with non-slip spikes removed (NSR) from an equal number of 20ms windows containing no slips (grey). (F) Mean firing rate per unit on Rough and Smooth trials with NSR (*** $p < 0.001$, analyzed as in B). (G) Top: Single unit population decoding. Schematic of decoding model weighting mean firing rate from each unit to predict Rough and Smooth trials. Bottom: schematic of multi-unit decoding model. (H) Single trial accuracy of model classification on 10-fold hold-out trials using all spikes (All), NSR or SR, for single unit population decoding (white) and multi-unit decoding (black; n.s. = $p > 0.05$, ** $p<0.01$, *** $p<0.001$, paired t-test on model accuracy per recording session, n=15 recording sessions in 5 mice; bars indicate mean + CI95, Dunn-Šidák correction for multiple comparisons).

trains containing all spikes (All; Figure 3.7H). The single unit population model using all spikes correctly classified 81.0 ± 5.5 % of Rough and Smooth hold-out trials (Figure 3.7H, white), very similar to the discrimination accuracy of all mice on all sessions (78 ± 4%, n=7 mice, Figure 3.2D). Model performance was actually more accurate than mice on the behavioral sessions in which these neural data were obtained (mouse accuracy: 70.8 ± 3.3%, n= 13 sessions, 5 mice). This was because mouse performance dropped slightly during neural recording sessions compared to all behavioral sessions. The single unit population model substantially out-performed the multi-unit model (62.6 ± 5.8 % correct) using all spikes ($p < 0.001$, paired t-test on model accuracy per recording session, n= 15 sessions; Figure 3.7H, blue), indicating that weighting of separate units improves Smooth vs. Rough decoding. The model weights for units were higher in L5B units than L4 units ($p = 0.026$, Kruskal-Wallis and post-hoc test; n= 426 units, Dunn–Šidák correction for MC; Figure 3.S7B). In addition, model weights were significantly higher in RS units than FS units ($p = 0.017$, Wilcoxon Rank Sum; n= 426 units; Figure 3.S7C). Thus, while slips were coded strongly by FS units and L4 spiking (Figure 3.6C), Rough vs. Smooth decoding relied more strongly on RS units and subgranular spiking.

We next examined whether slip spikes contribute to correctly decoding Rough vs. Smooth trials. In order to make this comparison, we used the logistic GLMs trained with all spikes, but presented trials with slip spikes and non-slip spikes removed (SSR and NSR, Figure 3.7H). Removing non-slip spikes, the single unit population model classified Rough vs. Smooth with the same accuracy as using all spikes (NSR: 77.1 ±5.8 % correct, Figure 3.7H, white). By contrast, removing slip-associated spikes decreased accuracy by 11% (SSR: 66.1 ±6.3 % correct, Figure 3.7F, white). Using the multi-unit model, classification performance degraded with both NSR and SSR trials (NSR: 57.1 ±3.9 %; SSR: 51.4 ±1.7 %; Figure 3.7F, blue), and the multi-unit model

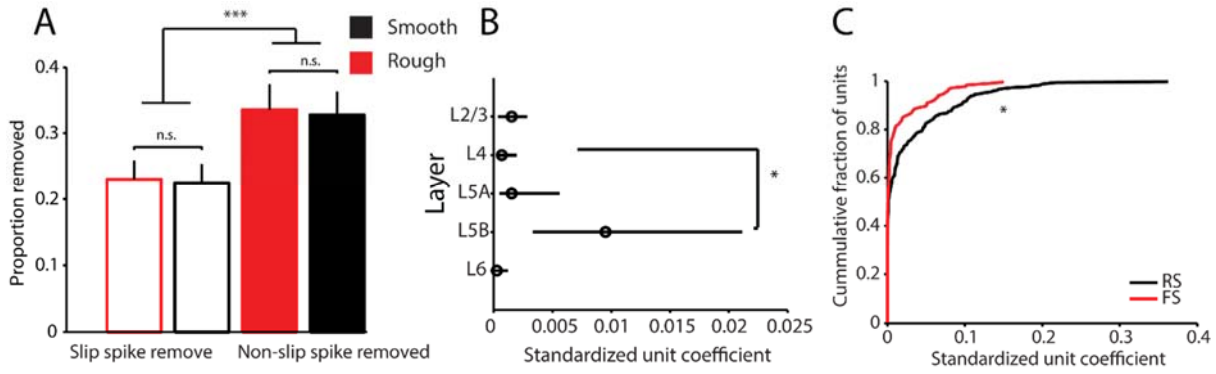

Supplemental Figure 3.7. Rough vs. Smooth model properties. (A) Proportion of palpation window removed for slip spike removal (no fill) and non-slip spikes removed (fill) for Smooth (black) and Rough (red) trials (n= 15 sessions, paired t-test). Bars are mean ± CI_{95} (B) Median ± bootstrapped CI_{95} GLM coefficient per layer in All Spike models (n=426 units, Kruskal Wallis with post-hoc test) (C) Cumulative fraction of RS and FS units vs. GLM coefficient (Wilcoxin Rank Sum test). n.s. = not significant, * $p < 0.05$, *** $p< 0.001$. Dunn–Šidák correction for M.C.

could not predict Smooth vs. Rough trials above chance level (50%) with slip-spikes removed (p=0.08, one tailed t-test, n=15 sessions). Together, these results suggest that individual units make independent contributions to decoding texture, which is not surprising given the diversity of unit responses we observed to Rough trials (Figure 3.5D-F). Furthermore, slip-evoked spikes accounted for a large proportion of discrimination accuracy.

Discrimination between rough surfaces

S1 represents precise features of tactile stimuli, even when the animal does not use that information for behavioral performance (Hernández et al., 2000; de Lafuente and Romo, 2005; McGuire et al., 2016). We asked whether S1 neurons discriminate between Rough surfaces, even though mice were not trained to discriminate these stimuli. S1 can be selective for sandpaper textures (Garion et al., 2014), but whether spatial frequency tuning exists is unknown. We analyzed the selectivity of each unit among Rough stimuli (10, 8, 4, 2 mm gratings, and Coarse sandpaper). 18.3% of units (78 / 426) were identified as selective using a one-way ANOVA ($p < 0.05$) on mean firing rate within the palpation window. Two stimulus selective RS units are shown in Figure 3.8A. Different units showed different spatial frequency tuning among rough stimuli (Figure 3.8B-C). 49% (38/78 units) responded maximally to one of the 4 grating stimuli, and 37% (29/78 units) responded maximally to the Coarse sandpaper (Figure 3.8C, example U2 in Figure 3.8A-B). In addition, 14% of units (11/78) were identified as spatial frequency selective, but also responded strongly to Smooth or Air (Figure 3.8C, example U4 in Figure 3.8B). Selective units were distributed across cortical layers similarly to roughness responsive units (Figure 3.5F), with most selective units occurring in subgranular layers (60.3%, 47/78). The vast majority of selective units were RS units (78%, 61/78, Figure 3.8D).

The existence of selective units suggest that the identity of a rough stimulus can be decoded from firing rate of the S1 unit population. We fit a multinomial GLM (glmnet, 4-fold cross-validation) to predict stimulus identity (Air, Smooth, 10mm, 8mm, 4mm, 2mm, and Coarse) from unit firing rate. Because no single recording session captured the full diversity of spatial tuning curves, we combined all units into one pseudo-population (n=396 units, 4 mice). The model was fit using 200 trials generated by bootstrapping unit firing rates (from the measured data ~28 trials/ stimulus). The resulting classifier decoded stimulus identity well above chance (cross-validation performance shown in Figure 3.8E, left) Chance performance is 14.3%, based on random choice of 7 stimuli. The model performed best at classifying Air (100% correct), Smooth, (97.6% correct), and the Coarse sandpaper (71.3% correct). Individual grating stimuli were distinguished well above chance (55.5% ± 9% mean accuracy across the 4 gratings). Fitting a similar multinomial model using C1 and C2 whisker slip rate and amplitude as predictors classified Air (82.5%), Smooth (39%) and Coarse (52%) trials above chance, but failed to distinguish between gratings (16.9 ± 2.7% mean accuracy across 4 gratings; p=0.054, one-tailed t-test of model performance against chance). Thus, discrimination of gratings in S1 spiking is not directly attributable to mean slip

activity in the palpation window, but instead likely reflects tuning generated within cortical circuits.

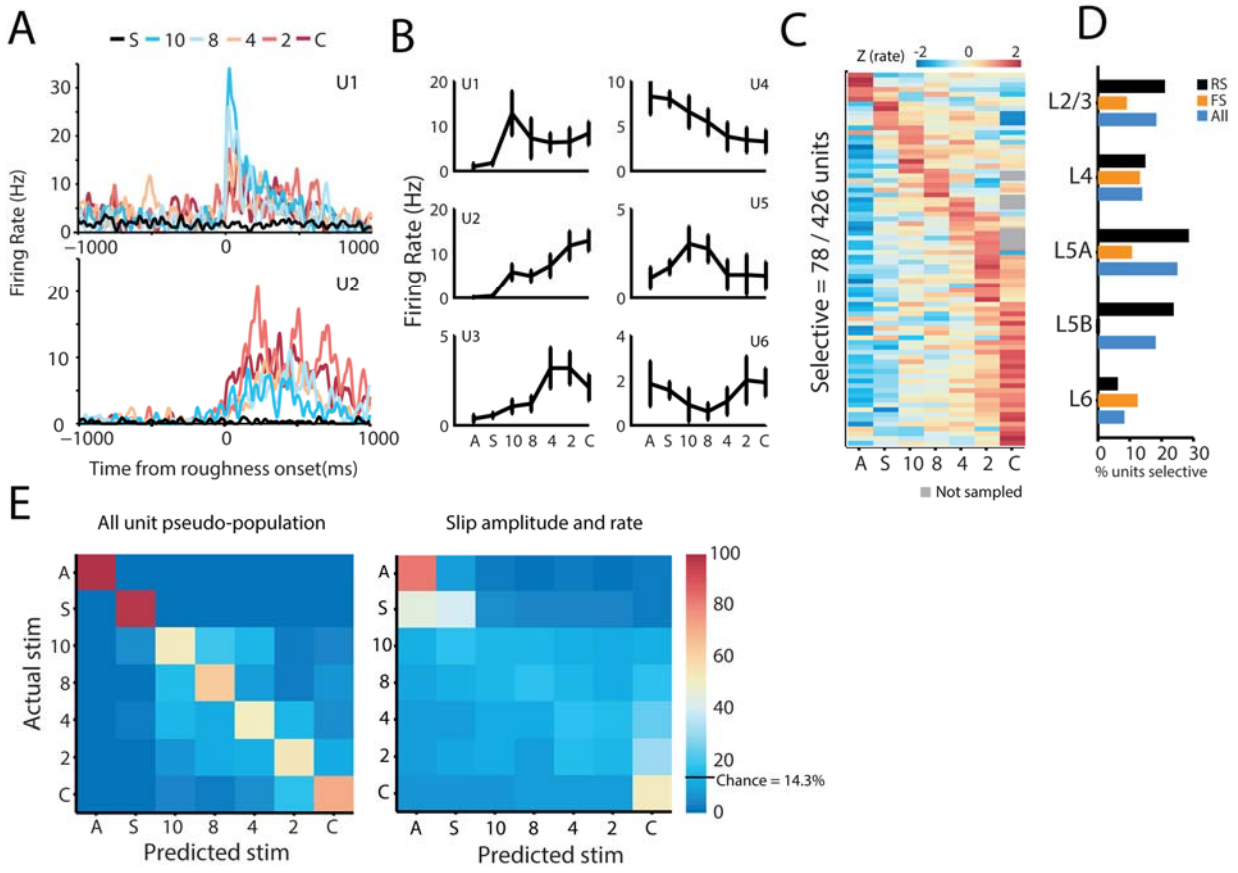

Figure 3.8. Discrimination between Rough stimuli in S1. (A) Two example L5A RS units identified as selective among Rough stimuli. PSTHs are aligned to first contact of ridge or sandpaper (Figure 3.5D) for 10mm to 2mm spatial periods (10, 8, 4, 2), coarse P150 sandpaper ("C") stimulus trials, and Smooth ("S"; aligned to equivalent stimulus position). (B) Spatial frequency tuning curves for 6 selective units (U1, U2 from (A); mean ± CI95). Responses to air catch trials ("A") also shown. (C) Mean z-scored firing rate for all stimuli for all selective units (n=78 / 426 units), sorted by maximum stimulus-evoked firing rate. (D) Percentage of RS, FS and All units in each layer that were stimulus selective. (E) Performance of neural population decoder to identify specific stimuli, shown as confusion matrices. Left: decoder based on firing rate, which showed strong discrimination even between different gratings. Right: decoder based on slip rate and amplitude, which showed poorer performance overall, and could not discriminate between gratings.

3.4 Discussion

In this study, we show for the first time that head-fixed mice can discriminate textures in a closed-loop stimulus paradigm. By performing high-speed whisker tracking during this behavior, we showed that stick-slips provided sufficient information to predict rough vs. smooth trials, and that these micromotions made a significant contribution to the mean firing rate difference between rough and smooth trials in S1. S1 neurons coded several largely overlapping features of touch, with neurons uniformly increasing response to touch, but responding more heterogeneously to roughness. We showed that this heterogeneity could be leveraged by individually weighting firing rates of single units in order to decode rough vs. smooth trials. At the same time, we showed that slips occur in a spatially inhomogeneous manner, locking to ridges with high spatial precision. Spikes also accumulated spatially at ridges. Interestingly, 20% of units showed selectivity within rough stimuli, with many subgranular RS units showing tuning for specific spatial frequencies. Taken as a whole, our observations offer evidence for a simultaneous representation of microscopic and macroscopic features of surfaces. This could provide sufficient information for more complex stimulus representations of shape.

Closed-loop texture presentation

The need for naturalistic head-fixed rodent behavioral paradigms has been widely acknowledged (Carandini and Churchland, 2013). Closed-loop approaches provide a useful compromise between the naturalistic stimulus exploration inherent to freely moving animals, and the strict stimulus control necessary to make accurate neurophysiological measurements. In addition, there is growing evidence that mouse locomotion facilitates primary cortical sensory responses via VIP -> SOM mediated disinhibition (Ayaz et al., 2013; Fu et al., 2014; Saleem et al., 2013) and that mouse locomotion may be broadly indicative of a more attentive, information gathering state (Niell and Stryker, 2010). Finally, whisking in mice is highly correlated with locomotion (Sofroniew et al., 2014). Therefore, the use of locomotion in closed-loop with stimulus delivery ensures an attentive, active whisking state and a receptive (disinhibited) primary sensory cortical state, ideal for measuring whisker S1 responses.

In the present study, closed-loop presentation also provided a means for self-initiated trials (reduced lapse rate, not shown) and naturalistic stimulus presentation dynamics (Figure 3.1C). At the same time, we exercised strict control over key aspects of stimulus geometry, such as the distance of the stimulus cylinder from the mystacial pad. This control was key for reconstructing the location of slips and spikes along different surfaces (Figure 3.3, 6). Notably, the 1D virtual track implemented in the present study is analogous to the active touch paradigm used in primate studies of texture coding, where hand movements are often restricted to a plane above grooved grating stimuli (Sinclair and Burton, 1991). Previous work using closed-loop stimulus delivery in the whisker system has revealed that S1 plays a key role in thigmotactic (wall-following) behavior (Sofroniew et al., 2014, 2015). In these studies, mice instinctively responded to open-loop distortions in wall distance by making corrective closed-loop running movements. Of note, mice picked a wall distance similar to the

distance used in the present study (~1.4cm) (Sofroniew et al., 2014). Building on this work, we have shown that mice can additionally discriminate rough from smooth textures in a wall-following paradigm.

Slips encode roughness and local spatial features

In the present study, we show for the first time that slips are sufficient to predict surface roughness with accuracy approaching mouse discrimination performance (Figure 3.2D). This moves the slip hypothesis beyond correlational observations (Arabzadeh et al., 2005; Jadhav et al., 2009; Wolfe et al., 2008) and shows that sufficient information is available in slip rate and amplitude during active whisking to discriminate individual rough and smooth trials. While recent studies indicate that neural responses in the periphery are better described by mechanical forces at the follicle than whisker kinematics (Bush et al., 2016), the two are highly correlated. The term “slip” is not meant to replace the underlying mechanical forces at play. Instead, slips are still best thought of as “kinetic signatures” (Arabzadeh et al., 2005), in that they provide a spatially and temporally precise signature for complex mechanical force transduction at the whisker follicle. In the last decade, evidence has continued to grow for the importance of slips in encoding roughness, both in the whisker system and in primates (Schwarz, 2016). The present study provides further evidence that slips accurately capture roughness information in naturally whisking mice discriminating smooth vs. rough textures.

The possibility that slips also contain spatial information has not been thoroughly explored (Schwarz, 2016). Stereotyped changes in whisker velocity across artificial whisking trials has led some to hypothesize that whisker kinematics represent underlying variability in spatial features (Arabzadeh et al., 2005). Until now, the relationship between whisker kinematics and local spatial features in actively whisking rodents had not been measured. Two large reasons for this are the difficulty in locating whisker contacts during naturalistic exploration, and the common use of sandpaper in tactile tasks, where local spatial features are heterogeneously arranged and confounded by changes in particle size and glue type. By combining high-speed whisker tracking in a global coordinate system and stimuli with known spatial period, we observed whisker micromotions locked to local spatial features during naturalistic whisking (Figure 3.3). In particular, we showed that slips accumulated along ridge onsets, providing a potential mechanism to decode surface shape as well as the location of features along surfaces. Recent work suggests rodents may have access to spatial frequency information (Georgieva et al., 2014), and there is no ambiguity that rodents can perform precise spatial discriminations (Knutsen et al., 2006; Mehta et al., 2007). Therefore, future study is necessary to elucidate the degree to which spatial frequency information is psychophysically available to rodents while palpating local shape.

Slips contribute spikes to S1 codes for roughness

We found that a substantial fraction of units (40%) coded for slip micromotions. In addition, many slip-coding neurons responded to roughness. While the correlation between slip-spikes and texture roughness has been observed previously (von

Heimendahl et al., 2007; Jadhav et al., 2009), the perceptual importance of these spikes has not been measured in discriminating rodents. In the present study, we showed that the firing rate of individually weighted neurons in small populations was sufficient to decode surface roughness with accuracy approaching mouse performance (Figure 3.7). By removing spikes in small windows relative to slips, we also showed that over 10% of rough vs. smooth discrimination accuracy relied on slip-evoked spikes. While neural populations have been decoded to predict texture previously (Chen et al., 2015),to our knowledge this is the first time neural decoding of texture has been shown to crucially depend on specific whisker kinematics.

It is important to note that our model did not attempt to differentially interpret RS and FS slip associated spikes: we treated both equally as sources of slip- and texture-related information. FS responses were not excluded because we found that slips were encoded by 70% of FS units, a distinction that was not measured in previous studies (Jadhav et al., 2009). The simplest reason for the high proportion of FS slip-responsiveness may be that FS neurons receive broad excitatory input from surrounding and feed-forward RS units (Scholl et al., 2015). In this model, inhibitory interneurons average over many local excitatory slip responses to offer a cleaner signal for slip coding than individual, sparsely responding excitatory neurons. The high level of FS slip responses may also play a role in increasing the dynamic range of cortical responses during persistent surface contact, a possibility which we discuss in more detail below.

Neurons show temporal space code, spatial frequency tuning

Like slips, S1 spikes accumulated along surfaces at grating ridge onsets (Figure 3.6H). The spike densities observed here are reminiscent of the canonical scanned letter rasters measured in primate Area 3b (Phillips et al., 1988). As in those studies, the spatial spike density plots of the present study are rendered purely in space. If instead we presented convolved estimates of spike rate in space, we would show only modest rate changes at bar edges (not shown). The reason for this was that spikes primarily occurred during slip events at ridges (Figure 3.3, 4), but following ridge contact, the whisker would often linger momentarily without further acceleration change. This pattern of whisker slipping and pausing would effectively average out the initial slip-induced increase in firing rate with respect to whisker position. Thus, Figure 3.6H presents unit spiking accumulated in time for a code of space.

Acquiring spatial information sequentially over several whisks (Figure 3.3,6H) represents temporal encoding of spatial information (Ahissar and Arieli, 2001). This is fundamentally different than a labeled-line spatial code arising instantaneously by simultaneously deflecting many whiskers (Ahissar and Arieli, 2001; Anjum et al., 2006). The duplex theory of texture (Katz, 1989) proposes coarse textures are transduced spatially across the skin surface while fine textures are encoded by temporal responses to skin vibration. The spatial coding described in the duplex theory refers to labeled-line spatial coding, and thus does not make predictions regarding temporal coding of spatial features. However, rapid exploratory movements in the whisker system (20Hz) seem likely to accumulate spatially discrete features sequentially in time, with spatial information recovered using a parallel temporal code of sensor position. The requisite

components of a temporal position code have been identified in whisker primary motor and somatosensory cortices (Kleinfeld and Deschênes, 2011). Thus, a temporal spatial code is a particularly plausible model for interpreting local feature encoding in the whisker system.

Interestingly, we also found evidence for spatial frequency tuning in S1 (Figure 3.8). While texture selective neurons have been observed in L2/3 (Garion et al., 2014), to our knowledge this is the first time spatial tuning has been observed in whisker S1. Furthermore, we showed that this selectivity was sufficiently informative to decode grating stimulus period from population firing rate, even though mice were not trained to perform that task.

Simultaneous coding of touch, roughness and local features

Neurons in L4 code whisker contact with high temporal precision and minimal noise (Hires et al., 2015), but whether these inputs are further processed across cortical layers to achieve new sensory representations remains unclear. By comparing firing rate changes to touch, roughness, and slips within the same neurons, we found that all three features were coded in a highly-overlapping population of responsive neurons (Figure 3.6G). This did not simply reflect a hierarchy of touch sensitivity: neurons that increased firing to touch did not necessarily increase further to the onset of a rough surface (Figure 3.5G), as would be expected from increased mechanical forces exerted during rough contact. Instead, we observed that while touch strongly and uniformly increased firing in the majority of neurons, roughness was commonly coded by both increases and decreases in firing rate, particularly in subgranular RS neurons (Figure 3.5F). This may reflect a preservation of dynamic range (Pouille et al., 2009) via feed-forward inhibition, including a recently observed L4->L5 inhibitory pathway (Pluta et al., 2015).

As mentioned above, FS slip-responsive neurons may be the source of this feedforward inhibition. We observed strong slip-evoked FS responses distributed across layers (Figure 3.6C) which overlapped with the laminar distribution of RS neurons that decreased in response to roughness (Figure 3.5F). Thus, decreased RS roughness responses may be a result of slip-mediated FS-to-RS inhibition in a subset of touch-excited RS units. In this model, S1 responds strongly to columnar whisker touch with firing rate increases, but dynamic range is preserved in a subset of RS units via slip-mediated inhibition. This could allow a subset of touch-excited RS units to avoid saturation and maintain texture response variability by decreasing firing rate. Indeed, individual unit response variability was crucial for decoding Rough vs. Smooth surfaces in the present study: when we averaged neural response variability across units in a multi-unit decoder, discrimination performance dropped significantly (Figure 3.7H).

Finally, we observed that RS slip responses were most prevalent in L4 (Figure 3.6B) while RS roughness and spatial frequency selectivity were most prevalent outside of L4 (L2/3, L5-L6). This may represent a fundamental transformation from local feature coding in L4 to an integrated representation of these features in extragranular layers. Other studies have suggested that subgranular layers are fundamentally more integrative in S1 (Chapin, 1986; Ghazanfar and Nicolelis, 1999; Manns et al., 2004). However, unlike the highly selective receptive field transformations observed in V1, the

neurons measured in this study showed highly overlapping feature responsiveness (Figure 3.6G). One clear benefit of this coding scheme is an exquisite sensitivity to whisker touch. In the present study, touch responses were low-adapting and robust during persistent surface contact (Figure 3.5B), which allowed for perfect (100%) neural population decoding accuracy of Air vs. Surface contacting trials (Figure 3.8E). In light of these observations, a picture emerges where S1 is primarily engaged by whisker touch (Yu et al., 2016), and subsequently refined to allow feature selectivity that arises in parallel with touch responses.

Simultaneous codes for touch and local tactile features could explain why reverse correlation historically extracts somewhat limited spatiotemporal kinematic filters (Estebanez et al., 2012; Maravall et al., 2007; Ramirez et al., 2014): these methods apply white noise whisker vibrations without first simulating the mechanical forces of whisker touch at the follicle. This might be equivalent to displaying visual noise with uncontrolled and spuriously correlated variations in luminance. Future studies could explore a more naturalistic stimulus space by performing kinematic reverse correlations that also introduce systematic variation to the baseline follicle tone.

Conclusion

We measured stick-slips and cortical spiking responses in mice trained to discriminate rough and smooth surfaces. Slips and spikes accumulated along local spatial features such as ridges and predicted rough surfaces on a single-trial basis. An overlapping set of neurons responded to touch, roughness and slips, with 20% of neurons showing selectivity for specific rough stimuli. Furthermore, we showed for the first time that slip-evoked spikes significantly contributed to a population rate code for roughness. Thus, neurons in S1 simultaneously responded to microscopic features like slips and ridges with temporally coded spikes, while generating rate codes for macroscopic features like touch, roughness, and spatial period.

3.5 Experimental Procedures

Surgical procedures

Head-plate implant: mice >P40 were anesthetized using 2% isoflurane (vol/vol) and placed in a stereotaxic apparatus. Body temperature was maintained at 37 °C using a feedback-controlled heating pad (FHC, 40-90-8D) and a small incision was made in the scalp. The skull was cleaned and a stainless steel head plate was implanted using dental cement (Metabond, Parkell), aligned to bregma and midline (Figure 3.S1A). Mice recovered for at least 1 week before training. After training, a second procedure was performed under Isoflurane (1.5%) + chlorprothixene (0.025 mg/kg) to localize C1-C3 whisker column locations through intact skull using intrinsic signal optical imaging (ISOI) as by Drew & Feldman, 2008. Afterwards the cranial chamber was filled with silicone elastomer (Kwik-Cast, WPI), sealed with a thin layer of dental cement and C1-C2

whisker follicle locations were measured in stereotactic coordinates from bregma (Figure 3.S1B), adjusted for rest vs. active set position (~1mm rostral, measured via high-speed imaging).

In vivo electrophysiology: mice were briefly anesthetized with 2% isoflurane, a small craniotomy (~ 0.1mm) was made over ISOI identified C1 or C2 column. Recording locations were measured in a coordinate system relative to vascular landmarks for later reconstruction, and the silicon probe was slowly inserted to desired depth (500-900μm; Sutter MP285). The chamber was then resealed and the probe was allowed to settle (45 minutes). After recording, the probe was removed and the chamber was resealed with silicone and dental cement.

Histology

After final recording, 3 fluorescent tracks were created relative to landmarks using a silicone probe covered in 1,1'-Dioctadecyl-3,3,3',3'-Tetramethylindo-carbocyanine Perchlorate (DiI, D282, ThermoFisher), mice were deeply anesthetized with isoflurane and killed, the brain was removed and fixed in 4% paraformaldehyde, flattened, tangentially sectioned (50μm) and stained for cytochrome oxidase (CO) to identify whisker barrels in L4. Fluorescent tracks were imaged relative to barrel boundaries to reconstruct experimental penetration locations.

Current source density

Slip-evoked local field potentials (LFPs; Butterworth filter 0.1-300 Hz; MATLAB) were cleared of electrical artifacts (>15 s.d. above mean), normalized to account for differences in channel impedance, and interpolated between channels (25um site spacing, 10-20x interpolation) before calculating the second spatial derivative (Freeman and Nicholson, 1975). CSDs were convolved with a 2D Gaussian and zero-crossings encountered between the most negative current sink (putative L4) and the next current source (putative L5A) was deemed the L4/L5A boundary (search restricted to sites estimated to lie 400-650um below pia as measured via micromanipulator). Units were then assigned to layers using layer boundaries as in (Lefort et al., 2009).

Spike sorting

A 32ch TDT System 3 (RZ5) was used to digitize running/motor movement signals (48kHz) and neural signals (24.4 kHz) recorded from 16 channel (A1x16-5mm-25-177-A16) or 32 channel (A1x32-5mm-25-177-A32, Neuronexus) linear probes for post hoc filtering. Channels used for spike processing (Bessel filter 300-6,000 Hz; MATLAB filtfilt()) were further processed by common average referencing (Ludwig et al., 2009). All spike detection, clustering and sorting was performed using UltraMegaSort 2000. Linear probe electrode sites were broken into groups of 4-adjacent sites (tetrodes) and spike events were detected 3-4 s.d. below the mean with a 0.75 ms shadow period. Events were then clustered using k-means clustering (kmeans_clustersize =50), aggregated based on interface energy (agg_cutoff = 0.2; Fee et al., 1996) and manually inspected on the basis of spike waveform, stability in time, and inter-spike interval

refractory period violations (< 0.5% of intervals < 1.5ms). Units were classified as fast-spiking if trough to peak duration was below 0.45ms (Barthó et al., 2004).

Smooth vs. Rough discrimination training

Mice (n=8) were water restricted to 85% ad lib weight and handled for 5-10 minutes for 2 days before training. Animals were acclimated to head-fixation (1-2 days) and taught to lick for water rewards (1-2 days; 2-5µl rewards paired with a 30ms 2.8kHz tone). Early training used 50:50 Rough:Smooth trials in block delivery (5±1 trials) with open-loop (fixed velocity) stimulus presentation. Initially, Rough stimuli were paired with automatic reward (1-2 days) followed by lick-triggered reward. Early training ended when mice performed with 5-10 correct transitions from Go to No-go blocks paired with overall session accuracy > 70% for two consecutive days. Rough and Smooth stimuli were then presented randomly (open-loop) until criterion (2 consecutive days of > 75% performance). Animals then transitioned from open-loop presentation to closed-loop presentation (1-4 days). Upon stable performance, rows of right-side whiskers were trimmed over 5 days until all but C1-C2 remained. If performance decreased, whisker trimming was paused until behavior recovered. Trials were prevented from starting until mice withheld licking for 2-3 seconds. Response windows started with stimulus movement (open-loop) or after running 1-2cm (closed-loop) and lasted for 1-2 seconds. False Alarms triggered a 300ms 10kHz tone and a 5 second time out, while no action was taken for Correct Rejections or Misses. Catch trials (~5% of trials; 50:50 Go:No-go) were identical to stimulus trials except the stimulus cylinder did not make contact with the whiskers. They were used to measure active whisking in Air and to test for the use of non-tactile cues. Two mice were excluded during early training due to suspected cheating and one mouse was excluded for failure to advance from early training after 26 training sessions (8/11 mice learned full task).

Behavioral analysis

In order to identify the start and stop of attentive mouse behavior in a training session, we calculated d' using a sliding window of 50 trials centered on each trial (Siegle et al., 2014), where

$$d' = z(hit) - z(fa)$$

hit = hit rate, *fa* = false alarm rate, and z= inverse of the normal cumulative distribution function, with mean = 0 and standard deviation = 1. We applied the log-linear correction for rate values of 0 and 1 (Stanislaw and Todorov, 1999). Discrimination accuracy was calculated from the first trial with a sliding d' > 1 to the last trial with a sliding d' >1. This method identified 66,906/78,713 trials (85%) for use in behavioral analysis. All mouse discrimination metrics (percent lick, d', % correct) were calculated from these trials. Neural data were analyzed from all available trials.

Rough and Smooth stimuli

Rough stimuli consisted of gratings with 2, 4, 8, and 10mm spatial period and one section of coarse (P150) sandpaper matched in height (0.8mm from surface). Spatial period defines one grating cycle i.e. 2mm = 1mm bar, 1mm gap. Gratings were

constructed from ±0.05 mm precision strips of 0.03” shim plastic (P/N: 9513K75, McMaster-Carr) glued (ZAP, PAAPT02) in 30mm patches to an acetate plastic sheet (3M, PP2950) attached to an acrylic wheel (OD: 12.64cm acrylic tube, 1/8” wall, TAP Plastics). The Smooth surface consisted of acetate plastic alone. Glue was also applied above and below Smooth sections to control for the presence of glue odor and all stimuli were wiped cleaned with odorless, water-based detergent (Process NPD) before every training session.

Closed-loop stimulus delivery

The stimulus cylinder was rotated with a stepper motor using 20,000 step/rotation micro-stepping (STM17R, Applied Motion). To control for stepper motor sounds, we used a stimulus randomization paradigm that took the same number of steps to reach any position on the stimulus cylinder. In addition, we mounted a sham stepper motor next to the stimulus motor which presented randomly chosen stimuli during each trial (and see “Catch trials” above). Stimulus cylinder motors were controlled by independent Arduino Uno R3’s using custom code. Real-time closed-loop stimulus delivery was achieved by switching stepper motor rotation control to pulses generated by the running disk rotary encoder (P/N: H5-1000-IE-S, US Digital). The running disk consisted of a 6” diameter disk machined from 1/16” thick acrylic (P/N: 8560K172, McMaster-Carr) with a polypropylene mesh adhered for traction (mesh P/N: 9265T51, McMaster-Carr).

Linear stimulus onset

The stimulus cylinder stepper motor was mounted to a linear actuator (P/N: LP28 with NEMA11 motor, Parker Automation; Nippon Pulse AD1431 motor driver, 16x μsteps, 3,211 steps/cm) at an angle of 52˚ from midline. Touch onset occurred while the stimulus assembly moved towards the mystacial pad at a velocity of 3.1cm/s. The linear onset had an S-curve velocity profile (max acceleration = 12 cm/s2 in 150ms onset/offset acceleration trapezoids; example trajectory in Figure 3.5A). When in position for stimulus delivery, the stimulus cylinder was 1.45 ± 0.05cm from the mystacial pad at its closest point (full contact). During stimulus randomization, the stimulus assembly was retracted to 2.94 ± 0.06 cm from the mystacial pad at its closest point (no contact).

Whisker Data Analysis

Identifying whisker position, slips

Whisker tracking was performed in n= 7 trained mice. Whiskers were imaged as 1D shadows in collimated IR light (904nm laser, P/N: L904P010, Thorlabs) at 4kHz using a custom linear CCD array as by Jadhav et al., 2009, 0.8-1cm from mystacial pad (Figure 3.S1C). Imaged pixels were spatially corrected for lens distortion and localized within a 2D plane in coordinates from mouse bregma using a calibrated webcam (C510, Logitech; MATLAB 2014b, Machine Vision Toolbox). This allowed whisker position to be calculated as angular coordinates from the follicle or absolute positions in space (mm along stimulus cylinder). Raw movies were pre-processed by subtracting median pixel

values. Whisker shadow peaks were detected and fit with a Gaussian curve to interpolate whisker position between pixels. Position noise was reduced by down-sampling to 1kHz (decimate( ), MATLAB) and up-sampling with a spline fit to the original sampling rate. Surface position estimates were corrected for bend by fitting a Gaussian model to projection errors measured in high-speed video analysis (Figure 3.S1). Acceleration was calculated numerically as the second derivative of position with respect to time (diff( ), MATLAB). Slips were detected as peaks in acceleration that exceeded ± 2.5 s.d. from the mean acceleration within each session (for each whisker), unless otherwise indicated.

Whisker Kinematics

Whisker imaging was used to identify a palpation window defined as 50ms before first contact with the stimulus patch in each trial, to 200ms before first lick. 650ms windows were used on no-lick trials. Mean slip rate, amplitude, whisker speed, and rodent speed were calculated in this window for each trial. These slip measurements were used to predict Rough vs. Smooth and Lick vs. No Lick trials (see: General Linear Model methods). Slip density was calculated by summing the number of slips per mm along the stimulus during each trial. Edge-triggered acceleration was calculated by z-scoring |acceleration| during the first two ridge crossings of each grating trial. We tested for differences in these means using a 2-way ANOVA with repeated measures with Rough and Smooth as factors; n=6 mice, 28 sessions, analyzed across time points ± 5ms from ridge crossing.

Neural Data Analysis

Neural data were analyzed in 5 trained mice. We calculated z-scored responses as:

$$z = \frac{x_{response} - x_{baseline}}{\sigma_{baseline}}$$

, where x = mean and σ = standard deviation across events (i.e. trials or kinematics). For z-scored PSTHs (zPSTH), time-series data were first averaged within the baseline period, and then $x_{baseline}$ and $\sigma_{baseline}$ were calculated as described above. These scalar values were used to z-score the $x_{response}$ PSTH time-series from each event.

The log-modulus transformation (Figure 3.5G) was implemented as:

$$lm = sign(\Delta x) * \log(|\Delta x| + 1)$$

, where $\Delta x = x_{response} - x_{baseline}$.

Touch and roughness responsiveness

We identified touch and roughness responsive units by performing a paired t-test on mean firing rate in 650ms windows before and after touch or roughness onset (Figure 3.5). Roughness onset was always relative to first C2 contact (Figure 3.5D). The mean sign of firing rate change was used to classify units as increasing or decreasing.

ZPSTHs from units classified as increasing, decreasing, or non-responsive were smoothed (MATLAB, 'lowess', 25ms) before calculating the mean and CI_{95} of all units.

Slip and ridge responsiveness
We measured slip responses in all units using columnar whisker slips ranging from 1 to 8 s.d. above baseline (Figure 3.6B). We found that slips ≥ 2.5 s.d. above baseline drove consistent responses in S1 (Figure 3.S6A). We identified slip responsive units by performing a paired t-test on mean firing rate 20ms after the peak acceleration of slips ≥ 2.5 s.d. compared to a 20ms baseline 40ms before the slip peak (Figure 3.6C). Ridge responses were measured in an identical way using ridge crossing events (Figure 3.6F). Slip response latency was measured using a binless poison method (Chase and Young, 2007), with median bootstrapped 95% confidence intervals. Spike jitter was measured in slip-responsive units as the full-width at half-max in the slip PSTH.

Rough stimulus selectivity
We identified selective units by calculating a one-way ANOVA on mean firing rates within the palpation window for each rough stimulus type (10, 8, 4, 2mm and Coarse). Tuning curves represent mean palpation window firing rate to each stimulus.

General linear models
Single trials were decoded using glmnet( ) in MATLAB (Qian et al., 2013) by fitting a multinomial GLM (glmnet( ), 'multinomial') and classifying hold-out data (glmnetPredict( ), 'class'). The alpha parameter was left at default, and lambda was calculated within each fold using cross-validation (CV, cvglmnet(), 10 folds). All classification accuracies represent mean model performance on hold-out data (k-fold implementation) across 25-50 iterations of randomly assigned folds. To eliminate bias, training and testing data were re-sampled to have identical numbers of trials within each response category. For whisker and neural decoding of Rough vs. Smooth trials, models were fit (10-fold CV) on trials within behavioral sessions and averaged for each mouse. To evaluate the contribution of slip spikes, models fit on palpation window firing rates using all spikes were then used to classify slip-spike-removed and non-slip-spike-removed firing rates. For discriminating between all stimuli (Air, Smooth, 10, 8, 4, 2mm, and Coarse), a pseudo-population was created by combining all units and bootstrapping 200 trials of palpation window firing rate responses. One recording did not contain all stimulus categories and was excluded from this analysis (n=4 mice).

3.7 Acknowledgements

We would like to thank Janice Chua, Karan Patel, Sierra Feasel, and Monet Lane for their help in mouse training and behavior analysis. B.R.I. was supported by National Science Foundation graduate fellowship (DGE 1106400).

3.6 References

Ahissar, E., and Arieli, A. (2001). Figuring Space by Time. Neuron *32*, 185–201.

Anjum, F., Turni, H., Mulder, P.G.H., van der Burg, J., and Brecht, M. (2006). Tactile guidance of prey capture in Etruscan shrews. Proc. Natl. Acad. Sci. U. S. A. *103*, 16544–16549.

Arabzadeh, E., Petersen, R.S., and Diamond, M.E. (2003). Encoding of whisker vibration by rat barrel cortex neurons: implications for texture discrimination. J. Neurosci. *23*, 9146–9154.

Arabzadeh, E., Zorzin, E., and Diamond, M.E. (2005). Neuronal encoding of texture in the whisker sensory pathway. PLoS Biol. *3*, e17.

Ayaz, A.A., Saleem, A.B., Schölvinck, M.L., and Carandini, M. (2013). Locomotion controls spatial integration in mouse visual cortex. Curr. Biol. *23*, 890–894.

Barthó, P., Hirase, H., Monconduit, L., Zugaro, M., Harris, K.D., and Buzsáki, G. (2004). Characterization of neocortical principal cells and interneurons by network interactions and extracellular features. J. Neurophysiol. *92*, 600–608.

Bush, N.E., Schroeder, C.L., Hobbs, J.A., Yang, A.E., Huet, L.A., Solla, S.A., and Hartmann, M.J. (2016). Decoupling kinematics and mechanics reveals coding properties of trigeminal ganglion neurons in the rat vibrissal system. Elife *5*, 1–23.

Carandini, M., and Churchland, A.K. (2013). Probing perceptual decisions in rodents. Nat. Neurosci. *16*, 824–831.

Chapin, J.K. (1986). Laminar differences in sizes, shapes, and response profiles of cutaneous receptive fields in the rat SI cortex. Exp. Brain Res. *62*, 549–559.

Chase, S.M., and Young, E.D. (2007). First-spike latency information in single neurons increases when referenced to population onset. Proc. Natl. Acad. Sci. U. S. A. *104*, 5175–5180.

Chen, J.L., Margolis, D.J., Stankov, A., Sumanovski, L.T., Schneider, B.L., and Helmchen, F. (2015). Pathway-specific reorganization of projection neurons in somatosensory cortex during learning. Nat. Neurosci. *18*, 1101–1108.

Chen, S., Augustine, G.J., and Chadderton, P. (2016). The cerebellum linearly encodes whisker position during voluntary movement. Elife *5*, 1–16.

Curtis, J.C., and Kleinfeld, D. (2009). Phase-to-rate transformations encode touch in cortical neurons of a scanning sensorimotor system. Nat. Neurosci. *12*, 492–501.

Diamond, M.E., Von Heimendahl, M., and Arabzadeh, E. (2008). Whisker-mediated texture discrimination. PLoS Biol. *6*, 1627–1630.

Drew, P.J., and Feldman, D.E. (2008). Intrinsic Signal Imaging of Deprivation- Induced Contraction of Whisker Representations in Rat Somatosensory Cortex. Cereb. Cortex.

Estebanez, L., Boustani, S. El, Destexhe, A., and Shulz, D.E. (2012). Correlated input reveals coexisting coding schemes in a sensory cortex. Nat. Neurosci. 1–11.

Fee, M.S., Mitra, P.P., and Kleinfeld, D. (1996). Automatic sorting of multiple unit neuronal

signals in the presence of anisotropic and non-Gaussian variability. J. Neurosci. Methods *69*, 175–188.

Freeman, J. a, and Nicholson, C. (1975). Experimental optimization of current source-density technique for anuran cerebellum. J. Neurophysiol. *38*, 369–382.

Fu, Y., Tucciarone, J.M., Espinosa, J.S., Sheng, N., Darcy, D.P., Nicoll, R. a, Huang, Z.J., and Stryker, M.P. (2014). A cortical circuit for gain control by behavioral state. Cell *156*, 1139–1152.

Garion, L., Dubin, U., Rubin, Y., Khateb, M., Schiller, Y., Azouz, R., and Schiller, J. (2014). Texture coarseness responsive neurons and their mapping in layer 2-3 of the rat barrel cortex in vivo. Elife *3*, e03405.

Georgieva, P., Brugger, D., and Schwarz, C. (2014). Are spatial frequency cues used for whisker-based active discrimination? Front. Behav. Neurosci. *8*, 379.

Gerdjikov, T. V., Bergner, C.G., Stüttgen, M.C., Waiblinger, C., and Schwarz, C. (2010). Discrimination of vibrotactile stimuli in the rat whisker system: behavior and neurometrics. Neuron *65*, 530–540.

Ghazanfar, A.A., and Nicolelis, M. a (1999). Spatiotemporal properties of layer V neurons of the rat primary somatosensory cortex. Cereb. Cortex *9*, 348–361.

von Heimendahl, M., Itskov, P.M., Arabzadeh, E., and Diamond, M.E. (2007). Neuronal activity in rat barrel cortex underlying texture discrimination. PLoS Biol. *5*, e305.

Hernández, a, Zainos, a, and Romo, R. (2000). Neuronal correlates of sensory discrimination in the somatosensory cortex. Proc. Natl. Acad. Sci. U. S. A. *97*, 6191–6196.

Hires, S.A., Gutnisky, D.A., Yu, J., O'Connor, D.H., and Svoboda, K. (2015). Low-noise encoding of active touch by layer 4 in the somatosensory cortex. Elife *4*, 1–18.

Hires, S.A. ndrew, Pammer, L., Svoboda, K., and Golomb, D. (2013). Tapered whiskers are required for active tactile sensation. Elife *2*, e01350.

Jadhav, S.P., and Feldman, D.E. (2010). Texture coding in the whisker system. Curr. Opin. Neurobiol. *20*, 313–318.

Jadhav, S.P., Wolfe, J., and Feldman, D.E. (2009). Sparse temporal coding of elementary tactile features during active whisker sensation. Nat. Neurosci. *12*, 792–800.

Katz, D. (1989). The World of Touch (translation). (Hillsdale, NJ: Erlbaum).

Kleinfeld, D., and Deschênes, M. (2011). Neuronal basis for object location in the vibrissa scanning sensorimotor system. Neuron *72*, 455–468.

Knutsen, P.M., Pietr, M., and Ahissar, E. (2006). Haptic object localization in the vibrissal system: behavior and performance. J. Neurosci. *26*, 8451–8464.

de Lafuente, V., and Romo, R. (2005). Neuronal correlates of subjective sensory experience. Nat. Neurosci. *8*, 1698–1703.

Lefort, S., Tomm, C., Floyd Sarria, J.-C.C., and Petersen, C.C.H. (2009). The excitatory neuronal network of the C2 barrel column in mouse primary somatosensory cortex. Neuron *61*, 301–316.

Ludwig, K.A., Miriani, R.M., Langhals, N.B., Joseph, M.D., Anderson, D.J., and Kipke, D.R. (2009). Using a common average reference to improve cortical neuron recordings from microelectrode arrays. J. Neurophysiol. *101*, 1679–1689.

Manns, I.D., Sakmann, B., and Brecht, M. (2004). Sub- and suprathreshold receptive field properties of pyramidal neurones in layers 5A and 5B of rat somatosensory barrel cortex. J. Physiol. *556*, 601–622.

Maravall, M., Petersen, R.S., Fairhall, A.L., Arabzadeh, E., and Diamond, M.E. (2007). Shifts in coding properties and maintenance of information transmission during adaptation in barrel cortex. PLoS Biol. *5*, 0323–0334.

McGuire, L.M., Telian, G., Laboy-Juárez, K.J., Miyashita, T., Lee, D.J., Smith, K.A., and Feldman, D.E. (2016). Short Time-Scale Sensory Coding in S1 during Discrimination of Whisker Vibrotactile Sequences. PLOS Biol. *14*, e1002549.

Mehta, S.B., Whitmer, D., Figueroa, R., Williams, B. a, and Kleinfeld, D. (2007). Active spatial perception in the vibrissa scanning sensorimotor system. PLoS Biol. *5*, e15.

Morita, T., Kang, H., Wolfe, J., Jadhav, S.P., and Feldman, D.E. (2011). Psychometric curve and behavioral strategies for whisker-based texture discrimination in rats. PLoS One *6*, e20437.

Niell, C.M., and Stryker, M.P. (2010). Modulation of visual responses by behavioral state in mouse visual cortex. Neuron *65*, 472–479.

O'Connor, D.H., Peron, S.P., Huber, D., Svoboda, K., Connor, D.H.O., Peron, S.P., Huber, D., Svoboda, K., O'Connor, D.H., Peron, S.P., et al. (2010). Neural activity in barrel cortex underlying vibrissa-based object localization in mice. Neuron *67*, 1048–1061.

Phillips, J.R., Johnson, K.O., and Hsiao, S.S. (1988). Spatial pattern representation and transformation in monkey somatosensory cortex. Proc. Natl. Acad. Sci. U. S. A. *85*, 1317–1321.

Pluta, S., Naka, A., Veit, J., Telian, G., Yao, L., Hakim, R., Taylor, D., and Adesnik, H. (2015). A direct translaminar inhibitory circuit tunes cortical output. Nat. Neurosci. *18*, 1631–1640.

Pouille, F., Marin-Burgin, A., Adesnik, H., Atallah, B. V., and Scanziani, M. (2009). Input normalization by global feedforward inhibition expands cortical dynamic range. Nat. Neurosci. *12*, 1577–1585.

Qian, J., Hastie, T., Friedman, J., Tibshirani, R., and Simon, N. (2013). Glmnet for Matlab.

Ramirez, A., Pnevmatikakis, E.A., Merel, J., Paninski, L., Miller, D., Bruno, R.M., Miller, K.D., Bruno, R.M., Miller, D., Bruno, R.M., et al. (2014). Spatiotemporal receptive fields of barrel cortex revealed by reverse correlation of synaptic input. Nat Neurosci *advance on*.

Ritt, J.T., Andermann, M.L., and Moore, C.I. (2008). Embodied information processing: vibrissa mechanics and texture features shape micromotions in actively sensing rats. Neuron *57*, 599–613.

Saleem, A.B., Ayaz, A., Jeffery, K.J., Harris, K.D., and Carandini, M. (2013). Integration of visual motion and locomotion in mouse visual cortex. Nat. Neurosci.

Scholl, B., Pattadkal, J.J., Dilly, G.A., Priebe, N.J., and Zemelman, B. V. (2015). Local Integration Accounts for Weak Selectivity of Mouse Neocortical Parvalbumin Interneurons.

Neuron *87*, 424–437.

Schwarz, C. (2016). The Slip Hypothesis: Tactile Perception and its Neuronal Bases. Trends Neurosci. *39*, 449–462.

Siegle, J.H., Pritchett, D.L., and Moore, C.I. (2014). Gamma-range synchronization of fast-spiking interneurons can enhance detection of tactile stimuli. Nat. Neurosci. *17*, 1371–1379.

Sinclair, R.J., and Burton, H. (1991). Neuronal activity in the primary somatosensory cortex in monkeys (Macaca mulatta) during active touch of textured surface gratings: responses to groove width, applied force, and velocity of motion. J. Neurophysiol. *66*, 153–169.

Sofroniew, N.J., Cohen, J.D., Lee, a. K., and Svoboda, K. (2014). Natural Whisker-Guided Behavior by Head-Fixed Mice in Tactile Virtual Reality. J. Neurosci. *34*, 9537–9550.

Sofroniew, N.J., Vlasov, Y. a, Andrew Hires, S., Freeman, J., and Svoboda, K. (2015). Neural coding in barrel cortex during whisker-guided locomotion. Elife *4*, 1–36.

Stanislaw, H., and Todorov, N. (1999). Calculation of signal detection theory measures. Behav. Res. Methods, Instruments, {&} Comput. *31*, 137–149.

Waiblinger, C., Brugger, D., and Schwarz, C. (2015). Vibrotactile discrimination in the rat whisker system is based on neuronal coding of instantaneous kinematic cues. Cereb. Cortex *25*, 1093–1106.

Weber, A.I., Saal, H.P., Lieber, J.D., Cheng, J.-W., Manfredi, L.R., Dammann, J.F., and Bensmaia, S.J. (2013). Spatial and temporal codes mediate the tactile perception of natural textures. Proc. Natl. Acad. Sci. *110*, 17107–17112.

Wolfe, J., Hill, D.N., Pahlavan, S., Drew, P.J., Kleinfeld, D., and Feldman, D.E. (2008). Texture coding in the rat whisker system: slip-stick versus differential resonance. PLoS Biol. *6*, e215.

Yu, J., Gutnisky, D.A., Hires, S.A., and Svoboda, K. (2016). Layer 4 fast-spiking interneurons filter thalamocortical signals during active somatosensation. Nat. Neurosci. *19*, 1–14.

Zuo, Y., Perkon, I., and Diamond, M.E. (2011). Whisking and whisker kinematics during a texture classification task. Philos Trans R Soc L. B Biol Sci *366*, 3058–3069.

Chapter 4

Conclusion

In summary, the results from these experiments advance our understanding of cortical laminar and tactile processing in rodent whisker primary somatosensory cortex (S1). In Chapter 2 we showed that layer 2/3 (L2/3) is a site of profound decreases in recurrent inhibition following sensory deprivation, which correlates with decreases in evoked and spontaneous gamma rhythm generation. The cellular and molecular mechanisms underlying this activity regulation are an ongoing area of study. In Chapter 3, we showed that cortex simultaneously responds to microscopic and macroscopic features of whisker touch. In particular, stick-slip whisker motions predict rough surface textures, and drive increased spiking in S1. Further, stick-slips occur with high spatiotemporal precision, locking to specific surface features such as bar ridges to produce spatial and temporal signatures. Kinematic variation in time is often different than local variation in space (Figure 4.1A), and whether spatial features are ultimately represented with spatial or temporal codes is not known. Thus, we briefly explore how spatial and temporal coding of these features could work given prior literature in the whisker system.

The first mechanism combines our findings in Chapter 3 with previous studies in whisker-based object localization (Kleinfeld and Deschênes, 2011). These studies found evidence for a whisker position code based on whisk cycle amplitude (coded in primary motor cortex, M1), whisk cycle set point (coded in M1), and whisker phase (coded in S1). These three variables can be combined to predict whisker position instantaneously in time (Figure 4.1B). To this equation, we have added an additional term for mouse body position (θ_{run}), which is required for coding slip position on spatial scales larger than the contacting arc of one whisk cycle (~1.5 cm). A neural representation of body position has been thoroughly studied in place cells of CA1, hippocampus (O'Keefe and Dostrovsky, 1971). Thus, this temporal coding of space could bind each slip to a

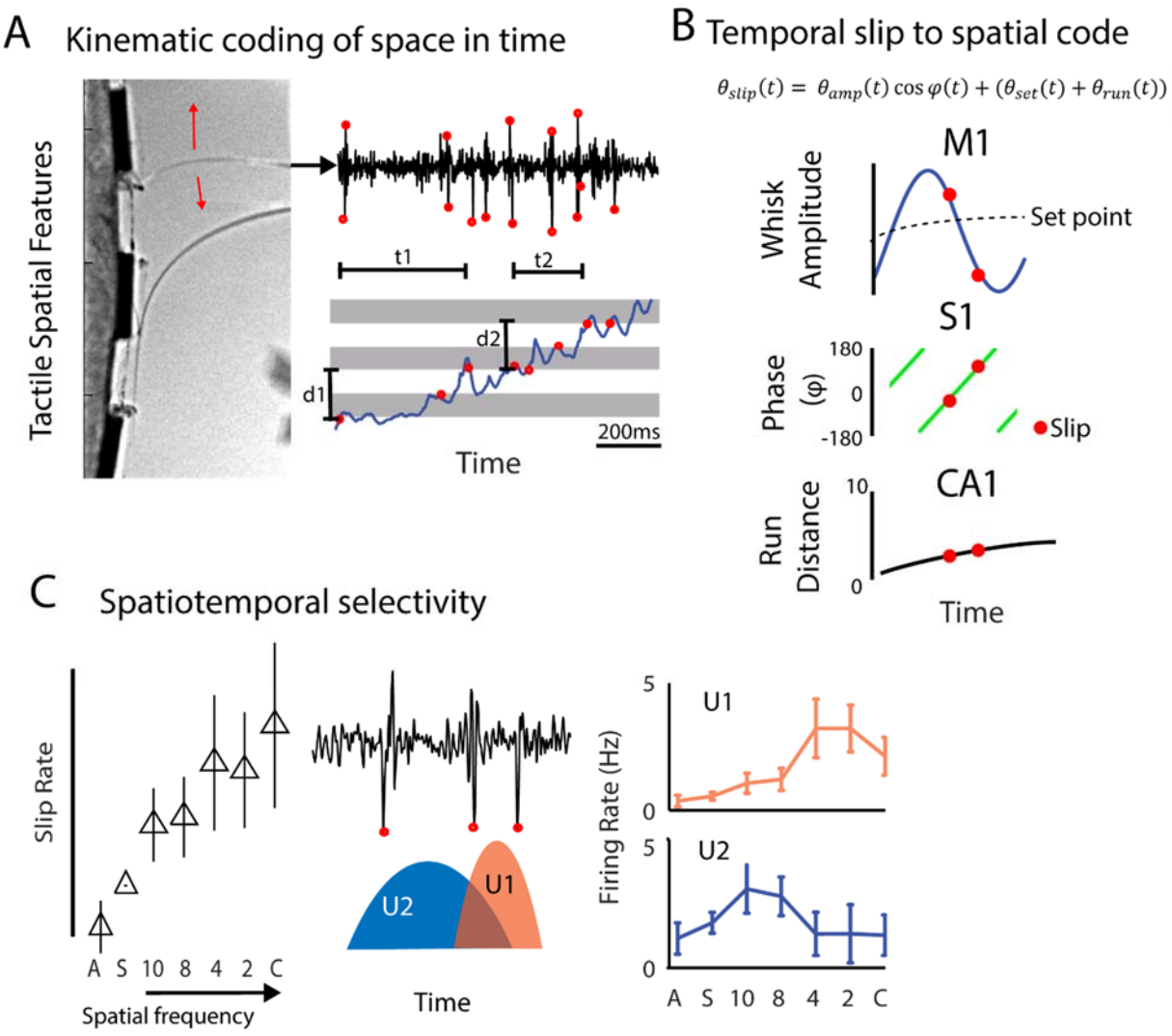

Figure 4.1. Temporal slip coding of local shape. (A) Kinematic coding of space in time. Left: Back and forth whisker movements accumulate kinematic events in time in the form of stick-slips, shown right with slips in red. Bottom: whisker position trace in blue as the whisker encounters bars spaced 10mm apart (grey). Slips that happen an equal distance apart (d1 = d2 = 10mm) may be correlated with time, but do not necessarily happen at equal intervals (t1 ≠ t2). (B) In order to read the position of slips in time, the central nervous system may combine several known sources of information using the formula shown (adapted from: Kleinfeld and Deschênes, 2011). Top: neurons in primary motor cortex (M1) are known to code whisk cycle amplitude (θ_{amp}) and set point (θ_{set}) in head-centered coordinates. Middle: neurons in S1 are known to code contact phase (ϕ) and slip kinematics. Bottom: Rodent position (θ_{run}) is coded with high precision by place cells in CA1 of the hippocampus. (C) Left: slip rate correlates with spatial frequency, thus some degree of spatial selectivity could arise from integration windows of different durations. Middle: cartoon example of two different integration windows relative to slip kinematics. Right: Example of actual S1 units that responded preferentially to specific spatial periods, an outcome that could arise from temporal integration if spatial frequency is strongly correlated with kinematic rate.

specific location, allowing relative spatial comparisons across accumulated time points at heterogeneous intervals (Figure 1A).

A second mechanism for spatial coding could function strictly in time. We observed that the temporal rate of slips positively correlated with the spatial frequency of local spatial features (Figure 4.1C, left). Thus, neurons with distinct temporal integration windows might select for slips at particular time intervals (Figure 4.1C, middle), possibly providing one mechanism for the spatial frequency tuning curves we observed in L5 regular spiking neurons (Figure 4.1C, right). In support of this hypothesis, previous work has shown that temporal integration windows in L5 of S1 can be quite large, often exceeding 150ms (McGuire et al., 2016).

References

Kleinfeld, D., and Deschênes, M. (2011). Neuronal basis for object location in the vibrissa scanning sensorimotor system. Neuron *72*, 455–468.

McGuire, L.M., Telian, G., Laboy-Juárez, K.J., Miyashita, T., Lee, D.J., Smith, K.A., and Feldman, D.E. (2016). Short Time-Scale Sensory Coding in S1 during Discrimination of Whisker Vibrotactile Sequences. PLOS Biol. *14*, e1002549.

O'Keefe, J., and Dostrovsky, J. (1971). The hippocampus as a spatial map. Preliminary evidence from unit activity in the freely-moving rat. Brain Res. *34*, 171–175.